A Theoretical Study on the Structure and Dynamics of Electronically Excited Molecules

（電子的に励起された分子の構造及び
ダイナミックスに関する理論的研究）

天辰　禎晃

①

A Theoretical Study on the Structure and Dynamics of Electronically Excited Molecules

（電子的に励起された分子の構造及びダイナミックスに関する理論的研究）

Yoshiaki Amatatsu

Contents

Acknowledgement

The author wishes to express his gratitude to Professor Shigeki Kato for his kind and continuous encouragement in carrying out the research. He also thanks Professor Soji Tsuchiya for his kind and continuous encouragement in preparing this thesis. He is obliged to express gratitude to Professor Keiji Morokuma and Dr. Satoshi Yabushita in carrying out the research of Part II. Finally, he is also grateful to the members of Professor Morokuma group.

Preface

A goal of theoretical chemistry is to clarify how and why the chemical reactions proceed from the first principle and to predict what is going on. The recent advances of computer brought about a remarkable progress in the electronic structure theory and has enabled theoretical chemists to accomplish the above goal as far as we are interested in small molecules in the ground state. Many ab initio Molecular Orbital (MO) calculations reproduced the experimental data and also gave the theoretical interpretations to the conventional chemical intuitions. Furthermore, the accumulation of results gave the empirical guide as to the reliability of calculations depending on the level of calculations.

On the other hand, the calculations of electronically excited molecules are less abundant than those of molecules in the ground state because, for the former, large scale calculations have to be performed to obtain reliable information of molecular properties such as the excited energies.

The recent progress of experimental techniques gave detailed information of the structure and dynamics of electronically excited molecules, which raised many new questions forced the conventional interpretations to be reexamined. In many cases, empirical potential functions been used to study the dynamics of electronically excited molecules. However, it was pointed out that empirical potential functions are inappropriate for covering various experiments because they were usually designed to reproduce a particular experiment. Therefore, experimental and theo-

retical chemists who work in the reaction dynamics look for ab initio potential energy surfaces (PESs).

Considering the situations described above, the author believes that a theoretical approach based on ab initio PESs is very significant for studying the structure and dynamics of electronically excited molecules. The determination of PESs by ab initio methods has several advantages over the determination of the same quantity by experimental measurements. They are summarized as follows.

1. In the theoretical study, a compound is characterized only by its number of electrons plus the charges and locations of its constituent nuclei. Therefore, the calculation can be carried out at all the nuclear geometries for systems irrespective of their thermodynamic stability and hence allows one to determine the entire potential energy surface.

2. The same theoretical method can be employed for the entire wavelength region from inner-shell ionization or excitation to the far-infrared, whereas different experimental equipment is generally needed for ultraviolet and infrared spectroscopy. The calculations are also in principle the same for all electronic states irrespective of their multiplicity or character.

3. An analysis of the calculated wavefunctions or properties gives insight into the qualitative principles that govern certain effects, and from this information qualitative rules can be derived which would allow predictions without actual calculations in related systems.

Considering these advantages, the ab initio method is a

powerful tool to study chemical reactions. In the following parts, the author will treat two problems relating to the structure and dynamics of the electronically excited molecules to which much attention has been paid from the experimental and theoretical points of view. He will derive ab initio potential functions and examine the structure and dynamics of the electronically excited molecules theoretically.

Part I

Charge Transfer State Formation in Polar Solvent

Chapter 1

General Introduction

1-1. Survey of Experimental Studies on the Charge Transfer Reaction of Electronically Excited Molecules

The formation of the charge transfer (CT) complexes through the electronic excitation is one of the most fundamental processes in organic photochemistry. Since the solvent can contribute to the energy dissipation of electronically excited molecules, the reaction shows the aspect which is not observed in gas phase reaction. Such a solvent effect has recently been attracted from a theoretical and experimental point of view (1-4).

Lippert et al first observed two kind of fluorescences in dilute N,N-Dimethylaminobenzonitrile (DMABN). One is the normal fluorescence and the other is the anomalous one which is observed at a longer wave length with a broader width. Since then, a series of compounds which show the dual fluorescence have been studied to characterize the anomalous emitting state and to discuss the role of solvent in the reaction. Although several mechanisms involving ground- or excited state complex formation were proposed at an early stage of this study (6), twisted internal charge transfer (TICT) mechanism by Grabowski and coworkers was widely accepted to explain the dual fluorescence (7). This was based on the following experimental findings:

i) the longer wavelength emission depends on the solvents while the shorter wavelength is almost independent of them.

ii) the compounds related to DMABN, for which twisting of the amino group are blocked, does not exhibit the longer wavelength emission (7,8).

iii) Similar model compounds that are twisted in the ground state such as 4-cyano-2,6,N,N-tetramethylaniline lack or nearly lack

the normal short-wavelength fluorescence (7,9).

From these experimental findings, they characterized the two emitting states and proposed the reaction scheme schematically represented in the figure. The excited molecule A^* can be directly deexcited to molecule A. Since the relaxation process from A^* to A state is independent of the solvent polarity, the A^* state is the locally excited (LE) state with a less ionic character. The excited species A^* is also possible to go to the other excited B^*. In this process, the reorientation of the surrounding solvent molecules is accompanied by change of the charge distribution of the solute. The photoemission from B^* to A can be observed at a longer wavelength. From the experimental findings ii) and iii) mentioned above, the anomalous emitting state has twisted geometry and so the $\pi-\pi$ conjugation between dimethylamino part and aromatic ring is broken and the charge is transferred from amino moiety to aromatic ring to generate the CT state.

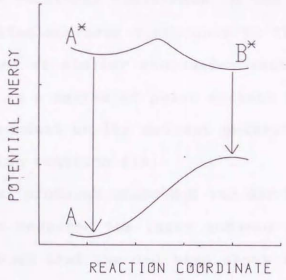

The TICT mechanism was confirmed or modified by several experimental works. Bischof et al found that TICT state was

formed independently in any solvent environments, that is, the CT state formation is a true intramolecular process (10). The time-resolved spectroscopic techniques gave more detailed information on the dynamics of the CT state formation and gave rise to much controversy about the CT formation process. Kosower et al measured the fluorescence decay time in a series of linear alcohols, which was found to correlate the dielectric relaxation time (11). They concluded that the motion of solvents controls the TICT formation. Following their suggestion, Dobowski et al pointed out that the TICT formation process is viscosity-controlled (12). On the other hand, Rettig and Wermuth found that the TICT formation rate depends on the solvent polarity (13). Low temperature quantum yield measurements and direct laser kinetic data show that the rate of formation of the TICT states in n-butylchloride is a factor of 2 - 13 greater than that of the nitriles. This is ascribed to the presence of a conical intersections along the reactions coordinate in the case of nitriles. That is, two excited surfaces contribute to the TICT formation. Hicks et al reached at similar conclusion that variation of the dynamics of DMABN in a series of polar solvent is ascribed to the barrier height dependent on the solvent polarity rather than the viscosity controlled reaction (13).

Kajimoto et al produced DMABN-H_2O van der Waals complex in a molecular beam and measured the laser induced fluorescence spectra (15). They found that the 0-0 band shows the blue-shift and the emission spectra of this complex does not contain the CT state component. From these findings, they pointed out the importance of the location of solvating molecules in the CT state

formation. Furthermore, they measured the dual fluorescence in a supercritical CF_3H fluid to characterize the nature of emitting state (16). They found that both the Stokes shift and the ratio between the CT and the S_1 emissions increased with increasing density of the polar fluid.

Contrary to the above discussion which insisted that the TICT formation is solvent-controlled, Su and Simon estimated the average survival probability of the locally excited (LE) state and found that the average life time of DMABN in the LE state is faster than the longitudinal solvent relaxation time (17). In comparison with their experimental data and recent Marcus theory, they concluded that the fluctuation of intramolecular motion is relatively important in the CT state formation.

1-2. Theoretical Treatments of Electron Transfer Reactions

In spite of above mentioned controversies about the CT state formation, theoretical studies on this problem are very limited. One of the reasons is that there is no realistic molecular model derived from the microscopic point of view. Many of previous theoretical models contain many assumptions and adjustable parameters which can not be determined *a priori*.

Before proceeding the present work, the author will summarize the theoretical models for the solute-solvent interaction and the dynamics of electron transfer on which many previous works are based.

1-2-1. Continuum Dielectric Model

In static treatment, the role of the solvent is to modify the potential energy surface (PES) in a gas phase. Continuum dielectric model, which was developed by Born (18) and Onsager (19), is a convenient tool to estimate the change of PES in a polar solvent. In this model the solvent is replaced by a frequency dependent dielectric continuum, with dielectric function, $\varepsilon(\omega)$, and the polar solute by a dipole within a cavity of some simple shape. The solvation energy is obtained by evaluating the reaction field of the polar solute molecule inside the molecular cavity. For instance, when the shape of the molecular cavity is sphere with the radius r_c, the solvation energy is

$$\Delta E_{Solv} = (\varepsilon(\omega)-1)/(2\varepsilon(\omega)+1)\ 1/r_c^3 \sum_j \mu_j 2 \qquad (1)$$

The predictions of homogeneous continuum theories are most simply discussed in terms of a solvation time correlation function, which is directly connected with a relaxation time

$$\tau_L^d = (2\varepsilon_\infty + \varepsilon_C)/(2\varepsilon_0 + \varepsilon_C)\ \tau_D \qquad (2)$$

where ε_0 and ε_∞ are the static and the optical dielectric constants of the solvent and τ_D is the Debye relaxation time of the dipolar solvent (20-21). ε_C is the dielectric constant of the molecular cavity. The application of this theory is well known by Lippert-Mataga equation in order to quantify the red-shifts and relate them to dipole moments of fluorescing spices (22).

However, this model is too simple in two points. The first point is that the above simple model was derived under the assumptions that the molecular cavity is spherical and the solvent dielectric response is of simple Debye form. Then both assumptions were relaxed into the ellipsoidal cavity and a non-Debye dielectric response (23). Castner et al pointed out the importance of non-Debye form to describe the solvent relaxation.

The second point is that the role of the solvents near the solute is same as that of solvent far from the solute in the above homogeneous model. Another modification, what is called inhomogeneous model, was done by several authors. Bagchi presented the inhomogeneous dielectric theory that the dielectric constant, $\varepsilon(r)$ was allowed to vary continuously as a function of distance (r) from the polar solute molecule and the solvation energy was evaluated by solving the Laplace equation, with the position- and frequency-dependent dielectric constant, $\varepsilon(r,\omega)$ (24). In another theory by Castner, a discrete shell representation of the position dependent dielectric function was assumed and the solvation energy was expressed as a sum of the solvation energy from each shell (25). The main effect of the dielectric inhomogeneity was to introduce relaxation times slower than τ_L and to make the decay non-exponential. It is also pointed out that the solvent response to a change in dipole moment is slower than that to a change in the charge.

Although these continuum dielectric models are quite phenomelogical, they are in agreement with experiment and provide a simple and intuitive picture of solvation dynamics and at the same time incorporate some aspects of solute-solvent interac-

tions.

1-2-2. Marcus' Thoery

Next the author turns to microscopic or molecular theory to describe the CT reaction in solution. Marcus' theory has been developed to explain the electron transfer which is the special problem in the chemical reaction in solution (26-28). This theory is based on absolute reaction rate theory by Eyring (29). The rate constant is given by eq.3

$$k_M = \kappa B \exp(-\Delta G^{\ddagger}/k_B T)$$
$$= \kappa B \exp(\Delta S^{\ddagger}/k_B) \exp(-\Delta H^{\ddagger}/k_B T) \qquad (3)$$

In this equation, $\Delta G^{\ddagger}$, $\Delta S^{\ddagger}$, $\Delta H^{\ddagger}$ are the free energy, entropy, entalpy, k_B is the Boltzmann constant, B is the liquid phase collision frequency with the order of 10^{13} sec^{-1}. κ relates the electron transfer probability. If the reaction is adiabatic, κ has the value 1, that is, there is no recrossing on potential surface, and less than 1 if non-adiabatic. Marcus gives the following equation for $\Delta G^{\ddagger}$

$$\Delta G^{\ddagger} = (\lambda + \Delta G^{0})^2/4\lambda \qquad (4)$$

ΔG^{0} is the standard free-energy increase for the electron trans-

fer reaction. The quantity λ, which is estimated from experiment, is the reorganization energy which is coupled to the electron transfer. In other words, λ is the energy which would be required to move all the atoms from their equilibrium positions before electron transfer to the equilibrium positions after electron transfer. Furthermore, Marcus divides λ into two parts, $\lambda_i + \lambda_o$ in order to analyze the solvent effect on the electron transfer reaction (28). λ_i is the reorganization energy of the inner shell of atoms and λ_o is that of the surrounding solvent molecules. λ_i is approximated by the inner-shell normal mode;

$$\lambda_i = 1/2 \sum_j \lambda_j Q_j^2 \qquad (5)$$

and λ_o is evaluated from the polarizability of the solvent which is considered to be a continuous polar medium;

$$\lambda_o = (\Delta e)^2/4\pi\varepsilon_0 \, (1/(2r_1) + 1/(2r_2) - 1/r_{12})(1/D_{op} - 1/D_s) \qquad (6)$$

where Δe is the charge transferred from donor to acceptor, r_1 and r_2 are the radii of the two reactants, D_{op} and D_s are the square of the refractive index of the medium and the static dielectric constant, respectively. This Marcus' theory was suitable for a reaction with a high activation barrier and based on a continuum description of the solvent polarization.

The various theory of the electron transfer reaction has developed on the basis of Marcus' theory. Levich and Dogonadze advanced a non-adiabatic electron-transfer theory, where the microscopic electronic process rather than dielectric relaxation constitutes the rate-determining step (30-32). Their treatment which employed a stochastic solvent model that described the dynamics of polarization fluctuation by a simple Debye model has been further extended by introducing more realistic models for the dielectric relaxation of solvents (33-35).

Recently, Calef and Wolynes investigated the role of solvent fluctuation with special emphasis on the molecular nature of the solvent (36-38). In their theory, the reaction coordinate (X) is identified and a Smoluchowski equation for this reaction coordinate is derived;

$$\partial P(X)/\partial t = \partial (D(X)(\partial P + P\partial (V_{eff}(X)/k_BT)/\partial X)/\partial X \qquad (7)$$

where D(X) is a position-dependent diffusion coefficient and $V_{eff}(X)$ is an effective potential. A detailed calculation of one-dimensional reaction free energy surface was done. Their conclusion was that the molecular theory prefactors are significantly lower than those calculated completely within a continuum model.

The low- or zero-barrier intramolecular electron transfer reaction has been of much interest for the last few years. In this type of reaction, since there is no clear separation of time scale between the motion in the reaction zone and the rest of

the potential surface, the theory for a low-barrier reaction is different from the traditional theory for a high-barrier reaction. Recently Marcus and co-workers presented a theory for a low-barrier electron transfer reaction (39,40). Their theory includes an average effect of the fast intramolecular vibrational motions of the reactant and treats the diffusive orientational motion of the solvent by using the continuum model. The low-barrier reaction was modeled as a diffusive process on a harmonic surface with the solvent polarization (X) as the reaction coordinate. The reaction takes place when the solvent polarization attains a certain critical value, X_c. The time-dependent probability distribution P(X,t) is given by a modified Smoluchowsky equation;

$$\partial P(X,t)/\partial t = \tau_L^{-1} \partial (\partial/\partial X + X)P/\partial X - k_c(X)P \qquad (8)$$

where $k_c(X)$ is a coordinate dependent rate constant and τ_L is the longitudinal polarizability relaxation time of the unperturbed solvent. The form of $k_c(X)$ depends on the nature of the participating electronic potential surfaces. Several limiting forms for the position dependence of $k_c(X)$ have been investigated in detail. If the vibrational modes of the electron transfer system make a little contribution to electron transfer, $k_c(X)$ is sharply peaked around X_c and may be represented by a delta function. On the other hand, if the contribution from vibrational modes dominates the reaction, the reaction window is wide and $k_c(X)$ may be represented by a broad Gaussian around X_c. The magnitude of the rate at the critical polarization value, X_c, is

governed by the adiabaticity/non-adiabaticity of the reaction. Their conditions for the validity of the results was also presented by Onuchic (41). This recent Marcus' theory was used to analyze the experiment by Su and Simon (17).

1-2-3. Molecular Theory

The importance of the molecular nature of the solvent in solution reaction calls for a quantitative understanding of microscopic process involved in orientational and polarization relaxation of a dense dipolar liquid. Several approaches have been done using generalized Smoluchowski equation (42-44)

$$\partial \delta P(r,\omega,t)/\partial t = D_R \nabla_\omega^2 \delta P + D_T \nabla^2 \delta P - [D_R \nabla_\omega \cdot P \nabla_\omega + D_T \nabla P \nabla] \beta F \qquad (9)$$

where $P(r,\omega,t)$ is the position, orientation and time-dependent density of the solvent, δP, the density fluctuation from the equilibrium state, D_R and D_T are the rotational and translational diffusion coefficients of the solvent, respectively. ∇_ω and ∇ are the usual angular and spatial gradient operators. The first and second terms are diffusion terms, and the last term is a free energy term which consists of a potential mean force and a mean field due to the other molecules.

$$\beta F = \int dr' d\omega' c(r,\omega,r',\omega') \delta P + \beta U_{ext} \qquad (10)$$

c is the two-particle direct correlation function of the dipolar solvent. U_{ext} is the external field which comes from the solute ion or dipole. From eq.9, the following expressions can be obtained. One is the time-dependent solvent polarization of a dipolar liquid, which is related to number density of the solvent

$$P^{pol}(r,t) = \mu \int d\omega\, \hat{\alpha}(\omega) P(r,x,t) \qquad (11)$$

where $\hat{\alpha}(\omega)$ is a unit vector with orientation ω and μ is the magnitude of the dipole moment of the solvent molecules. Relating to eq.11, the time-dependent solvation energy is given by

$$E^{solv}(t) = -1/2 \int dr D(r) \cdot P^{pol} \qquad (12)$$

where D(r) is the bare electric field of the polar solute molecule. Furthermore, the expression for polarization relaxation for dipolar hard spheres can be obtained. Both longitudinal and transverse components were found to relax exponentially with time constants given by

$$\tau_L(k) = (2D_R)^{-1}[1 + p'(k\alpha)^2 - P_0/3\ (1 + p'(k\alpha)^2(C_\Delta + 2C_D)]^{-1} \qquad (13)$$

$$\tau_T(k) = (2D_R)^{-1}[1 + p'(k\alpha)^2 - P_0/3\ (1 + p'(k\alpha)^2(C_\Delta - C_D)]^{-1} \qquad (14)$$

where τ_L and τ_T are the wavevector-dependent longitudinal and transverse polarization relaxation times, respectively, and p' = $(D_T/2D_R\sigma^2)$, σ is the solvent molecular diameter. p' is a measure of the relative importance of translational modes in solvent polarization relaxation. P_0 is the equilibrium number density of bulk solvent. C_Δ and C_D are the anisotropic parts of the direct correlation functions. Calef et al and Chandra & Bagchi examined the dynamical properties varying the parameters in this theoretical model and pointed out that structural relaxation occurs with multiple relaxation times.

Maroncelli and Fleming have carried out the equilibrium and non-equilibrium molecular dynamics (MD) simulations to study the time-dependence of solvation in water (45). Relaxation of the solvation energy following step function jumps in the solute's charge, dipole moment and quadrupole moment have been determined from equilibrium MD simulation under the assumption of a linear solvent response. The relaxation times observed differ substantially depending on the type of multipole jump and the charge/size ratio of the solute. They concluded that the Onsager's picture of monotonically increasing relaxation time with distance is not correct for the systems studied. They have also pointed out that the structure of the first solvation shell plays an important roll in solvation dynamics. Their conclusion is, roughly speaking, in accord with the theoretical study mentioned above.

References

1. E.M.Kosower, Ann.Rev.Phys.Chem. 37 127 (1986).

2. K.Peters, Ann.Rev.Phys.Chem. 38 253 (1987).

3. E.Lippert, W.Rettig, V.Bonacic-Koutechy, F.Heisel and J.A.Miehe, Adv.Chem.Phys. 68 1 (1987).

4. B.Bagchi, Ann.Rev.Phys.Chem. 40 115 (1989).

5. E.Lippert, W.Luder and H.Boos, in 'Advances in Molecular Spectroscopy', A.Mangini ed., Pergamon Press, Oxford, 1962.

6.(a) O.S.Khalil, R.H.Hofeldt and S.P.Mcglynn, Chem.Phys.Lett. 17 479 (1972).
(b) O.S.Khalil, R.H.Hofeldt and S.P.Mcglynn, J.Lumin. 6 229 (1973).
(c) O.S.Khalil, R.H.Hofeldt and S.P.Mcglynn, Spectrosc.Lett. 6 147 (1973).

7.(a) K.Rrotkiewicz, K.H.Grellmann and Z.R.Grabowski, Chem.Phys.Lett. 19 315 (1973).
(b) K.Rrotkiewicz, Z.R.Grabowski, A.Krowczynski and W.Kuhnle, J.Lumin. 12 877 (1976).
(c) Z.R.Grabowski, K.Rrotkiewicz, A.Siemarczuk, D.J.Cowly and W.Baumann, Nouv.J.Chimie 3 443 (1979).
(d) Z.R.Grabowski, K.Rrotkiewicz, W.Rubaszewska, and E.Kirkor-Kaminska, Acta. Phys. Polonica A54 767 (1979).
(e) Z.R.grabowski and J.Dobkowski, Pure and Appl.Chem. 55 245 (1983).

8. W.Rettig, K.Rotkiewicz and W.Rubaszewska, Spectrochim.Acta 40A 241 (1984).

9. K.Rotkiewicz and W.Rubaszewska, Chem.Phys.Lett. 70 444 (1980).

10. H.Bischof, W.Baumann, N.Detzer and K.Rotkiewicz, Chem.Phys.Lett. 116 180 (1985).

11. (a) D.Huppert, H.Kanety and E.M.Kosower, Chem.Phys.Lett. 84 38 (1981).
(b) E.M.Kosower and D.Huppert, Chem.Phys.Lett. 96 433 (1983).

12. J.Dobkowski, E.Kirkor-Kaminska, J.Koput and A.Siemiarczuk, J.Lumin. 27 339 (1982).

13.(a) G.Wermuth, Z.Natforsch 38a 641 (1983).
(b) G.Wermuth, R.Rettig and E.Lippert, BerBunsenges.Phys.Chem. 81 64 (1981).
(c) W.Rettig and G.Wermuth, J.Photochem. 28 351 (1985).

14 (a). J.Hicks, M.Vandersall, Z.Babarogic and K.Eisenthal, Chem.Phys.Lett. 116 18 (1981).
(b). J.Hicks, M.Vandersall, E.V.Sitzmann and K.Eisenthal, Chem.Phys.Lett. 135 413 (1987).

15. T.Kobayashi, M.Futakami and O.Kajimoto, Chem.Phys.Lett. 130 63 (1986).

16. O.Kajimoto, M.Futakami, T.Kobayashi and K.Yamasaki, J.Phys.Chem. 92 1347 (1988).

17. S.G.Su and J.D.Simon, J.Chem.Phys. 89 908 (1988).

18. M.Born, Z.Phys. 1 45 (1920).

19. L.Onsager, J.Amer.Chem.Soc. 58 1485 (1935).

20. Yu.T.Mazurenko and N.G.Bakshiev, Opt.Spectrosc. 28 490 (1970).

21. B.Bagchi, D.W.Oxtoby and G.R.Fleming, Chem.Phys. 86 257 (1984).

22.(a) E.Lippert, Z.Naturforsch 10a 541 (1955).
(b) E.Lippert, Ber.Bunsenges.Phys.Chem. 61 962 (1957).
(c) N.Mataga, Y.Kaifu and M.Koizumi, Bull.Chem.Soc.Japan, 29 115 (1956).
(d) N.Mataga, Y.Kaifu and M.Koizumi, Bull.Chem.Soc.Japan, 29 465 (1956).

23. E.W.Castner Jr., G.R.Fleming and B.Bagchi, Chem.Phys.Lett. 143 270 (1988).

24. B.Bagchi, E.W. Castner Jr. and G.R.Fleming, J.Mol.Struct. Theor.Chem. 194 171 (1989).

25. E.W.Castner Jr., G.R.Fleming, B.Bagchi and M.Maroncelli, J.Chem.Phys. 89 3519 (1988).

26.(a) R.A.Marcus, J.Chem.Phys. 24 966 (1956).
(b) R.A.Marcus, J.Chem.Phys. 26 867 (1957).

27. R.A.Marcus, Ann.Rev.Phys.Chem. 14 155 (1964).

28. R.A.Marcus, J.Chem.Phys. 43 679 (1965).

29. S.Glasstone, K.J.Laidler and H.Eyring, 'The Theory of Rate Processes', McGraw-Hill, New-York (1941).

30. V.G.Levich and R.R.Dogonadze, Coll.Czech.Chem.Commun. 26 193 (1961).

31. R.R.Dogonadze, Kharkats, I.Yu and J.Ustrup, Chem.Phys.Lett. 37 366 (1976).

32. R.R.Dogonadze, J.Ustrup, Karkats, Yu,
J.Theor.Biol. 40 279 (1973).

33. S.Efrima and M.Bixon, J.Chem.Phys. 70 3531 (1979).

34. L.D.Zusman, Chem.Phys. 49 295 (1980).

35. I.V.Alexandrov, Chem.Phys. 51 449 (1980).

36. D.F.Calef and P.G.Wolynes, J.Phys.Chem. 87 3387 (1983).

37. D.F.Calef and P.G.Wolynes, J.Chem.Phys. 78 470 (1983).

38. D.F.Calef and P.G.Wolynes, J.Chem.Phys. 78 4145 (1983).

39. H.Sumi and R.A.Marcus J.Chem.Phys. 84 4894 (1986).

40. W.Nadler and R.A.Marcus, J.Chem.Phys. 86 3906 (1987).

41. J.N.Onuchic, J.Chem.Phys. 86 3925 (1987).

42. D.F.Calef and P.G.Wolynes, J.Chem.Phys. 78 4145 (1983).

43. A.L.Nicholas III and D.F.Calef,
J.Chem.Phys. 89 3783 (1988).

44. a) A.Chandra and B.Bagchi, Chem.Phys.Lett. 151 47 (1988).
b) B.Bagchi and A.Chandra, J.Chem.Phys. 90 7338 (1989).
c) B.Bagchi and A.Chandra, Chem.Phys.Lett. 155 533 (1989).

45. M.Maroncelli and G.R.Fleming, J.Chem.Phys. 89 5044 (1988).

Chapter 2

Charge Transfer State Formation of 4-(N,N-Dimethylamino)Benzonitrile in an Aqueous Solution

2-1. Introduction

The formation of charge transfer (CT) state is one of the fundamental processes in photochemistry of organic molecules in solutions. This process involves the relaxation of surrounding solvent molecules and the rate of CT state formation is known to be affected by the solvent dielectric relaxation time. Such a solvent effect in the chemical processes has recently received much attention from experimental (1,2) and theoretical (1,3,4) points of view.

There is a series of molecules which exhibit dual fluorescence in polar solvents (1,5). The polarity of solvent has been recognized to be a clue in understanding the origin of redshifted fluorescence. 4-(N,N-Dimethylamino) benzonitrile (DMABN) is a prototype of such a class of molecules. Although there are some controversies (6,7), the formation of a twisted intramolecular charge transfer (TICT) state (8,9) in the excited state has been generally accepted to be the origin of anomalous red shifts of fluorescence in polar solvents. In the TICT state where the dimethylamino group undergoes a 90° internal rotation with respect to the aromatic ring, an electron is completely transferred from the amino group to the benzonitrile moiety because the conjugation between the amino lone pair orbital and the π orbitals on the aromatic ring is absent and the dipole moment reaches to the extreme. The TICT state in DMABN is thus fully stabilized by the solvent dipoles.

In recent years many experimental works on DMABN have been performed to elucidate the mechanism of CT state formation. Kajimoto et al. (10) have measured the dual fluorescence in a

supercritical CF_3H fluid to characterize the nature of emitting state. They have confirmed the CT state from the observation that both the Stokes shift and the intensity of emission with a longer wavelength increase with increasing the density of polar fluid. The picosecond time resolved emission spectroscopy has been applied to examine the relative importance between the solvent dielectric relaxation and the intramolecular vibrational motion to the rate of CT state formation. Hicks et al. (11,12) have proposed that the barrier height for the CT state formation is controlled by the polarity of solvent from their experiments on DMABN in nitrile solutions. Su and Simon (13) have pointed out the importance of fluctuations of intramolecular vibrational motion compared to solvent diffusion in determining the reaction rates in alcohol solution. Their conclusions were deduced from the analyses of their experiments on the basis of theoretical model developed by Sumi, Nadler and Marcus (14,15). By using the supersonic expansion technique, the spectra of DMABN-solvent complex have been examined by several groups (16-18) to obtain the information about local solute-solvent interactions. All of these works revealed that 1:1 complex at low temperature does not exhibit the dual fluorescence under isolated conditions.

To obtain a satisfactory understanding of the mechanism of CT state formation in solutions, detailed theoretical studies for the potential energy surfaces including the solute-solvent interactions and for the dynamics of solute molecule under the influence of solvent motions. Statistical mechanics calculations such as Monte Carlo and molecular dynamics simulations for the

solute-solvent systems would give valuable information on the solvation processes (19-22). In spite of the experimental activities mentioned above, theoretical studies on DMABN are still limited at present. The potential energy surfaces of low-lying states of DMABN have been calculated by Rettig and Koutechy (23). They have employed the ab initio and semiempirical CNDO/S molecular orbital (MO) methods to characterize the excited state electronic structures. Dynamics calculations for the intramolecular electron transfer in DMABN based on a realistic molecular model are virtually nonexistent because of the lack of reliable potential energy functions and solute-solvent intermolecular potentials.

In this chapter, the CT state formation process of excited state DMABN in the aqueous solution is treated theoretically to provide a realistic description of the process at molecular level. We focus on the nature of solution phase potential energy profiles, the ingredient essential to understand the dynamics. We first perform ab initio MO calculations on the excites as well as the ground state potential energy surfaces of DMABN in the gas phase. With the aid of electron distributions obtained from the ab initio calculations, pair potentials are next constructed to describe the solute-solvent systems are then carried out to afford theoretical information on the solution phase potential energy surfaces partitioning in the CT state formation process and the solvation structures. In the next section, the results of calculations on the potential energy surfaces of ground and excited state DMABN are presented. The method of calculations are first summarized. We examine the nature of electronic struc-

tures of the excited states leading to the CT state and develop the diabatic representation of excited state potential surfaces to facilitate the calculations for solute-solvent systems. The intermolecular potentials derived here are used to calculate the structures of DMABN-water complex in the gas-phase and the resultant structures are compared to the available experimental results. In section 2-3, the Monte Carlo simulation calculations on the aqueous solution of DMABN are presented. The potentials of mean force for the ground and excited electronic states of DMABN are calculated as the function of torsional angle of dimethyl amino group to see the effect of solvation on the potential energy profiles. The mechanism of fluorescence shifts are also discussed on the basis of calculated solvation properties. The reaction free energy surfaces for the CT state formation process are calculated in section 2-4. The reaction surfaces are given as the function of solvation coordinate, representing the solvent configuration relaxation, and intramolecular vibrational coordinate. In section 2-5, we give a discussion on the mechanism of intramolecular CT state formation on the basis of the results of present calculations. The conclusions are also summarized in section 2-5.

2-2. Potential Energy Surfaces of DMABN

2-2-1. Method of calculations

The potential energy surfaces of the ground and excited states of DMABN were calculated by the configuration interaction (CI) method. We first carried out the geometry optimization for the ground state DMABN because it is experimentally unknown. The analytical energy gradient method for the Hartree-Fock (HF) wave function with the STO-3G basis set (24) was employed. The results were summarized in Table I. We have calculated the potential energy surfaces as a function of two internal coordinates, the torsional angle around the N_1C_1 bond τ and the wagging angle of dimethyl amino group θ. The coordinate system is give in Fig. 1. All the atoms except in the methyl groups were placed on the plane, the y-z plane, and the z-axis was taken to be the direction of N_1C_1. The geometric parameters were fixed to the values in Table I.

We used a modified MINI4 basis set (25) (Basis A) in the CI calculations. The 2p orbitals on the N and C atoms except in the methyl groups are of double zeta quality and the minimal MINI4 set was employed for all the other orbitals. This basis set is more flexible than the minimal basis set in describing the π orbitals of DMABN. The calculations were carried out at 25 points for the (τ, θ) pair; τ=0°, 20°, 45°, 70°, 90°, and θ=0°, 20°, 42°, 60°, 80°, respectively. In order to obtain more reliable energy estimates, the CI calculations with the split valence MINI4 basis set (25) (Basis B) were further carried out at two important geometries, the planar, (τ, θ) =(0°,0°), and perpendicular, (90°,0°), geometries. The numbers basis functions are

Table I. Optimized Geometry of DMABN[a)]

Bond Distances[b)]			
N_1-C_1	1.446	C_1-C_2	1.402
C_2-C_3	1.379	C_3-C_4	1.394
C_4-C_7	1.458	C_7-N_2	1.157
N_1-C_8	1.486	C_2-H_1	1.078
C_3-H_2	1.084	C_8-H_5	1.093
C_8-H_6	1.087	C_8-H_7	1.088
Valence angles[c)]			
$C_1C_2C_3$	121.1	$C_2C_3C_4$	120.8
$C_2C_1C_5$	117.7	$C_3C_4C_6$	118.6
$C_3C_2H_1$	118.2	$C_2C_3H_2$	119.5
$C_8N_1C_9$	115.1	$N_1C_8H_5$	112.4
$N_1C_8H_6$	111.3	$N_1C_8H_7$	108.1
Torsional angles[c)]			
$C_1N_1C_8H_5$	119.6	$C_1N_1C_8H_6$	-118.8
$C_1N_1C_8H_7$	-0.5		

a) Torsional and wagging angle of dimethylamino group are 0° and 41.8°, respectively.

b) Bond distances are given in Å.

c) Angles are given in degree.

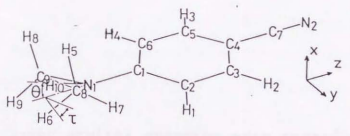

Fig.1 Coordinate system of DMABN

92 and 119 for the Basis A and B, respectively.

The one-particle basis functions in the CI wave functions were taken from the HF calculations. The orbital space was divided into three sub-spaces. We have chosen 10 orbitals as the active orbitals, which are the π and lone pair orbitals. Some of important active orbitals are displayed in Fig. 2. The 34

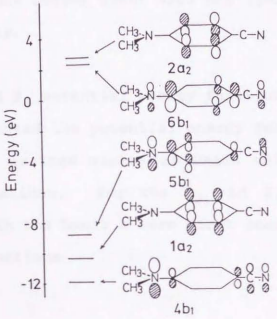

Fig.2 Schematic representation of important MO's of DMABN at the planar geometry. MO's are assigned in terms of C_{2v} symmetry although DMABN has only the C_s symmetry because of methyl group.

orbitals with lower orbital energies were regarded as the internal orbitals and the remaining ones with higher energies were as the external, respectively. All the single, double and triple

excitations within the active space from the HF configuration were included in the CI wave functions. In addition to those configurations, all the possible singly excited configurations, with the N and C 1s orbitals kept doubly occupied, from the important configurations were further taken into account. This choice of configurations is similar to the polarization CI (POL-CI) method (26). The numbers of configuration state functions in C_1 symmetry thus became about 9000 and 12000 for the Basis A and B, respectively.

2-2-2. S_0 and S_1 potential energy functions

We constructed the potential energy functions for the ground and low-lying excited states of DMABN using the results of ab initio calculations. For the S_0 and S_1 state, the energies calculated with the Basis A were first least square fitted to the analytical functions

$$W_I(\tau, \theta) = \sum_{n=0}^{3} (a_{n0} + a_{n2}\,\theta^2 + a_{n6}\,\theta^6) \cos 2n\tau \qquad (1)$$

These energy functions were further modified by adding the correction terms, $a + b\cos 2\tau$, to reproduce the barrier heights for the internal rotation around the NC bond calculated with the Basis B (Table II). The resultant potential energy surfaces are shown in Fig. 3.

Table II. Relative energies at the planar and perpendicular geometries

	Planar geometry ($\tau=0°, \theta=0°$) 1^1A_1	1^1B_2	2^1A_1	3^1A_1
Basis A	0.0[b]	5.44	5.99	7.87
Basis B	0.0[c]	5.26	5.71	7.64
	Perpendicular geometry ($\tau=90°, \theta=0°$) 1^1A_1	1^1A_2	1^1A_2	1^1A_1
Basis A	0.26	5.86	7.05	6.83
Basis B	0.26	5.79	6.32	6.53

a) Energies are given in eV.

b) Total energy is -454.7384 hartree.

c) Total energy is -454.8845 hartree.

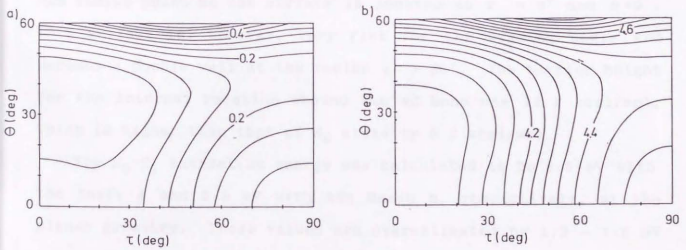

Fig.3 Contour maps of potential energy surfaces of S_0 and S_1 states. Potential surfaces of S_0 and S_1 states are given in (a) and (b), respectively. Energy at the minimum of S_1 surface is 4.0eV. Contour spacing is 0.05eV.

The ground state S_0 surface is a double well potential for the wagging angle and the energy increases along the torsional angle as seen in Fig. 3(a). The wagging angle at the minimum energy point was calculated to be 38.2° and the inversion barrier of dimethylamino group was 1.6 kcal/mol at $\tau = 0°$. The barrier height for the NC internal rotation was 5.9 kcal/mol.

The first excited S_1 state is characterized by the two electronic configurations,

$$\cdots\cdots(4b_1)^2(1a_2)^2(5b_1)(2a_2) \qquad (2)$$

and

$$\cdots\cdots(4b_1)^2(5b_1)^2(1a_2)(6b_1), \qquad (3)$$

at the planar geometry and the weights of configurations correlated to them in the CI wave function were almost constant at all the geometries considered here. As seen in Fig. 3(b), the minimum energy point on the surface is located at $\tau = 0°$ and $\theta = 0°$. This surface is, however, very flat for the wagging angle and becomes a double well at the region $\tau > 20°$. The barrier height for the internal rotation around the NC bond was 12.1 kcal/mol, which is higher than that of S_0 state by 6.2 kcal/mol.

The S_0-S_1 excitation energy was calculated to be 5.5 eV with the Basis A and 5.3 eV with the Basis B, respectively, at the planar geometry. These values are overestimated by 1.3 ~ 1.5 eV compared with the experimental excitation energy, ~ 4 eV. We therefore shifted the S_0 energy in constructing the potential

energy functions (Fig.3) so that the adiabatic S_0-S_1 excitation energy becomes 4.0 eV. The parameters for the S_0 and S_1 potential functions are summarized in Table V.

Table V. Parameters of potential energy functions

(A) Diagonal elements

	S_0	S_1	D_1	D_2	D_3
a_{00} [a]	0.1785	4.2581	5.2671	5.5062	6.3993
a_{02} [b]	-0.3034	-0.1374	0.4178	-0.4386	-0.1569
a_{06} [c]	0.5119	0.4299	0.4209	0.4311	0.4466
a_{20} [a]	-0.1447	-0.2771	0.2015	0.1527	-0.0360
a_{22} [b]	0.0906	0.1456	-0.1635	-0.1942	0.1139
a_{26} [c]	0.0092	0.0018	0.0374	0.0174	-0.0000
a_{40} [a]	0.0176	0.0054	0.0058	0.0332	0.0140
a_{42} [c]	-0.0010	0.0293	-0.0130	-0.0304	0.0133
a_{46} [a]	-0.1183	-0.1297	-0.1303	-0.1098	-0.1185
a_{60} [b]	0.0164	0.0137	0.0127	-0.0062	-0.0025
a_{62} [c]	-0.0196	0.0043	-0.0035	0.0106	0.0137
a_{66}	0.0066	-0.0009	0.0226	0.0082	-0.0045

(B) Off-diagonal elements

D_{12}		D_{13}		D_{23}	
b_1 [a]	-1.0044			b_0 [a]	-0.2490
b_3 [a]	0.0011	-0.4821		b_0 [a]	0.0821
		0.0073		b_4 [a]	-0.0160
				c	0.0455

a) Given in eV.

b) Given in eV rad^{-2}.

c) Given in eV rad^{-6}.

2-2-3. Diabatic representation of CT state surface

In solutions the shape of potential energy surfaces will be modified by solute-solvent interactions. Among the various components of interaction energy such as the dispersion and the exchange term, the electrostatic potential by solvent molecules applied to the solute is expressed by the one electron operator v(x), the potential energy of the I-th state is calculated by

$$W_I(X) = W_I^0(X) + V_{II}(X) + \sum_{J=1}^{N} |V_{IJ}(X)|^2/(W_J^0(X)-W_I^0(X)) \quad (4)$$

using the second order perturbation theory. The energy of isolated solute molecule is $W_I^0(X)$ where X stands for the molecular coordinates of solute. The diagonal and off-diagonal elements of electrostatic potentials are given by

$$V_{II}(X) = \int \rho_{II}(x,X)v(x)\,dx \quad (5)$$

and

$$V_{IJ}(X) = \int \rho_{IJ}(x,X)v(x)dx \quad (6)$$

respectively, where ρ_{II} is the solute electron density for the state I and ρ_{IJ} the transition density between the states I and J, respectively. The electrostatic interaction energy is conveniently rewritten into the multi-pole expression after expanding

the potential v(x) by the power series of coordinate x. For a polar molecule the most dominant term of this expansion is the first order term. Then the diagonal element V_{II} is expressed in terms of the dipole moments and the off-diagonal element V_{IJ} by the transition moments. The I-th electronic state of solute is thus largely modified by mixing with the J-th state through the interaction with solvents when the transition moment to the state J is large and the energy difference is small.

It was found that the second and third excited states, S_2 and S_3 state, strongly couple by the electric field from solvent molecules because the transition moment between these state is large and strongly depends on the amino torsional angle τ. The S_2-S_3 transition moment increases with twisting the dimethylamino group and takes the maximum value of 4.3 D, the same order of magnitude dipole moment itself, at $\tau = 73^{\circ}$ (see Fig. 7). These states are found to be mainly described by the combinations of three electronic configurations,

$$\cdots\cdot(4b_1)^2(1a_2)^2(5b_1)(6b_1), \tag{7a}$$

$$\cdots\cdot(1a_2)^2(5b_1)^2(4b_1)(6b_1), \tag{7b}$$

and

$$\cdots\cdot(4b_1)^2(5b_1)^2(1a_2)(2a_2), \tag{7c}$$

at the planar geometry and correlate to the 1^1A_2 and 2^1A_1 states of the perpendicular form. The relative contributions of these configurations in the CI wave functions change along the torsion-

al coordinate.

We constructed here the diabatic representation of potential energy surfaces for these states which are stable to the electric field from solvent molecules in order to facilitate the calculations in a polar solvent. The successive two step unitary transformations of the CI wave functions calculated with the Basis A were carried out to diminish the transition moment and the three diabatic states, D_1, D_2, D_3 state, were obtained as the basis functions representing the S_2 and S_3 states. The supplementary S_4 state was also provided.

The diabatic states defined here have a simple physical interpretation. The D_1 state corresponds to the CT state configuration and the D_2 and D_3 states to the local $\pi-\pi^*$ excited state configurations in the benzonitrile moiety. In the adiabatic representation the main component of S_2-S_3 transition moment is the off-diagonal element of MO's which are given by the plus and minus combinations of amino lone pair and aromatic π orbital ($4b_1$ and $5b_1$ MO in Fig. 2). These MO's are transformed into the orbitals localized at the separated sides of molecule, i.e. the N lone pair and π orbital, respectively. Thus the transition moment between the D_1 and D_2 state becomes very small. The D_3 state is the $1a_2$-$2a_2$ $\pi-\pi^*$ locally excited configuration where two electrons are differently occupied from the D_1 and D_2 state.

The diagonal elements of diabatic state potential energy matrix were least square fitted to the analytical function (eq. 1). The off-diagonal terms of D_1 state with the D_2 and D_3 state were represented by the function

$$D_{IJ}(\tau, \theta) = (b_1 \cos\tau + b_3 \cos 3\tau) \cos\theta , \qquad (8)$$

and the D_2-D_3 off-diagonal element was by

$$D_{IJ}(\tau, \theta) = (b_0 + b_2 \cos 2\tau + b_4 \cos 4\tau) \times (1 - c + c \cos\theta) \qquad (9)$$

respectively.

As seen in Table II, the energy of CT state (1^1A_2) is lowered by the calculations with the Basis B at the 90° twisted geometry and becomes the second excited state while the change of relative energies at the planar geometry is small. We modified the diagonal elements of the energy matrix by adding the correction terms, $a + b\cos 2\tau$, as in the case of S_0 and S_1 states. It was found that the D_1-D_2 off-diagonal element needs to be reduced by multiplying the scale factor of 0.9 to reproduce the energies and the relative weights of electronic configurations of S_2 and S_3 states calculated with the Basis B. Fig. 4 shows the diagonal

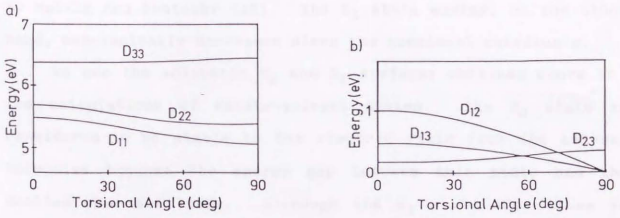

Fig.4 Diagonal and off-diagonal Hamiltonian matrix elements of diabatic states at θ=0°. Diagonal elements are in (a) and off-Diagonal ones in (b), respectively.

and off-diagonal matrix elements of the diabatic states at θ =0°. The D_1 and D_2 state energies are close and decrease with increasing the torsional angle while the D_3 potential surface slightly increases. The off-diagonal element between the D_1 and D_2 state is considerably large at the planar, 1.0eV, and declines with twisting to the perpendicular geometry. The planar S_2 energy is lowered by this term. The parameters of potential energy functions for these diabatic states are tabulated in Table V.

We calculated the adiabatic potential energy surfaces by diagonalizing the Hamiltonian matrix for the diabatic states obtained here and the resultant potential energy surfaces are shown in Fig. 5. The potential surface features of S_2 state in Fig.3(a) are somewhat different from those imagined to interpret the TICT state in the literatures (1). The S_2 energy has been conveniently regarded to be a decreasing function of amino internal rotation angle τ. The present calculations show, however, that the energy at the perpendicular geometry is higher than that of the planar. This qualitatively agrees with the calculations by Rettig and Koutechy (23). The S_3 state energy, on the other hand, monotonically decreases along the torsional coordinate.

We use the adiabatic S_0 and S_1 surfaces obtained above in the calculations of solute-solvent system. The S_0 state is considered to be stable to the electric field from the solvent molecules because the energy gap between this state and the excited ones are large. Although the S_1 state lies close in energy to the S_2 and S_3 state, the calculated S_1-S_2 and S_1-S_3 transition moments were small and their directions were perpen-

dicular to the z-axis. Since the solvent charge distribution is symmetric in the directions of transition moments, the solute-solvent interaction coming from these transition moments will be canceled out in the equilibrium solvation. The profiles of gas phase potential energy surfaces of DMABN at $\theta = 0^{\circ}$ are shown in Fig. 6.

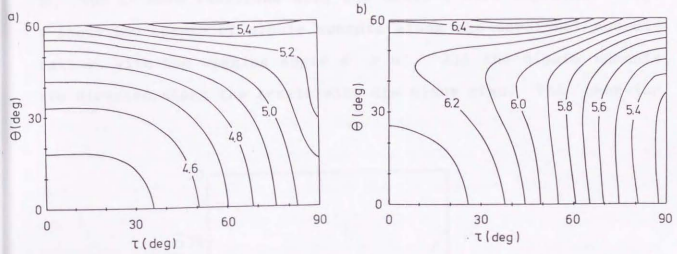

Fig.5 Contour maps of potential energy surfaces of S_2 and S_3 states. Potential surfaces of S_2 and S_3 states are given in (a) and (b), respectively.

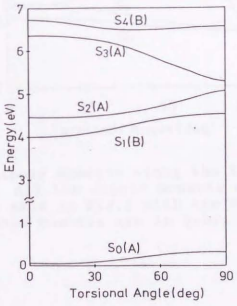

Fig.6 Profiles of gas phase potential energy surfaces at $\tau = 0^{\circ}$. All the states are assigned in terms of C_2 symmetry although the methyl groups break the C_2 symmetry.

2-2-4. Dipole Moments

The red shifts of fluorescence spectra of DMABN have been related to the difference of dipole moments between the excited and ground state. The Lippert-Mataga equation (27) has been utilized to qualify these red shifts. We calculated the dipole moments for the ground and excited states as a function of τ and θ. The CI wave functions with the Basis A were employed. Fig. 7 shows the change of dipole moments along the torsional coordinate τ with the wagging angle θ = 0°. All the dipole moments are directed along the z-axis with the minus sign. The behavior

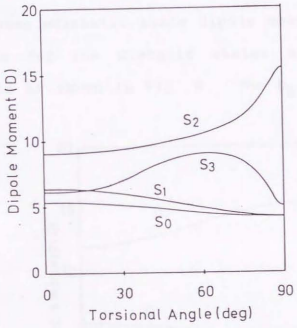

Fig.7 Changes of dipole moments along the torsional coordinate with θ=0°. All the dipole moments are directed to the molecular z axis in Fig.1 with the minus sign. Unit of dipole moments are in Debye.

of dipole moment functions for the other values of θ was essentially the same as in Fig. 7. The dipole moments for S_0 and S_1 state were calculated to be 5.4 and 6.4 D at the planar geometry, which are underestimated than the experimental values, 7.6 and 9.1 D (28). However, the difference of dipole moments between these two states, 1.0 D, is comparable to the experiments. The S_0 and S_1 dipole moments gradually decrease with the NC internal rotation and become nearly the same value, 4.2 D, at the 90° twisted geometry. As seen in Fig. 7, the S_2 state dipole moment gradually increases at the region $0° < \tau < 70°$ and then rapidly grows up. This reaches the CT state dipole moment finally. The S_3 state dipole moment curve has the maximum at $\tau = 62°$. In contrast to these adiabatic state dipole moments, the changes of dipole moments for the diabatic states are small along the torsional angle as shown in Fig. 8. The D_2 and D_3 state dipole

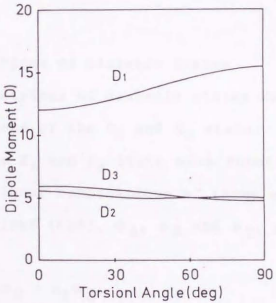

Fig.8 Changes of dipole moments of diabatic states along the torsional coordinate with θ=0°. All the dipole moments are directed to the molecular z axis with the minus sign. Unit of dipole moments is in Debye.

moments are almost constant and their magnitudes are similar to those of S_0 and S_1 state. Only the D_1 state dipole moment is large and monotonically increases with the degree of internal rotation.

The dipole moment of CT state has been estimated from the measurements of fluorescence shifts in various solvents with different polarities. Although the estimated values depend on the Onsager's cavity radius inherent to the Lippert-Mataga model, one of the recommended values is ~ 16 D (29), about three times larger than the S_0 state dipole moment, with the cavity radius of 4 A. The present calculations gave the CT (1^1A_2) state dipole moment of 15.5D. The dipole moment of $\pi-\pi^*$ locally excited state at τ = 90° was calculated to be 5.0 D.

2-2-5. Density matrices of Diabatic States

The density matrices of diabatic states were calculated from the CI wave functions of the S_2 and S_3 state. For this purpose, we assumed that the S_2 and S_3 state wave functions, Ψ_I and Ψ_{II}, are expressed as linear combinations of three electronic configuration state functions (CSF), Φ_A, Φ_B and Φ_C, given in eq. 7 as

$$\Psi_I = a_1\Phi_A + b_1\Phi_B + c_1\Phi_C \qquad (10)$$

and

$$\Psi_{II} = a_2\Phi_A + b_2\Phi_B + c_2\Phi_C \qquad (11)$$

because these states are mainly described by the three configurations, A, B and C.

The density matrices in terms of the configurations A and B are easily derived from eqs. 10 and 11 as

$$\rho_{A,A} = \{b_{22}\rho_{I,I} - 2b_1b_2\rho_{I,II} + b_{12}\rho_{II,II} - (b_1c_2 - c_1b_2)^2\rho_{C,C}\}/N \quad (12)$$

$$\rho_{B,B} = \{a_{22}\rho_{I,I} - 2a_1a_2\rho_{I,II} + a_{12}\rho_{II,II} - (a_1c_2 - c_1a_2)^2\rho_{C,C}\}/N \quad (13)$$

and

$$\rho_{A,B} = -\{a_2b_2\rho_{I,I} - (a_1b_2 + a_2b_1)\rho_{I,II} + a_1b_1\rho_{II,II} - (a_1c_2 - c_1a_2)x(b_1c_2 - c_1b_2)\ \rho_{C,C}\}/N \quad (14)$$

with

$$N = (a_1b_2 - b_1a_2)^2,$$

where $\rho_{I,I}$, $\rho_{II,II}$ and $\rho_{I,II}$ are the densities of S_2 and S_3, and the transition density between these states, respectively. The density $\rho_{C,C}$ is for the configuration C. In deriving eqs. 12 to 14, the transition densities $\rho_{A,C}$ and $\rho_{B,C}$ were put to be zero because two electrons are differently occupied in the configuration C from A and B.

The diabatic state densities, $\rho_{1,1}$ and $\rho_{2,2}$, were then

calculated by diagonalizing the 2 x 2 z-component dipole moment matrix,

$$\begin{bmatrix} \mu_{A,A} & \mu_{A,B} \\ \mu_{B,A} & \mu_{B,B} \end{bmatrix} \qquad (15)$$

the density $\rho_{3,3}$ is the same as $\rho_{C,C}$.

In calculating eqs. 12 to 14 the coefficients of CSF's in the wave functions were taken from the CI wave functions, where the coefficients are renormalized after eliminating the contributions from the other CSF's. The density $\rho_{C,C}$ was represented by

$$\rho_{C,C} = \sum_{i,j} \gamma_{i,j} \phi_i \phi_j \qquad (16)$$

using the MO's ϕ_i and the coefficients $\gamma_{i,j}$ were obtained by diagonalizing the dipole moment matrix at the perpendicular geometry. The same coefficients $\gamma_{i,j}$ were used for the other geometries.

The energy matrix elements in the diabatic state representation were obtained to reproduce the adiabatic energies and relative contributions of three CSF's in the wave functions.

2-2-6. Solute-Solvent Interaction Potential

We assumed that the DMABN-H2O intermolecular potential is composed of the electrostatic (Coulomb) and the exchange-exclusion potential. Although the Mulliken atomic populations are sometimes used for the effective charges on atoms, the dipole moments calculated with the Mulliken charges were only 60-70 % of ab initio values. We therefore developed a different method. In order to determine the electrostatic term of the interaction potential, we calculated the electrostatic potential as a function of x', the position of test charge,

$$V(x') = \int \rho(x)\, e^2/\, |x'-x|\, dx + \sum_N Z_N e^2/\, |x'-X_N| \qquad (17)$$

where X_N and Z_N are the nuclear coordinates and charge of atom N in DMABN. The calculations were carried out at about 500 points of x' for each the geometry of DMABN. The density matrix $\rho(x)$ was constructed from the CI wave function (Basis A) for each state. The density matrices of diabatic states were obtained by the method discussed above. The effective charges located on the atoms of DMABN were next determined so as that calculated electrostatic potentials are represented by the sum of Coulombic interactions between the effective charges and the test charge at x'. The contributions from the methyl groups were represented by the effective charges on the methyl C atoms. The least square fitting was carried out under constraint that the ab initio dipole moments are reproduced. The electrostatic potential thus obtained contains the contributions from the multi-pole moments

more than the dipole. In Table III, the effective charges of S_0 and S_1 at the planar geometry and of the three diabatic states at

Table III. Effective charges on the atoms

Atom	S0[a]	S1[a]	D1[b]	D2[b]	D3[b]
N_1	-0.2627	-0.1379	0.7130	-0.2950	-0.1044
C_8	0.1360	0.1449	0.0782	0.1082	0.0646
C_1	0.0681	0.0314	-0.1903	0.0763	0.1094
C_2	-0.1041	-0.0800	-0.4327	-0.0345	-0.0628
C_3	-0.1804	-0.1767	-0.3229	-0.1615	-0.1606
C_4	0.0407	0.0744	0.4619	0.0871	0.0852
C_5	0.2643	0.2184	-0.1331	0.1464	0.2084
N_2	-0.4047	-0.3482	-0.3478	-0.3652	-0.3750
H_1	0.1167	0.0503	0.1933	0.0969	0.0550
H_2	0.1788	0.1422	0.2323	0.1660	0.1420

a) Planar geometry.

b) Perpendicular geometry.

the 90° twisted geometry are summarized. We can see from the Table that the D_1 state is strongly polarized at τ = 90°, the effective charge of dimethyl amino moiety is 0.87e, while the other states are of neutral type. The effective charges calculated at various geometries of DMABN are fitted to the analytical functions. The details will be presented later.

The Gordon-Kim (GK) (29) model was applied to obtain the exchange-exclusion potential. The interaction energy between two molecules is calculated by

$$V_{ex}(R_{ab}) = \int dx \{[\rho_a(x) + \rho_b(x)]E_G(\rho_a+\rho_b) - \rho_a(x)E_G(\rho_a) - \rho_b(x)E_G(\rho_b)\} \quad (18)$$

where $\rho_a(x)$ is the density matrix of one molecule and $\rho_b(x)$ of the other, respectively. The energy density $E_G(\rho)$ is given by

$$E_G(\rho) = 3/10(3\pi^2)^{2/3}\ \rho^{2/3} - 3/4(3/\pi)^{1/3}\ \rho^{1/3} \quad (19)$$

The electron density of DMABN was expressed as a superposition of atomic density ρ_N

$$\rho_{DMABN}(x) = \sum_N n_N \rho_N(x), \quad (20)$$

with n_N the effective number of electrons on the atom N, determined above, and the atomic density is approximated by

$$\rho_N(x) = \sum_m C_m |x - X_N|^m \exp(-\alpha_m|x-X_N|) \quad (21)$$

which is obtained by a least square fitting to the electron density of isolated atom. The densities of CH_3 groups and CH in the aromatic ring are regarded as the extended atoms. The coefficients C_m were reoptimized by the least square fitting of electron density distributions calculated for each state to eq. 20. The electron density of H_2O was also represented by eq. 21. In calculating the GK exchange-exclusion potential, we introduced an

approximation that the total interaction energy is given as the sum of contributions of pair potentials between H_2O and the atoms or extended atoms in DMABN. This approximation enabled us to use a simple integration scheme in evaluating eq. 18. The 24 * 24 point Gauss-Laguerree and Gauss-Legendre numerical quadrature was employed. The pair exchange-exclusion potentials are finally fitted to the function

$$V_{ex}(R_{ab}) = A \exp(-BR_{ab}) - C/R_{ab}^{6} \qquad (22)$$

where R_{ab} is the distance between an atom in DMABN and the O atom of H_2O, to facilitate the simulation calculations. It was found that the pair exchange-exclusion potentials are insensitive to the change of DMABN geometry. We therefore ignored the τ and θ dependence of potential and used the parameters determined at the planar geometry.

The DMABN-H_2O intermolecular potentials were given as the sum of Coulombic and exchange-exclusion terms. For the Coulombic part, the τ and θ dependence of effective charge on the atoms in DMABN was represented by the function

$$q^i(\tau, \theta) = (a_0{}^i + a_2{}^i\cos 2\tau + a_4{}^i\cos 4\tau + a_6{}^i\cos 6\tau) \times (1-c+c\cos\theta), \qquad (23)$$

since q^i was relatively insensitive to the angle θ compared to the angle τ. The coefficients, $a_n{}^i (n = 0,2,4,6)$, were first determined for the geometries with $\theta = 0^\circ$ and the parameter c was then obtained.

2-2-7. DMABN-H_2O complex

The geometries of DMABN-H_2O complex were optimized by using the potential functions developed here. We chose the effective charges of 0.41e for the H atoms and -0.82e for the O atom in H_2O to calculate the DMABN-H_2O electrostatic potentials. The results are summarized in Table IV. We found four different types of stable configurations for the S_0 state and illustrated them in Fig. 9. One of the H atoms in H_2O is coordinated to the amino N atom and the other toward to the aromatic ring in the type A configuration. The H_2O molecule is located perpendicular to the aromatic ring and lies on the x-z plane. The binding energy for this complex was 2.70 kcal /mol. The type B configuration is

Table IV. Binding energies of DMABN·H2O complex in the S_0 and S_1 state[a)]

Type[b)]	S_0	S_1
A	2.70	3.20
B	2.89	...
C	3.73	3.65
D	4.26	3.89

a) Energies are given in kcal/mol.

b) See Fig.9 for the configuration types.

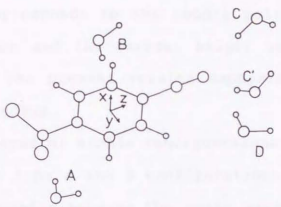

Fig.9 Nuclear configurations of H_2O coordinated to DMABN in DMABN·H2O 1:1 complex.

resemble to the type A; H_2O suited on the x-z plane. Both the H atoms interact more strongly with the aromatic carbons than the amino N atom in this case. The binding energy, 2.89 kcal/mol, of type B was slightly larger than the type A binding energy. The type C and D are characterized by a strong hydrogen bonding to the terminal N atom of CN moiety. The H_2O molecule is also on the x-z plane and the binding energy is 3.73 kcal/mol in the type C. The most stable configuration is type D with the binding energy of 4.26 kcal/mol. In contrast to the other complexes, H_2O suited on the same plane as the aromatic ring, the y-z plane. The O atom is coordinated to the atom attached to the aromatic carbon with a strong N-H hydrogen bonding.

Warren et al. (17) have calculated the geometries of DMABN-H_2O system using the empirical interaction potentials. Their results are somewhat different from ours. H_2O is located parallel to the aromatic plane as in the benzene-H_2O complex at their

most stable configuration. In the present calculations, this geometry corresponds to the saddle point leading to the type B configuration and the barrier height was calculated to be 0.49 kcal/mol. The present results emphasize the importance of N-H hydrogen bonding.

Three types of stable configurations were obtained at the S_1 state. The type A and B configurations of S_0 state resulted in the same geometry because the amino wagging angle is very small, 6°, in this case. The changes of H_2O location upon the S_0-S_1 excitation were small for the type C and D complex and the wagging angle became nearly equal to zero. As seen in Table IV, the H_2O binding energy of S_1 state are larger than those of S_0 state for the type A and B. The configurations C and D, on the other hand, exhibit blue shifts upon the excitation. This is due to the decrease of local bond dipole of terminal CN group in the S_1 state as seen in Table III, where the effective charge on the cyano N atom is -0.35e in the S_1 state and -0.40e in the S_0 state at the planar geometry. Several authors have observed the blue shifts of fluorescence spectra in the supersonic jet experiments on the DMABN-H_2O complex (16,17). The present calculations yield the blue shifts of 28 and 129 cm^{-1} for the more stable type C and D complex, which are in good agreement with the experimental values by Warren et al (19), 14 and 199 cm^{-1}, respectively. It should be mentioned, however, that more extensive MO calculations would be required to confirm the present results considering the approximations introduced in the present work.

For the S_2 state, two stable positions of H_2O were found;

one is coordinated to the amino N and the other to the cyano N atom. The torsional angles of amino group were about 45° for both the complex. The binding energies were 4.58 and 5.18 kcal/mol, respectively. In addition to these configurations, we found the dipole-dipole type complex, in which the H_2O dipole is oriented to the direction of z-axis from the side of amino group. The binding energy was 2.66 kcal/mol. In spite of larger stabilization energies, the energies of S_2 DMABN-H_2O complexes were still far above the S_1 energies. This result is consistent with the experimental finding that the CT state formation is not achieved under the isolated molecular beam conditions.

2-3. Equilibrium Solvation

2-3-1. Monte Carlo calculations

Monte Carlo simulation calculations were carried out on a DMABN molecule solvated in water. The potential energy of this system are calculated by the DMABN intramolecular and the DMABN-H_2O intermolecular potential functions developed in section 2-2. For the S_0 and S_1 state, the potential energies are given as the sum of three terms;

$$W_I(\tau, \theta, R; r, \Omega) = E_I^{solute}(\tau, \theta) + E_I^{int}(\tau, \theta, R; r, \Omega) + E^{solv}(r, \Omega) \quad (24)$$

where the first term is the potential energy of isolated DMABN in its I-th electronic state, the second the DMABN-solvent interaction energy, and the third the solvated energy, respectively. The solute energy is assumed to be the function of two internal coordinates, τ and θ. We used the simple point charge (SPC) model (31) to describe the H_2O-H_2O intermolecular interaction. The interaction energy is constituted of the Coulombic potentials between the effective charges placed on the atoms and the 12-6 Lennard-Jones potential between the O atoms. The effective charges are 0.41e for the H atom and -0.82e for the O atom, respectively. The length and energy parameters of the Lennard-Jones potential are taken to be 3.1656 Å and 0.1554 kcal/mol. The solvent H_2O molecule is regarded as a rigid body in the calculations. Thus the solvent energy E^{solv} is given as the function of a set of solvent center of mass coordinates r and

orientation angles Ω. The solute-solvent interaction energy E_I^{int} depends on the solute coordinates, τ, θ, and R as well as the solvent coordinates, r and Ω. R denotes the center of mass and Euler angles to determine the orientation of DMABN molecule.

As shown in the previous section, the S_2 state is described as a superposition of three diabatic states and the weights of these states in the wave function strongly influenced by the solute-solvent interaction. We therefore constructed the Hamiltonian matrix

$$H_{KL}(\tau, \theta, R; r, \Omega) = D_{KL}(\tau, \theta) + \delta_{KL} V_K^{int}(\tau, \theta, R; r, \Omega) \quad (K, L = 1, 2, 3) \qquad (25)$$

and solved the secular equation

$$H C = \lambda C \qquad (26)$$

to obtain the S_2 state energy. In eq. 25 D_{KL} is the energy matrix element between the K and L-th diabatic states and V_K^{int} the solute-solvent interaction energy of S_2 state are thus given as the sum of the lowest eigenvalue of eq. 26 and the solvent energy. We further defined the S_2 state solute and solute-solvent interaction energy for the later analyses as

$$E_2^{solute}(\tau, \theta) = \sum_K \sum_L C_K C_L D_{KL}(\tau, \theta) \qquad (27)$$

$$E_2^{int}(\tau, \theta, R; r, \Omega) = \sum_K C_K^2 V_{Kint}(\tau, \theta, R: r, \Omega) \qquad (28)$$

where C_K (K =1,2,3) is the eigen vector corresponding to the lowest eigenvalue of eq.26.

Calculations were carried out for the system composed of a DMABN and 350 water molecules, enough to describe the bulk solvent partitioning in the solvation, in the NVT ensemble at 25 °C. The density was taken to be 1.0 g/cm^3. The cubic periodic boundary conditions were employed and the length of box side was thus 22.0 Å. In calculating the interatomic potentials, spherical cutoffs of potential with the cutoff length was taken from the half of box length used in a conventional 216 water simulation with the density of 1.0 g/cm^3.

Since we allowed to move the internal coordinates of DMABN, τ and θ, as well as the translational and rotational coordinates in the simulations, the appropriate volume element is required for the coordinate space integration. The Jacobian of transformation from the Cartesian coordinate system to the molecular fixed coordinates, τ, θ and R is given by

$$J(\tau, \theta, \gamma) = |I(\tau, \theta)|^{\frac{1}{2}} \sin\gamma \qquad (29)$$

where γ is the Euler angle to determine the orientation of molecular z-axis. The 5*5 inertia tensor $I(\tau, \theta)$ is for the rotations around the molecular axes and the internal coordinates, τ and θ. Thus the probability for the move of DMABN from the m-th configuration to the n-th one is

$$P_{mn} = \exp\{-\beta(W_n - W_m)\}J(\tau_n, \theta_n, \gamma_n)/J(\tau_m, \theta_m, \gamma_m) \qquad (30)$$

with $\beta = 1/k_B T$.

We employed the importance sampling (32) to calculate the potentials of mean force, the relative free energy curves, for the S_0, S_1 and S_2 state. The torsional angle τ of dimethylamino group was chosen as the coordinate. The imposed umbrella potentials were taken to be

$$U_i(\tau) = f_i(\tau - \tau_i)^2 - E_I^{solute}(\tau, 0^\circ) \qquad (31)$$

for the S_0 and S_1 state, and

$$U_i(\tau) = f_i(\tau - \tau_i)^2 \qquad (32)$$

for the S_2 state, respectively. The umbrella potential was added to all the diagonal elements of diabatic state potential functions in the simulations for S_2 state. We carried out the simulation calculations at 5 ~ 6 different windows of τ for each electronic state and obtained the probability distributions of τ at each window. The potential of mean force was then calculated by combining the distributions at different overlapping regions into a single distribution.

For each simulation calculation, the averaging of 2000 - 4000 K configurations were performed after the equilibration run of 3000 - 5000 K configuration steps. New configurations were generated in the usual Monte Carlo manner and the acceptances of new configurations was according to the Metropolis test with the

appropriate modifications for each sampling scheme. The solute moves were attempted every 50th configurations. The ranges of move for the geometric parameters were determined so that the acceptance ratio becomes about 45 %.

2-3-2. Potential of Mean Force

The potentials of mean force for the angle τ are shown in Fig. 10. The solution phase S_0 energy curves monotonically increases with twisting of dimethylamino group and reaches to the maximum at τ = 90° as in the gas phase curve. The barrier height in the solution, 6.1 kcal/mol, is almost the same as that of gas phase. The S_1 state energy curve also rises with the internal rotation. The solution phase barrier height, 12.9 kcal/mol, is slightly higher than the gas phase one by 0.8 kcal/mol. The increase of S_1 state barrier heights in the solution can be rationalized from the results that the dipole moments of S_1 state decrease with the degree of internal rotation and the difference of dipole moment between the planar and the perpendicular geometry is larger in the S_1 state than in the S_0 state as seen in Fig. 7.

The S_2 energy curve in the solution presented in Fig. 10(c) is much different from the gas phase energy profile. The potential energy is very flat and gradually decreases with the internal rotation. Although the 90° twisted geometry corresponds to the top of barrier on the S_2 surface in the gas phase, it became a stable point due to the solvation and is lower in energy than the planar geometry by 2.0 kcal/mol. This result is consistent

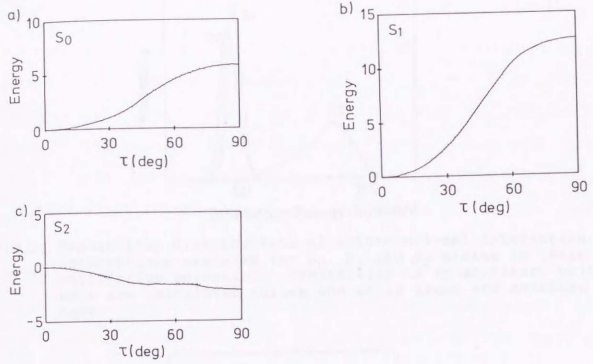

Fig.10 Potentials of mean forces for the torsional coordinate. Potentials for S_0, S_1, S_2 states are given in (a), (b), and (c), respectively. Dots are calculated values and solid lines are smoothed ones.

with the conjecture derived from the experiments that the TICT state is formed when the DMABN molecule is excited in polar solvents.

In order to see the effect of solvation on the potential energy profiles, we compared the energy components of solute-solvent system for each electronic state. The distributions of solute-solvent interaction energies are shown in Fig. 11. For the S_0 and S_1 state, the energies distribute at the range 40.0 - 60.0 kcal/mol and the average interaction energies are about 50 kcal/mol. The S_2 state shows very broad distribution of interaction energy compared to the S_0 and S_1 state. This is because the S_2 state potential of mean force is very flat and the torsional angle distributes in a wide range. Fig. 12 shows the changes of

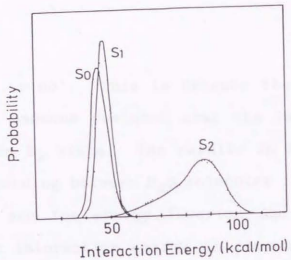

Fig.11 Probability distributions of solute-solvent interaction interactions energies for S_0, S_1 and S_2 states in their equilibrium solvation. Probability is in arbitrary unit. Dots are calculated values and solid lines are smoothed ones.

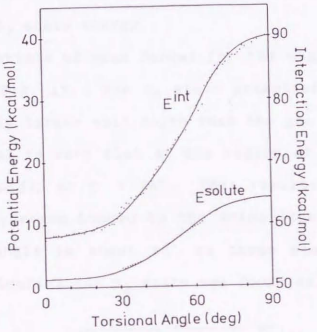

Fig.12 Changes of averaged S_2 state solute potential energy and solute-solvent interaction energy given as a function of the torsional angle in the equilibrium solvation. Dots are calculated values and solid lines are smoothed ones.

averaged solute potential and solute-solvent interaction energy of S_2 state along the torsional coordinate. The solute-solvent interaction remarkably increases with twisting the dimethylamino group compared to the solute potential energy and becomes 90.1

kcal/mol at $\tau = 90^{\circ}$. This is because the contribution of ion pair D_1 state becomes dominant near the region of 90° twisted geometry in the S_2 state. The results in Fig. 12 indicate that the hydrogen bonding between H_2O molecules is weaken with forming the CT state and the energy lowering due to the increase of solute-solvent interaction energy is compensated by the changes of solute potential and solvent-solvent hydrogen bond energies to bring the very flat S_2 state potential of mean force in Fig. 10(c). The changes of solute-solvent interaction energies of S_0 and S_1 state are, on the contrary, found to be very small compared to the S_2 state energy.

The potentials of mean forces for the wagging coordinate θ are shown in Fig. 13. The S_0 state potential is a double well with a slightly larger well depth than the gas phase one. The S_1 state potential is very flat at the region of $0^{\circ} < \tau < 25^{\circ}$ and rises very rapidly at $\tau > 25^{\circ}$. This results indicate that H_2O is strongly hydrogen bonded to the amino lone pair orbital when the wagging angle is about 20° in these states. The wagging angle mean potential for S_2 state was found to be a single well.

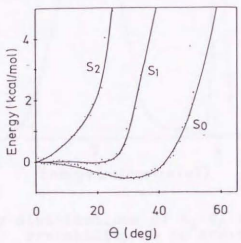

Fig.13 Potentials of mean force for wagging angle. Dots are calculated values and solid lines smoothed ones.

2-3-3. Photoemission Profiles

In order to examine the effect of solvation to the photoemission spectrum profiles, we calculated the probabilities

$$P_{0<-I}(\Delta E) = < \delta (W_I - W_0 - \Delta E)>_I \qquad (I=1,2) \qquad (32)$$

where W_I is the potential energy of the state I and W_0 of the S_0 state, respectively. The ensemble average $<\cdots\cdots>_I$ stands for the integration over the solute and solvent configuration in the equilibrium solvation for S_I state. The probability given by eq. 32 approximately represents the intensity profile for the transition from the S_I state to S_0 under the assumption that the vertical electronic transition occurs at the classical turning point.

Fig. 14 shows the calculated energy difference distributions. The S_1-S_0 distribution curve is centered at 4.0 eV and

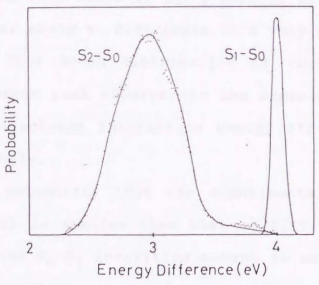

Fig.14 Probability distributions of S_1-S_0 and S_2-S_0 energy difference. Probability is in arbitrary unit. Dots are calculated values and solid lines smoothed ones.

its half width of 0.1 eV. THe S_2-S_0 energy difference curves covers a broad range of energy and has the maximum at 2.9 eV. The half width of this peak was calculated to be 0.7 eV.

The excited state DMABN is known to exhibit dual fluorescence in polar solvents. In many experimental studies, the band with a shorter wavelength has been attributed to the emission from the locally excited (LE) state and the very broad one with a longer wavelength is to that from the TICT state. The results presented in Fig. 14 seem to well reproduce the essential features of typical emission spectra of DMABN in polar solvents. The S_0-S_1 transition corresponds to the emission from the LE state. The position and width of this peak is expected to be rather insensitive to the solvent polarity since the dipole moment of S_1 state is close to that of S_0 state. The broad peak at a longer wavelength region is attributed to the emission from the S_2 state. Although this peak is considered to be the emission from the TICT state is not a pure CT state with $\tau = 90^\circ$ and the torsional angle τ distribute in a very wide range as seen in Fig. 10. This broad distribution of torsional angle is the origin of broad peak observed in the experiments because the S_2 state solute-solvent interaction energy strongly depends on the torsional angle.

It is noteworthy that the experimental intensity of LE emission peak is smaller than that of TICT state. This is because that the S_0-S_1 transition moment is much smaller than that of S_0-S_2 transition.

2-4. Mechanism of CT State Formation

2-4-1. Theoretical model

It is convenient to describe chemical reactions in solution in terms of the reaction free energy surface. For the electron transfer reactions where the solvent dielectric relaxation plays an important role, the reaction surface is usually defined as the function of the solvation coordinate representing the solvent orientation polarization (33). Although there are several ways to choose the solvation coordinate (33-35), we have taken the difference of potential energies between the S_1 and S_2 state,

$$s = f(\tau, \theta, R, r, \Omega) \tag{33}$$

with

$$f(\tau, \theta, R, r, \Omega) = \beta\{W_1(\tau, \theta, R, r, \Omega) - W_2(\tau, \theta, R, r, \Omega)\} \tag{34}$$

as the solvation coordinate s. With this definition the potential energies of two states coincide each other at the transition state, s=0.

The magnitude of solute-solvent interaction in DMABN-H_2O system strongly depends on the torsional coordinate particularly in the S_2 state as mentioned above. Therefore it is important to include the effect of intramolecular coordinates to describe the CT state formation process of DMABN. Actually, based on the experimental results by the time resolved emission spectroscopy, Su and Simon (13) have pointed out the importance of fluctuation of intramolecular vibrations in determining the rate of CT state formation.

We constructed the reaction free energy surfaces F_I using

the relation

$$F_I(s,\tau) = -\beta^{-1}\ln P_I(s,\tau) + C \quad (I = 1,2) \tag{35}$$

where the probability $P_I(s,\tau)$ is given by

$$P_I(s,\tau) = \int \delta\{f(\tau, \theta, R, r, \Omega) - s\}\, \delta(\tau' - \tau) \times \exp(-\beta W_I(\tau, \theta, R, r, \Omega))\, d\Gamma / Z_I \tag{36}$$

with

$$Z_I = \int \exp\{-\beta W_I(\tau, \theta, R, r, \Omega)\} d\Gamma \tag{37}$$

The volume element for coordinate integration is given by $d\Gamma$. It is straightforward to derive the relation from eqs. 35 to 37,

$$F_1(s,\tau) - F_2(s,\tau) = \beta^{-1}s \tag{38}$$

This implies that the only first order term of s is different between the free energy surfaces of two states when the surfaces are represented by the power series of s and τ.

In calculating the free energy reaction surfaces, the probability $P_I(s,\tau)$ was expressed by

$$P_I(s,\tau) = P_I^A(s) P^B(\tau;s) \quad (I = 1,2) \tag{39}$$

where P^B is the probability distribution function of τ at a given value of s and is the same for both the states because the

potential energies of the two states differ only by the constant value, β^{-1}s. With the use of relations,

$$F_I(s,\tau) = F_I^A(s) + F^B(\tau,s) + \ln C \tag{40}$$

$$F_I^A(s) = F_I(s) + \beta^{-1}\ln\int d\tau \ \exp(\{-\beta F^B(\tau,s)\}) \tag{41}$$

$$F_I(s) = -\beta^{-1} \ln\int d\tau \ P_I(s,\tau) \tag{42}$$

and

$$F^B(\tau,s) = -\beta^{-1} \ln P^B(\tau,s) \tag{43}$$

the reaction surface for respective state is calculated by

$$F_I(s,\tau) = F_I(s) + \beta^{-1} \ln\int d\tau \ \exp\{-\beta\Delta F^B(\tau,s)\}$$

$$+ \Delta F^B(\tau,s) \tag{44}$$

where

$$\Delta F^B(\tau,s) = F^B(\tau,s) - F^B(\tau_0(s),s) \tag{45}$$

and $\tau_0(s)$ is the value of τ at the minimum of $F^B(\tau,s)$. The second term of eq. 44 was found to be small and a slow varying function of s in the calculations presented below. By approximating $\Delta F^B(\tau,s)$ by the harmonic function

$$\Delta F^B(\tau,s) \sim 1/2\ k(s)(\tau-\tau_0(s))^2 \tag{46}$$

and neglecting the second term of eq. 44, a more simple and

useful form of the reaction surface

$$F_I(s,\tau) \sim F_I(s) + 1/2\ k(s)(\tau-\tau_0(s))^2 \qquad (47)$$

may be derived.

2-4-2. Reaction Surface

Monte Carlo calculations were carried out to obtain the reaction free energy surfaces for the nonadiabatic transition between the S_1 and S_2 state. The methods of calculations are presented in section 3-1. We first calculated the probability distribution function of s, P(s). The importance sampling was employed by imposing the umbrella potential

$$U(\tau, \theta, R, r, \Omega) = a_i\{f(\tau, \theta, R, r, \Omega) - s_i\}^2 \qquad (48)$$

to obtain uniform distribution of s. The function f was introduced in eq. 34. the calculations were carried out at 8 windows by choosing different umbrella potential parameters, a_i and s_i. The free energy curve $F_I(s)$ was obtained after combining the distributions at different windows into a single distribution. The results are presented in Fig. 15. The S_1 state free energy is a nearly parabolic function of s and has the minimum at s = -15. Much different behavior was observed for the S_2 state curve. The energy gradually decreases at the region $0 < s < 5$ and reaches the minimum at s =48. The energy of crossing point

of two curves is 4.1 kcal/mol measured from the bottom of S_1 curve and 1.4 kcal/mol from the S_2 bottom.

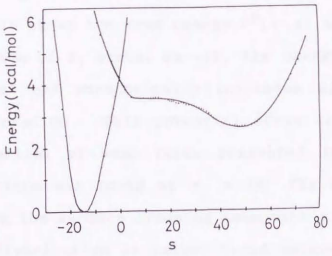

Fig.15 Free energy curves along the solvation coordinate. Energy at the minimum of S1 curve is taken to be zero. Dots are calculated values and solid lines smoothed ones

The distribution of torsional angle τ at fixed values of s, $P^B(\tau,s)$, were next calculated to obtain the free energy $F^B(\tau,s)$. We employed the umbrella potential of the form

$$U(\tau,\theta,R,r,\Omega) = a_i \{\beta f(\tau,\theta,R,r,\Omega) - s_i\}^2 + b_j(\tau-\tau_j)^2 \quad (49)$$

The first term was introduced to ensure that the difference of potential energies of two states distributes in a very small range around the given value of s_i. The parameter a_i was chosen to be 5000.0, which gave very small value of the root mean square of the energy difference, $\langle(W_1-W_2)^2\rangle^{1/2}$. For example, this was smaller than 0.01 kcal/mol at $s_i = 0$. The second was to ensure uniform sampling for the angles τ. The calculations were car-

ried out at 8 points of s_i (-25,-15,-5,0,10,30,48 and 70). For each value of s_i we performed the simulations at 5 ~ 8 windows, corresponding to different choices of the parameters b_j and τ_j.

Fig. 16 shows the free energy $F^B(\tau, s)$ at s = -15, 0 and 48. At the bottom of S_1 state, s= -15, the energy F^B has the minimum at τ = 0° and monotonically increases along with the amino internal rotation. This potential curve is resemble to the S_1 state potential of mean force presented in Fig. 10(b). The energy minimum was found at τ = 25° for the potential energy curve along the surface crossing seam with s = 0. The torsional angle τ distribution is rather broad because the curve is flat as seen in Fig. 16. The TICT state becomes the minimum energy

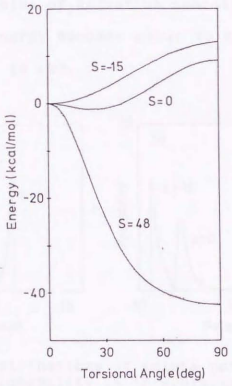

Fig.16 Free energy curves along the torsional coordinate at s=-15,0,48. Energies at τ=0° are taken to be zero. Dots are calculated values and solid lines smoothed ones.

point for s = 48. Very sharp decrease of energy indicates a strong solvation near the bottom of S_2 surface. We compared the components of potential energies of solute-solvent system at s =-15, 0, 48 in Figs. 17 and 18. For the S_1 state, the distributions of solute potential energy are narrow at s =-15 and 48 compared to that at the transition state region (Fig. 17(a)). this makes the free energy curve along the crossing seam flat as seen in Fig. 16. The S_2 state solute potential energy in Fig. 17 (b) shows a similar behavior to the S_1 state. The S_1 state solute-solvent interaction energy in Fig.18(a) is peaked at 47 kcal/mol at s =-15 and the solvation becomes strong with approach to the transition state region. Although the interaction energy in the S_2 state is close to the S_1 energy at s =-15, it increases with increasing the value of solvation coordinate s. The difference of interaction energy becomes about 40 kcal/mol between s = -15 and 48 as in Fig. 18 (b).

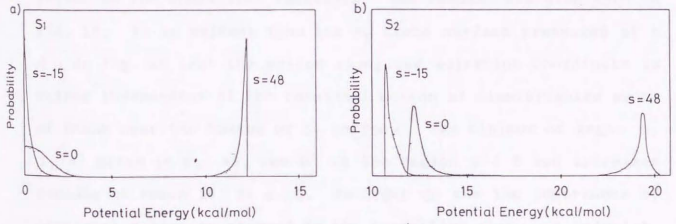

Fig.17 Probability distributions of solute potential energy at s=-15,0,48. Probability is in arbitrary unit. Energies of S_1 and S_2 states are given in (a) and (b),respectively. Energies are measured from the minimum of gas phase S_1 surface. Dots are calculated values and solid lines smoothed ones.

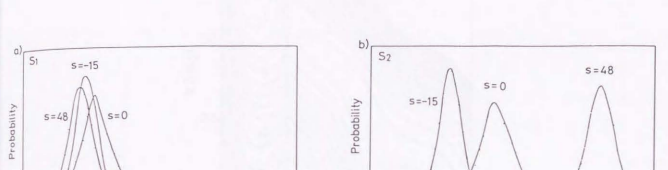

Fig.18 Probability distributions of solute-solvent interaction s=-15,0,48. Probability is in arbitrary unit. Energies of S_1 and S_2 states are in (a) and (b), respectively. Dotes are calculated values and solid lines smoothed ones.

Two dimensional reaction free energy surfaces were constructed using the relation given by eq. 44. To facilitate the calculations, the energies $F^B(\tau,s)$ and $F_I(s)$ were least square fitted to the analytical functions. the results are displayed in Fig. 19. It is evident from the S_1 state surface presented at $s < 0$ in Fig. 19 that the motion along the solvation coordinate is rather independent of the torsional motion of dimethylamino group of DMABN near the bottom of S_1 surface. The minimum of angle τ, $\tau_0(s)$ given in eq. 45, was 0° at the region $s < 8$ and increases rapidly to reach 25° at $s = 0$. In order to see the importance of torsional motion to proceed to the transition state, we calculated the steepest decent path starting from the minimum energy point on the crossing seam, $s = 0$ (36). The effective masses for s and τ motion were assumed to be unity. The reaction path is

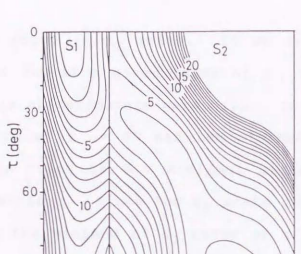

Fig.19 Reaction free energy surfaces for the CT state formation of DMABN. Energy is measured from the minimum of S_1 free energy surface. Contour spacing is 1 kcal/mol.

mainly described by the torsional coordinate at the region $0° < \tau < 18°$ and changes its main component to the solvation coordinate s at $\tau \sim 20°$. Therefore the fluctuation of torsional motion plays an important role for the CT state formation reaction. This can be also understood from the energy component distributions in Figs. 17 and 18, where the S_1 state solute potential energy increase at the transition state region. On the other hand, the solvent motion strongly couples with the torsional motion on the S_2 surface. The reaction path is described by a combination of two coordinates at the region $0 < s < 30$ and then mainly by the torsional coordinate at $s > 30$.

The shape of free energy curve $F_2(s)$ in Fig. 15 is much different from a parabolic potential usually considered to describe electron transfer reactions. This is because that the solvent motion strongly couples with the internal rotation of

dimethylamino group in S_2 state. If we see a section of free energy surface cut at a given value of τ, we can find that the energy curve is approximately parabolic. It is noted that the S_2 surface section at $\tau = 0^\circ$ has the minimum at s = -3 and the energy of this point is 5.5 kcal/mol higher than that of the bottom of S_1 surface. Since the S_2 state curve crosses with the S_1 curve near the minimum of S_2 curve at $\tau = 0^\circ$, the internal conversion to the S_1 state through the surface crossing region seems to be fast even when the solute molecule is initially excited to the S_2 state by photo-absorption.

The activation barrier for the CT state formation was calculated to be 4.1 kcal/mol. This is slightly overestimated compared to the experimental values of 2.6 4.0 kcal/mol measured in various alcohol solutions. We neglected the coupling term v for the nonadiabatic electronic transition between the S_1 and S_2 state in the present calculations. The barrier height is reduced by $|v|$ if the coupling term is included. In contrast to the experimental findings (13), the CT state formation is resulted to be the endothermic process by 2.7 kcal/mol in the present calculations. This may be due to a slight overestimation of $S_2 - S_1$ energy difference of the theoretical model employed here.

2-5. Conclusion

In the present work, we aimed to construct a realistic molecular model in describing the CT state formation of excited state DMABN in a polar solution. Ab initio CI calculations were carried out for the potential energy surfaces. The intermolecular pair potentials between DMABN and H_2O were also developed with the aid of electron distribution obtained by the calculations. Although many experimental works have been performed on the CT state formation of DMABN, the interpretations of these results have been based on hypothetical models of DMABN potential surfaces and solute-solvent interactions. As pointed out in the present work, theoretical characterization of S_2 state electronic structure is a clue to understanding the mechanism of CT state formation because this state is directly related to the TICT state at the 90° twisted geometry. The present calculations showed that the S_2 state can be described as a superposition of three diabatic states, one is of the ion pair type and the other two of the neutral ones, and the relative importance of these states are strongly affected by the amino internal rotation and the interaction with solvents.

The Monte Carlo simulation calculations for the equilibrium solvation of DMABN have revealed that the potential of mean force for the torsional angle τ is very flat in the S_2 state. Although the existence of TICT state in a polar solvent has been suggested from the experiments, the solvated S_2 state is not a pure ion pair state and the conjugation between the amino lone pair and aromatic π orbital still remains. Actually the broad

emission band experimentally observed at a longer wavelength region cannot be explained soly by the 90° twisted TICT state because the ion pair state is dipole forbidden to the ground S_0 state if the twisted molecule has the C_{2v} symmetry. Thus the broad distribution of torsional angle is the origin of broad emission band in a polar solvent. A rather narrow weak band at a shorter wavelength region was assigned to the fluorescence from the locally excited S_1 state. These conclusions were deduced from the calculations of energy difference distributions between two states.

The two dimensional reaction free energy surfaces were constructed as the functions of solvation coordinate and torsional angle. As the solvation coordinate, the difference of solute-solvent interaction energies has been conveniently chosen in the literatures (22,34). We have instead taken the difference of potential energies of solute solvent system for the solvation coordinate because the S_2 state potential energy itself is a function of solvent coordinates, r and Ω and is not separable from the solute-solvent interaction energy. We can, however, redefine the solvent coordinate by using eq. 28 as

$$s' = \beta\{f(\tau, \theta, R, r, \Omega) - (\langle E_1^{solute}(\tau)\rangle - \langle E_2^{solute}(\tau)\rangle)\} \quad (50)$$

where $\langle E_1^{solute}\rangle$ and $\langle E_2^{solute}\rangle$ are the averaged solute potential energies calculated along the crossing seam, which are presented in Fig. 20. The reaction free energy surfaces are then simply redrawn as the function of s' and τ.

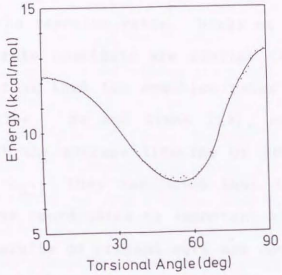

Fig. 20 Difference of averaged potential energies of S_2 and S_1 states, $\langle E_2^{solute}\rangle - \langle E_1^{solute}\rangle$, along the crossing seam, s=0, given as a function of torsional angle. Dots are calculated values and solid lines smoothed ones.

As mentioned in the previous section, the S_2 state free energy curve along the solvation coordinate given in Fig. 15 is far from a parabolic form usually assumed to describe electron transfer processes. This is peculiar to the present system where the ion pair state strongly couples with the neutral states in the S_2 state and the solvation energy becomes larger with the degree of amino internal rotation. Nonparabolic free energy curves as in the present case may be required to introduce in many other intramolecular electron transfer processes. We need to include the contribution of intramolecular degrees of freedom to elucidate the mechanism in such cases.

Dynamics of CT state formation of DMABN have been experimentally studied in a variety of polar solvents. Main interest in these works has been how the longitudial solvent relaxation time

τ_L affects the reaction rates. Hicks et al (11,12) have reported that the rate constants are similar to τ_L^{-1} in alcohol solutions suggesting that the reaction rates are controlled by solvent relaxation. Su and Simon (13), on the other hand, have observed that the average lifetime of DMABN in the LE state is faster than τ_L. They concluded that the fluctuations in the intramolecular coordinates is important than the solvent fluctuation. The results of present work are consistent with the postulate of Su and Simon. As seen in Fig. 19, DMABN is needed to undergo a deformation in the amino torsional angle to reach the transition state region. On the S_2 surface, the solvent diffusion seems to play an important role to reach the bottom of S_2 valley. Since the relaxation of torsional motion is faster than the solvent relaxation, the torsional angle is spontaneously adjusted to the solvent diffusive motion.

It is noted that the direct excitation to the S_2 state can be achieved because the photon wavelengths used in many experiments are shorter than the $S_1 - S_0$ adiabatic excitation energy and the $S_2 - S_0$ transition moment is much larger than that of $S_1 - S_0$ excitation. In such a case, the dynamics of excited state molecule becomes complicated, including the internal conversion from the S_2 to S_1 state, the diffusive motion on the S_2 surface as well as the transition from the S_1 to S_2. Although the S_2 to S_1 internal conversion seems to be fast because the surface crossing occurs near the bottom of S_2 surface at the region of small τ as seen in Fig. 19 and the vibrational relaxation is much faster than the solvent relaxation time, the TICT state can be directly

achieved from the vertically excited S_2 state without forming the S_1 state. The contribution of such process may be determined by the ratio of time scales between the solvent diffusion and internal conversion.

In this chapter, we have proposed a molecular model potentials of DMABN in a polar solvent to elucidate the mechanism of CT state formation in the excited state. The calculated solvation properties based on these potentials are in qualitatively agreement with the available experimental findings. It should be noted, however, that the present model is derived from the potential energy surfaces provided by approximate theoretical methods of the electronic structure calculations. In order to obtain quantitative results, more elaborate calculations with a larger basis set and a more accurate wave function would be required both for the DMABN potential energy surfaces and the intermolecular potentials. This is computationally unavailable for us at present because the system treated here is too large.

We have mainly focused on the static properties of DMABN in an aqueous solution in the present work. The next step would be the dynamics calculations on the reaction free energy surfaces developed here. Although the Fokker-Planck and diffusion equations have been used to treat the dynamics on the free energy surfaces of electron transfer (14,15,37), the intramolecular motions have been assumed to be separable to the solvent diffusive motion in these works. This is not the case for the present system. Molecular dynamics simulation calculations will provide a valuable information to construct the reaction diffusion equation for the CT state formation.

References

1. E. Lippert, W. Rettig, V.Bonacic-Koutecky, F.Heisel, and J.A.Miehe, Adv.Chem.Phys. ed. I. Prigogine and S. A. Rice (Wiley, New York, 1987), Vol 68, p 1.

2. D. Huppert and E.M.Kosower, Annu.Rev.Phys.Chem. 37,127 (1986).

3. M.D.Newton and M. Sutin, Annu.Rev.Phys.Chem. 35, 437 (1984).

4. J.T.Hynes, in The Theory of Chemical Reaction Dynamics, ed. M.Baer (Chemical Rubber, Boca Raton, 1986), Vol. 4, p171.

5. E.Lippert, Wluder and H.Boos, in Advances of Molecular Spectroscopy, ed. J.A.Mangini (Pergamon, Oxford, 1962), p443.

6. R.Visser, C.Varma and K.Konijnenberg and P.Bergwerf, J.Chem.Soc., Fraday Trans. II 79,347 (1983).

7. C.Cazeau-Dubroca, S.A.Lyazidi, G.Nouchi and A.Peirigua, Nouv. J. Chim. 10, 337 (1986).

8. K.Rotkiewicz, K.H.Grellmann and Z.R.Grabowski, Chem.Phys.Lett. 19,315 (1973).

9. D. Huppert, S.D.Rand, P.M.Rentzepis, P.F.Barbala, W.S.Sturve and Z.R.Grabowski, J.Chem.Phys. 75,413 (1987).

10. O.Kajimoto, M.Futakami, T.Kobayashi and K.Yamasaki, J.Phys.Chem. 92, 1347 (1988).

11. J.Hicks, M.Vandersall, Z.Babarogic, and K.Eisenthal, Chem.Phys.Lett. 116, 18 (1981).

12. J.Hicks, M.Vandersall, E.V.Sitzmann, and K.Eisenthal, Chem.Phys.Lett. 135,413 (1987).

13. S.G.Su and J.D.Simon, J.Chem.Phys. 89, 908 (1988).

14. H.Sumi and R.A.Marcus, J.Chem.Phys. 84, 4272 (1986).

15. W. Nadler and R.A.Marcus, J.Chem.Phys. 86,3906 (1987).

16. T. Kobayashi, M.Futakami, and O.Kajimoto, Chem.Phys.Lett. 130, 63 (1986).

17. J.A.Warren, E.R.Bernstein, and J.I.Seeman, J.Chem.Phys. 88, 871 (1988).

18. V.H.Grassian, J.A.Warren, E.R.Bernstein, and H.V.Secor, J.Chem.Phys. 90,3994 (1989).

19. J.K.Hwang and A.Warshel, J.Am.Chem.Soc. 109, 715 (1987).

20. R.A.Kuharski, J.S.Bader, D.Chandler, M.Sprik, M.Klein, and R.W.Impey, J.Chem.Phys. 89, 3248 (1988).

21. Y.Hatano, M.Saito, T.Kakitani, and N.Mataga, J.Phys.Chem. 92, 1008 (1988).

22. E.A.Carter and J.T.Hynes, J.Phys.Chem. 93, 2184 (1989).

23. W.Rettig and V.Bonacic-Koutecky, Chem.Phys.Lett. 62, 115 (1979).

24. W.J.Hehre, R.F.Stewart, and J.A.Pople, J.Chem.Phys. 51, 2657 (1969).

25. H.Tatewaki and S.Huzinaga, J.Comput.Chem. 1, 205 (1980).

26. P.J.Hay and T.H.Dunning, Jr, J.Chem.Phys. 64, 5077 (1976).

27. See for example, N.Mataga and T.Kubota, Molecular Interaction and Electronic Spectra (Marcel Dekker, New York, 1970).

28. P.Weisenborn, C.Varma, M.de Haas, and J.Miehe, Chem.Phys.Lett. 128, 323 (1986).

29. J.Lipinsky, H.Chojnacki, Z.R.Grabowski, and K.Rotkiewicz, Chem. Phys.Lett. 70, 449 (1980).

30. R.G.Gordon and Y.S.Kim, J.Chem.Phys. 56,3122 (1972).

31. H.J.C.Berensen, J.P.M.Postma, W.F.von Gunsteren, and J. Hermans, in Intermolecular Forces, ed. B. Pullman (Reidel, Dordrecht,1981).

32. G.N.Patey and J.P.Valleau, J.Chem.Phys. 63, 2334 (1975).

33. See for example, R.A.Marcus, Annu.Rev.Phys.Chem.15,155 (1964)

34. D.F.Calef and P.G.Wolynes, JPhys.Chem.87, 3387 (1983); J.Chem.Phys. 78,470 (1983).

35. G.van der Zwan and J.T.Hynes, J.Phys.Chem. 89, 4181 (1985).

36. S. Kato, R.L.Jaffe, A.Komornicki, and K.Morokuma, J.Chem.Phys. 78, 4567 (1983).

37. J.N.Onuchic, J.Chem.Phys. 86, 3929 (1987).

Part II

Photodissociation Dynamics

Chapter 1

General Introduction

1-1. Survey on the Experimental and Previous Theoretical Studies of the Photodissociation Dynamics of CH_3I

Photodissociation of polyatomic molecules through the absorption of UV photons is one of the most fundamental gas phase chemical reactions. A photodissociation process consists of three parts: the absorption of UV photons, dissociation process on potential energy surfaces (PESs), and distributions into final product states. Many experimental techniques have been applied to the photodissociation of polyatomic molecules. Especially, I-containing compounds such as alkyl iodide have been extensively studied since Kasper and Pimentel pointed out that these compounds can become phtodissociation laser due to the high quantum yield of $I^*(^2P_{1/2})$ product (1). At an early stage of this study, several kind of compounds were photolyzed to examine the substituent effect on the I/I^*-branching ratio (1-4). It was found that the branching ratios of alkyl iodides and fluorinated alkyl iodides are similar to that of CH_3I.

The main interest of the photodissociation of I-containing molecules has been directed to obtain more detailed information on the photodissociation process including non-adiabatic transition. Since in general bulky alkyl iodide does not give clear data and it is hard to interpret them without ambiguity, CH_3I, which is the simplest molecule in a series of alkyl iodide, was chosen to examine the photodissociation process in many cases. Rowe and Gedanken assigned the main transition at A-band region to the $^3Q_{0^+} \leftarrow {}^1A_1$ transition by the magnetic circular dichromism experiment (5). This assignment was confirmed by some different kind of experiments such as photoacoustic

measurement(6), time-of-flight experiments (7-8). Van Veen et al pointed out that dissociation proceeds along the top axis of CH_3 (8).

The time-of-flight experiment, which allowed I- and I^*-channel product to be distinguished, and the IR-spectroscopic techniques gave the vibrational distribution of the final product, the quantum yield and their dependence of excitation wavelength (9-12). In these experiments, it was found that the quantum yield of I^*-product is 0.7 ~ 0.8 and that the distribution of umbrella mode of the product CH_3 for I- and I^*-channel shows an inverse population with an maximum peak at v_2=2.

Shapiro and Bersohn have theoretically examined the photodissociation dynamics of CH_3I, using an empirical potential energy surface which reproduces the experimental findings described above. They have treated CH_3I system as a pseudo-linear triatomic system and carried out the quantum dynamics to examine excitation wavenumber dependence of the vibrational distribution and the intensity distributions of the Raman lines (13-16).

From these experimental and theoretical approaches, the following description about the dynamics had been widely accepted until very recently. CH_3I molecule through the absorption of UV photons is excited to a triplet state ($^3Q_0+$) and CH_3I moves on $^3Q_0+$ surface and finally the system goes through to CH_3 + I^* while 20 ~ 30 % of CH_3I goes to CH_3 + I due to the curve crossing between $^3Q_0+$ and a singlet state ($^1Q_1$). The products CH_3 for both I- and I^*-channels have an inverted population of umbrella vibrational mode. This was rationalized by the large change of geometry of the CH_3 portion between initial C_{3v} and final D_{3h}

structure.

However, the recent experimental findings about the photodissociation of CH_3I are different from the above descriptions. Although the detailed reviews will be given in next chapter, the recent experimental findings can be summarized as follows.

(i) The CH_3 product in the I-channel is rotating around the axis perpendicular to the CH_3 top axis (17-20). The CH_3 product in the I^*-channel has much less rotational excitation than in the I-channel (17,19,20). This dynamics, therefore, can no longer be treated with a pseudo-linear triatomic model as it used to be.

(ii) The vibrational distribution of the CH_3 product's ν_2 umbrella mode in the I-channel has an inverse population, with a maximum around $v_2 = 2$ (17,20-22), in qualitative agreement with earlier studies. On the other hand, the product in the I^*-channel has primarily $v_2 = 0$ (17,20-25). Therefore, the previous interpretation about the umbrella mode excitation is inadequate.

(iii) There is some excitation of the ν_1 symmetric stretching mode in the CH_3 product (17,19,20,26,27), though the possibility of ν_1 mode excitation was excluded due to the fact that the frequency of the ν_1 mode of CH_3 radical is much higher than that of the ν_2 mode.

(iv) Recent sophisticated emission spectroscopy made it possible to examine the dissociation process more directly. The CH_3 umbrella motion takes place after the C-I bond is extended to some extent (27). The polarization of the emission changes from parallel to perpendicular in the curve crossing region (28).

The discussion based on ab initio PESs against these new

experiments was desirable because ab initio PESs are developed irrespective of experimental findings, and therefore if we encountered another type of experiment in future, we could discuss the dynamics using ab initio PESs. Furthermore, since the photodissociation dynamics of CH_3I can no longer be treated as a pseudo-linear dynamics as mentioned above, the degree of freedom of PES must be more than 3 dimensions and therefore it is difficult to determine the couplings among the internal degrees of freedom empirically. So it is very natural that one wishes to reexamine the dynamics of CH_3I using ab initio PES instead of empirical PES. The author will theoretically examine the photodissociation dynamics of CH_3I by deriving ab initio PES and performing the classical trajectory calculations using ab initio PES.

1-2. Theoretical Treatments of Nonadiabatic Electronic Transition

The nonadiabatic transition between the PES's plays a critical role in describing the photodissociation dynamics of CH_3I Since the dissociation process involves the PES's of different spin multiplicities, the calculation of spin-orbit coupling elements was required. The author will describe the methods of calculations of spin-orbit coupling elements and the semiclassical surface hopping trajectories which are key theoretical methods before proceeding the next chapter.

1-2-1. Spin-orbit Interaction

Spin-orbit interaction is a significant factor in calculat-

ing accurate wave functions for systems containing heavy elements. Pitzer has calculated several low-lying excited states as well as the ground states for Tl_2, Au_2, TlH, Sn_2, Pb_2 and found that bond lengths, bond strengths and the shape of potential energy curves drastically change when spin-orbit couplings are taken into account (29).

The spin-orbit operator in the Breit-Pauli approximation is given by

$$H^{SO} = \alpha^2/2 \left[\sum_{i,K} Z_K/r_{Ki}^3 \, (r_{Ki} \times p_i)\cdot s_i + \sum_{i,j} 1/r_{ij}^3 (r_{ij} \times p_i)\cdot(s_i + 2s_j) \right] \qquad (1)$$

where α is the fine structure constant, i and j index, the electrons, and K indexes the nuclei. The first term in eq.1 is the one-electron spin-orbit interaction and the second term is the two electron spin-orbit interaction. Walker and Richards have noted that two-center contributions to the matrix element of H^{SO} are small owing to cancellation between the two-center one- and two- electron terms (30). Langhoff has compared the following method (31,32) with all-electron calculations using the full spin-orbit Hamiltonian for the rare-gas oxide potential curves and found very good agreement (33). Therefore, an effective one-center and one-electron spin-orbit hamiltonian

$$H^{SO} = \alpha^2/2 \sum_{A,i} Z_A^{eff}/r_{Ai}^3 \, (r_{Ai} \times p_i)\cdot S_i \qquad (2)$$

has been often used to evaluate the CI matrix elements. Here Z_A in eq.1 is replaced by Z_A^{eff} in eq.2, which is adjusted to match

experimental data. In this research described in the next chapter, Z_A^{eff} is chosen to reproduce the experimental spin-orbit multiplet separation of the iodine atom, $E(I,^2P_{1/2}) - E(I,^2P_{3/2}) = 7603\ cm^{-1}$ at the same level of calculation.

1-2-2. Non-adiabatic Transition

Since the behavior of electronically excited molecule is often associated with the nuclear motion on two or more than potential energy surfaces, the treatment of non-adiabatic transition is also important problem in a classical trajectory calculation. Tully and Preston have developed the surface hopping trajectory method (34). In this method, it is necessary to specify N-dimensional (N: internal degrees of freedom) potential surfaces and the off-diagonal interaction between the surfaces. It is also necessary to define the crossing seam S(R) which is an (N-1)-dimensional avoided crossing hypersurface. A trajectory is started on one surface with the initial conditions and integration is continued until the condition S(R)=0 is satisfied. At this point, the trajectory is branched. The probability $P_i(R,\dot{R})$ of the trajectory undergoing a transition to surface i in obtained by numerical integration of the coupled equations;

$$P_i(R,\dot{R}) = |a_i|^2 \tag{3}$$

$$ih/2\pi\ \dot{a}_i = \sum_{j\neq i} a_j (W_{ij} - ih/2\pi \int \Phi_i (\partial \Phi_j / \partial \tau)\ dr) \tag{4}$$

$$*\exp(-2\pi i/h \int_0^t (W_{jj} - W_{ii})dt)$$

which is derived from substitution of the expansion of eq.5 into eq.7

$$H_{el}(R,r)\Phi(r,t) = ih/2\pi \quad \partial\Phi/\partial t \tag{5}$$

$$\Phi = \sum_j a_j(t)\Phi_j(R,r)\exp(-2\pi i/h\int W_{jj}dt) \tag{6}$$

$$W_{ij} = \int \Phi_i H_{el}\Phi_j d\tau \tag{7}$$

The calculation then proceeds by the integration of each of the trajectories on the interaction surface. If any of them reach the interaction region again, the surface hopping procedure is repeated. In the final averaging process to calculate cross-sections or detailed rate constants each of the branched trajectories is weighted by the appropriate $P_i(R,\dot{R})$ factor.

However, this procedure will rapidly become burdensome if seams are encountered repeatedly in a trajectory. In stead of this method (ants method), Tully and Preston have suggested that only one trajectory be integrated (ant-eater method). At each seam, this one trajectory either undergoes a transition or remains on its present surface as determined by a Monte Carlo game. That is, if probability $P > \xi$ at a seam, a transition occurs but not otherwise. In the limit of an infinite number of trajectories, the two procedures become identical.

Tully and Preston also found that the transition probability were given satisfactorily by the Landau-Zener-Stueckelberg ap-

proximation instead of eq.3.

If adiabatic potential surfaces are used, there is an additional complication arising from the fact that the avoided crossing the surfaces are not degenerate. This is taken into account by adjusting the velocity along the non-adiabatic coupling vector to conserve the total energy.

The appropriateness of using any classical trajectory surface hopping method to the non-adiabatic processes is dependent on the assumption that non-adiabatic transition takes plaoce at localized region and is well separated in time along a trajectory (34,35). It was subsequently improved by Stine and Muckermann, who reduced the multi-dimensional intersection (36-41). However, their formulation is restricted to a particular type of transition region (trough-like intersections).

In order to extend more general cases, Parlant and Alexander have very recently developed a new modification of the trajectory surface hopping technique that allows for trajectory hops at any location, not only at avoided intersections (42,43). In their method, the semiclassical probability for being on each adiabatic surface is calculated by integrating the electronic coupled equations. For simplicity, consider a system with two electronic states Ψ_1 and Ψ_2, which are eigenfunctions of the electronic Hamiltonian with eigenvalues W_1 and W_2. As the trajectory evolves in time, the electronic states obey

$$\dot{a}_1 = a_2 \, \Omega \, \exp(-2\pi i S/h) \qquad (8)$$

$$\dot{a}_2 = -a_1 \, \Omega \, \exp(-2\pi i S/h) \qquad (9)$$

$$S = \int^{t} W(t')dt' \qquad (10)$$

$$\Omega = \dot{r} \cdot \langle \Psi_2 | \nabla | \Psi_1 \rangle \qquad (11)$$

Here $W = W_2 - W_1$, $\dot{r}$ is the nuclear velocity vector and $\langle \Psi_2 | \nabla | \Psi_1 \rangle$ is the non-adiabatic coupling vector. $|a_i(t)|^2$ (i=1,2) represents the probability that the system is in electronic state i at time t. Initially a_1=1, a_2=0, Ω=0. As the trajectory evolves in time, $|\Omega|$ and $|a_2|^2$ grow, and at same point, the trajectory is allowed to branch to surface 2. Eqs.8 and 9 are integrated through the entire transition region to obtain the hopping probability P and the coefficients are reinitialized only at the points where $|\Omega|$ is minimum. The transition region is defined here as the region where $|\Omega|$ rises from a minimum, goes through a maximum, and falls to a second minimum. They found it to give excellent agreement with quantum calculations for He + CN reaction.

References.

1. J.V.V.Kasper and G.C.Pimentel, Appl.Phys.Lett. 5 231 (1964).

2. J.V.V.Kasper, J.H.Parker and J.C.Pimentel, J.Chem.Phys. 43 1827 (1965).

3. M.A.Pollack, Appl.Phys.Lett. 8 36 (1966).

4. S.J.Riely and K.R.Wilson, Faraday Disc.Chem.Soc. 53 132 (1972).

5. A.Gedanken and M.D.Rowe, Chem.Phys.Lett. 34 39 (1975).

6. T.F.Hunter and K.S.Kristjansson, Chem.Phys.Lett. 58 291 (1978).

7. M.D.Barry and P.A.Gorry, Mol.Phys. 52 461 (1984).

8. G.N.A.van Veen, T.Baller, A.E.de Vries and N.J.A. van Veen Chem.Phys. 87 405 (1984).

9. R.K.Sparks, K.Shobatake, L.R,Carlson and Y.T.Lee, J.Chem.Phys. 75 3838 (1981).

10. S.L.Baughcum and S.R.Leone, J.Chem.Phys. 72 6531 (1980).

11. H.W.Hermann and S.R.Leone, J.Chem.Phys. 76 4766 (1982).

12. W.P.Hess, S.J.Kohler,H.K.Haugen and S.R.Leone, J.Chem.Phys. 84 2143 (1986).

13. M.Shapiro and R.Bersohn, J.Chem.Phys. 72 3810 (1980).

14. M.Shapiro and R.Bersohn, Ann. Rev.Phys.Chem. 33 409 (1982).

15. S.Kanfer and M.Shapiro, J.Phys.Chem. 88 3964 (1984).
16. M.Shapiro, J.Phys.Chem. 90 3644 (1986).

17. R.O.Loo, H.P.Haerri, G.E. Hall and P.L.Houston, J.Chem. Phys. 90 4222 (1989).

18. J.F.Black and I.Powis, J.Chem.Phys. 89 3986 (1988).

19. I.Powis and J.F.Black, J.Phys.Chem. 93 2461 (1989).

20. D.W.Chandler, J.W.Thoman Jr., M.H.M Jassen and D.H.Parker, Chem.Phys.Lett. 156 151 (1989).

21. R.O.Loo, G.E.Hall,H.P.Haerri and P.L.Houston, J.Phys.Chem. 92 5 (1988).

22. J.F.Black and I.Powis, Chem.Phys. 125 375 (1988).

23. D.W.Chandler and P.L.Houston, J.Chem.Phys. 87 1445 (1987).

24. a) H.Kanamori and E.Hirota, private communication.
b) T.Suzuki, H.Kanamori and E.Hirota, private communication.

25. G.E.Hall, T.J.Sears and J.M.Frye,
J.Chem.Phys. 90 6234 (1989).

26. D.Imre, J.L.Kinsey, A.Asinha and J.Krenos,
J.Phys.Chem. 88 3956 (1984).

27. M.O.Hale, G.E.Galcica, S.G.Glogover and J.L.Kinsey,
J.Phys.Chem. 90 4997 (1986).

28. K.Q.Lao, M.D.Person, P.Xayariboun and L.J.Butler,
J.Chem.Phys. 92 823 (1990).

29. a) K.S.Pitzer, Int.J.Quantum Chem. 25 13 (1984).
b) K.S.Pitzer, Acc.Chem.Res. 12 271 (1979).

30. T.E.H.Walker and W.G.Richards, J.Chem.Phys. 52 1311 (1970).

31. J.S.Cohen, W.R.Wadt and P.J.Hay,
J.Chem.Phys. 71 2955 (1979).

32. P.J.Hay, W.R.Wadt, L.R.Kahn, R.C.Raffenetti and D.H.Phillips,
J.Chem.Phys. 71 1767 (1979).

33. S.R.Langhoff, J.Chem.Phys. 73 2379 (1980).

34. J.C.Tully and R.K.Preston, J.Chem.Phys. 55 562 (1971).

35. W.H.Miller and T.F.George, J.Chem.Phys. 56 5637 (1972).

36. C.A.Mead and D.G.Truhlar, J.Chem.Phys. 84 1055 (1986).

37. J.R.Stine and J.T.Muckeman, J.Chem.Phys. 65 3975 (1976).

38. J.R.Stine and J.T.Muckeman, J.Chem.Phys. 68 1085 (1978).

39. J.R.Stine and J.T.Muckeman, J.Chem.Phys. 84 1056 (1986).

40. N.C.Blais and D.G.Truhler, J.Chem.Phys. 79 1334 (1983).

41. B.J.Kuntz, J.K.Kedrick and W.N.Whitton,
Chem.Phys. 38 147 (1979).

42. G.Parlant and E.A.Gislason, J.Chem.Phys. 91 4416 (1989).

43. G.Parlant and M.H.Alexander, J.Chem.Phys. 92 2287 (1990).

Chapter 2

Ab Initio Potential Energy Surfaces and Trajectory Studies of $CH_3I^* \rightarrow CH_3 + I$ and $CH_3 + I^*$

2-1. Introduction

The A(n –> σ*) band photodissociation of CH_3I had been extensively studied experimentally (1-14) and theoretically (15-22), with a major focus on the ν_2 umbrella mode excitation of the CH_3 product. In this reaction (see Fig.1), the photon is

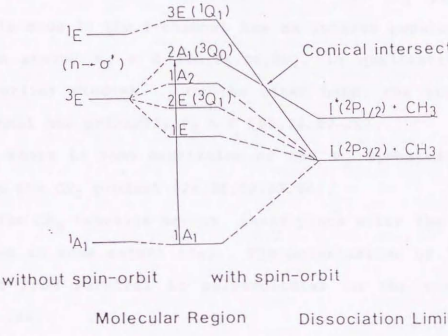

Fig.1 Correlation diagram of the potential energy surfaces for C_{3v} dissociation without and with spin-orbit.

considered to take the CH_3I system to the $^3Q_0$ state, which crosses with the $^1Q_1$ state during the dissociation. The former state gives the products : CH_3 + $I^*(^2P_{1/2})$, and the latter state, CH_3 + I ($^2P_{3/2}$). However, in the last few years, several new experimental reports have appeared giving new insights in the detail of the dynamics. The recent experimental findings can be summarized as follows.

(i) The CH_3 product in the I-channel is rotating around the axis perpendicular to the CH_3 top axis (24,27,28,30). The CH_3 product in the I^*-channel has much less rotational excitation than in the I-channel (24,28,30). This dynamics, therefore, can no longer be treated with a pseudo-linear triatomic model as it used to be.

(ii) The vibrational distribution of the CH_3 product's ν_2 umbrella mode in the I-channel has an inverse population, with a maximum around $v_2 = 2$ (23,24,26,30), in qualitative agreement with earlier studies. On the other hand, the product in the I^*-channel has primarily $v_2 = 0$ (23,24,29-32).

(iii) There is some excitation of the ν_1 symmetric stretching mode in the CH_3 product (24,28,30,33,34).

(iv) The CH_3 umbrella motion takes place after the C-I bond is extended to some extent (34). The polarization of the emission changes from parallel to perpendicular in the curve crossing region (35).

However, individual results are different in detail from each other and we make a belief review on some important experimental reports. Powis and Black (PB) (28) have found in the photodissociation of CD_3I (as well as CH_3I (27)) that the CD_3 product in the I-channel has relatively large population at N = 8 and has high rotational excitation up to N=14 and that the product in the I^*-channel has less excitation, with up to 4 angular momentum units. They have also found that the I^*-channel product has a trend with $K \approx N$ and that I-channel product has $K \perp N$. Houston et al. have estimated the average CH_3 rotational excitation to be 125 cm^{-1} (24), which is lower than the PB esti-

mation, 208cm^{-1} for CH_3 (27). They have examined this difference and pointed out that PB results might be affected by the initial rotation of the parent CH_3I molecule. Chandler and coworkers have obtained results similar to Houston's; the rotational excitation extends only up to N=6, and the average rotational energies around the axis perpendicular and parallel to the top axis are 106 and 8 cm^{-1}, respectively (30).

PB have shown that the I-channel has an inverted CH_3 ν_2 vibrational population with its peak at v_2=3, and that the I^*-channel has a peak at v_2=2 with the population ratio for v_2=0,1,2 of 1 : 1.1 : 2.0 (26), which is very different from previous results, 1 : 4.4 : 14.6, of Lee et al. (8). Houston et al. have estimated the population ratio $(v_2=0)/(v_2=2)$ for CD_3 to be about 1.1 (24). They have found that the I^*-channel product has primarily v_2=0. Chandler et al. have shown that the I/I^* ratio increases with the increasing vibrational quantum number (30). Kanamori et al. have observed that the distribution in the ν_2 mode in the I^*-channel monotonically decreases with the quantum number with the population ratio of 0.66 : 0.26 : 0.08 : 0.004 for v_2 = 0,1,2,3 (31). Hall et. al. have found that the population ratio of the I^*-channel product is 4 : 3 : 2 for v_2 = 0, 1, 2 (32).

The excitation in the ν_1 CH_3 symmetric stretching mode was in earlier days considered unlikely because the C-H bond distances of the parent CH_3I and the product CH_3 are almost identical and that the ν_1 mode has a much higher frequency than the ν_2 mode. PB have found that the ν_1 excitation occurs only in the CD_3 produced via the I-channel, that is, the ν_1 excitation has an isotope and channel specificity (28). Houston et al. have

found the ν_1 mode excitation for CH_3 spieces (24), but they did not examine the channel specificity. Chandler et al. have observed that the I/I^* ratio of v_1=1 is >2.0, indicating that the I-channel is more easily excited (30). Kinsey and co-workers have observed the ν_1 mode excitation (v_1 =1) by means of Raman emission spectroscopy (33,34).

Recent emission spectroscopy studies have made it possible to probe an evolution of the molecular dissociation on potential energy surfaces. Kinsey and co-workers have concluded that in the photodissociation of CH_3I, the C-I bond extension initially takes place to some extent before the subsequent umbrella motion sets in (34). Lao et al. have observed that the polarization of the emission with lower quantum number in C-I stretch is parallel, but the polarization of the emission with the higher quantum number is perpendicular. From their observation, they have given a classical picture to the photodissociation through an electronic curve crossing, that is, the amplitude of the molecular wave function gradually develops on the $^1Q_1$ repulsive surface as the molecule dissociates through a curve crossing (35).

On the theoretical side, Shapiro and Bersohn have treated the photodissociation dynamics of CH_3I as a linear triatomic system using empirical potential surfaces (denoted hereafter the SB surfaces) of the $^3Q_0$ and $^1Q_1$ states and adjusted their parameters to explain the dynamics such as the ν_2 vibrational distribution of the CH_3 product, the branching ratio and its wavelength dependence (15-17). The SB empirical surfaces have also been used for other dynamics studies (18,19). However, the SB

surfaces, with only two degrees of freedom, the C-I stretch and the CH_3 umbrella motion, can not handle the new experimental findings of CH_3 rotational excitation. Even for the CH_3 umbrella mode distribution, the SB surfaces give results (ν_2 hot in both channels) which agree with the old experiments (7-12) but disagree with new experimental findings mentioned above (24,26,30-32) (ν_2 hot in the I-channel but cold in the I^*-channel). Very recently Guo and Schatz have modified the SB surfaces (denoted hereafter the GS surfaces) to reproduce the new experimental findings (36).

We have recently calculated and reported preliminarily the general feature of the potential energy surfaces (PESs) of the two excited states for non-C_{3v} geometries of CH_3I, and have indicated that the bending near the $3E$-$2A_1$ conical intersection can be the origin of the CH_3 rotational excitation (37).

The present study is an extended and thorough account of the study. We have calculated the potential energy surfaces of the excited states with an ab initio SOCI method and fitted them to analytical functions for six degrees of freedom, (the C-I stretch, the CH_3 umbrella motion, the CH_3 deformation, the CH_3 rock), i.e. all the degrees of freedom except for 3 C-H stretches. We have also performed classical trajectory calculations on these analytical potential functions. In section 2-2, we describe the method of calculation for obtaining the adiabatic energies, transformation from the adiabatic to the diabatic basis and analytical fitting of diabatic energies. In section 2-3, we describe the method of classical trajectory calculation including the treatment of non-adiabatic transition based on a Landau-Zener

model. In section 2-4, we describe the global features of PESs, the results of classical trajectory calculations and discussions on the origin of vibrational and rotational excitation. We also discuss the relationship between PES characteristics and dynamics and how the initial conditions affect the dynamics. Finally, we give our conclusions in section 2-5.

2-1. Methods of Calculation of PESs

2-1-1. Adiabatic Energies

Ab initio spin-orbit configuration interaction (SOCI) calculations have been performed to obtain the potential energy surfaces. We have used a double-zeta-plus-polarization (DZP) basis set: the Huzinaga-Dunning double-zeta basis set for carbon and hydrogen atoms (38), and the Hay-Wadt relativistic effective core potential (39) and associated valence double-zeta basis functions augmented with a single d-polarization function on carbon (α_d=0.75) and iodine (α_d=0.405). The molecular orbitals have been determined by an open shell RHF calculation for the averaged $n \rightarrow \sigma^*$ excited states. SOCI calculations have been carried out with a modified COLUMBUS package (40), using a one-electron spin-orbit hamiltonian with an empirical nuclear charge (37). In our previous calculations, we have used the uncontracted SOCI with about $5*10^5$ configuration state functions for each of A' and A" symmetry, arising from the single and double excitations out of the full valence $(\sigma, \sigma^*, e_x, e_y)^6$ reference configurations (16 in A' and 12 in A"). In order to perform calculations at many points to obtain the analytical potential functions, we have used in the present paper a 'contracted' SOCI method, which is similar to the method by Cohen et al. (41). First, a large-scale spin-free CI calculation is performed to obtain the spin-free eigenstates and eigenvalues and then a small contracted SOCI matrix (12 dimension in the C_1 double group symmetry, 6 (A') and 6 (A") dimension in C_s double group symmetry), which is composed of the diagonal matrix elements of the spin-free eigenstates obtained above and the off-diagonal matrix elements of spin-orbit

interaction, is diagonalized and the adiabatic energies for each geometry are obtained. All the independent spin functions belonging to the lowest $^1A_1$, ^3E, ^1E and $^3A_1$ states of the spin free CI are included in the contracted SOCI; the six A' independent functions included in the contracted SOCI are one $^1A_1$, three ^3E's, one ^1E and one $^3A_1$, and the six A" functions are three ^3E's, one ^1E and two $^3A_1$'s. The inclusion of the high-lying $^3A_1$ states is essential to obtaining a reasonable results in the contracted SOCI calculation. In Table I, we show an example of

Table I. Comparison of Excitation Energies (in eV) [a]

State	Contracted SOCI	Uncontracted SOCI
$^1A_1$ ($1A_1$)	0.0 [b]	0.0 [b]
$^3Q_2$ (1E)	4.455	4.457
$^3Q_1$ (2E)	4.629	4.629
$^3Q_{0-}$ ($1A_2$)	4.984	4.991
$^3Q_{0+}$ ($2A_1$)	5.089	5.067
$^1Q_1$ (3E)	5.450	5.448

a) At the experimental equilibrium geometry : R(C-I) = 2.132 Å, R(C-H) =1.084 Å and <HCH =111.2° with the C_{3v} symmetry (42).

b) The total energy of the ground state is -51.008888 and -51.009699 hartree for contracted and uncontracted SOCI, respectively.

comparison of adiabatic energies between contracted and uncontracted SOCI calculations. The contracted SOCI results reproduce the uncontracted ones very well. The excitation energies of CH_3I at the experimental equilibrium geometry from the ground to the n -> σ^* excited states $^3Q_1$, $^3Q_{0-}$, $^3Q_{0+}$ (we refer this state simply an $^3Q_0$ throughout the paper) and $^1Q_1$ are 4.63, 4.98, 5.09 and 5.45 eV, respectively, in reasonable agreement with the experimental broad A-band centered around 260 nm (4.77eV). The adiabatic energies at 170 points have been calculated, varying the C-I distance R, the umbrella angle α, the bending angle θ, the direction of the bend ϕ, and the projections of the three HCH angles to the plane perpendicular to the top axis β_i (i=1,2,3), as defined in Fig.2. The C-H bonds are fixed throughout the paper at r_e = 1.084 Å (42).

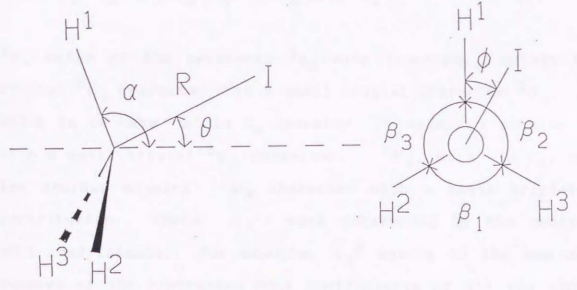

Fig.2 Definition of internal coordinates.
The broken line on the left is the axis for which the the umbrella angle is equal for all three CH's.
The figure on the right is projection to the plane perpendicular to this axis.
θ takes a value between 0 and π. ϕ is between 0 and 2π.
β_i's are redundant, satisfying $\beta_1 + \beta_2 + \beta_3 = 2\pi$.

2-2-2. Transformation from Adiabatic to Diabatic Basis

In running a classical trajectory, we have to evaluate the adiabatic $^3Q_0$ and $^1Q_1$ potential energies and forces using analytical potential functions. However, it is hard to fit the adiabatic $^3Q_0$ and $^1Q_1$ energies to analytical functions because the character of each state changes with the geometry. Therefore, we transformed the adiabatic states to the diabatic states and fitted the latter to analytical functions. The transformation was carried out in the following way. Three adiabatic wave functions for each geometry can be written as in eqs. 1 to 3.

$$^3\Psi = N_1(^3\psi_1+\lambda_1{}^1\psi_1) \qquad N_1=1/(1+\lambda_1{}^2)^{\frac{1}{2}} \qquad (1)$$

$$^1\Psi_1= N_2(^1\psi_2+\lambda_2{}^3\psi_2) \qquad N_2=1/(1+\lambda_2{}^2)^{\frac{1}{2}} \qquad (2)$$

$$^1\Psi_2= N_3(^1\psi_3+\lambda_3{}^3\psi_3) \qquad N_3=1/(1+\lambda_3{}^2)^{\frac{1}{2}} \qquad (3)$$

$^3\Psi$, which is the adiabatic $^3Q_0$ wave function, mainly has a triplet $^3\psi_1$ character with a small singlet character $^1\psi_1$. $^1\Psi_1$, which is to have A' in C_s symmetry, is mainly a singlet $^1\psi_2$ with a small triplet $^3\psi_2$ character. $^1\Psi_2$, of A" in C_s, mainly has another singlet $^1\psi_3$ character with a small triplet $^3\psi_3$ contribution. Three λ_i's were determined by the contracted SOCI coefficients. For example, $\lambda_1{}^2$ equals to the sum of the squares of the contracted SOCI coefficients of all the singlets (3 singlets in C_1, 2 for A' in C_s, and 1 for A" in C_s in the SOCI). We transform these adiabatic wave functions (eqs. 1 to 3), using the matrix U defined in eq. 4 into another set of wave functions in eq. 5.

$$U = \begin{bmatrix} 1 & 0 & 0 \\ 0 & \cos A & \sin A \\ 0 & -\sin A & \cos A \end{bmatrix} \begin{bmatrix} \cos B & \sin B & 0 \\ -\sin B & \cos B & 0 \\ 0 & 0 & 1 \end{bmatrix} \begin{bmatrix} \cos C & 0 & \sin C \\ 0 & 1 & 0 \\ -\sin C & 0 & \cos C \end{bmatrix} \quad (4)$$

$$\begin{bmatrix} {}^3\Phi_1 \\ {}^1\Phi_2 \\ {}^1\Phi_3 \end{bmatrix} = \begin{bmatrix} a_{11} & a_{12} & a_{13} \\ a_{21} & a_{22} & a_{23} \\ a_{31} & a_{32} & a_{33} \end{bmatrix} \begin{bmatrix} {}^3\Psi \\ {}^1\Psi_1 \\ {}^1\Psi_2 \end{bmatrix} = U \begin{bmatrix} {}^3\Psi \\ {}^1\Psi_1 \\ {}^1\Psi_2 \end{bmatrix} \quad (5)$$

$$\begin{aligned} {}^3\Phi_1 = {} & (a_{11}N_1{}^3\psi_1 + a_{12}\lambda_2N_2{}^3\psi_2 + a_{13}\lambda_3N_3{}^3\psi_3) \quad (6) \\ & + (a_{11}\lambda_1N_1{}^1\psi_1 + a_{12}N_2{}^1\psi_2 + a_{13}N_3{}^1\psi_3) \\ {}^1\Phi_2 = {} & (a_{21}\lambda_1N_1{}^1\psi_1 + a_{22}N_2{}^1\psi_2 + a_{23}N_3{}^1\psi_3) \quad (7) \\ & + (a_{21}N_1{}^3\psi_1 + a_{22}\lambda_2N_2{}^3\psi_2 + a_{23}\lambda_3N_3{}^3\psi_3) \\ {}^1\Phi_3 = {} & (a_{31}\lambda_1N_1{}^1\psi_1 + a_{32}N_2{}^1\psi_2 + a_{33}N_3{}^1\psi_3) \quad (8) \\ & + (a_{31}N_1{}^3\psi_1 + a_{32}\lambda_2N_2{}^3\psi_2 + a_{33}\lambda_3N_3{}^3\psi_3) \end{aligned}$$

The angle A, for instance, in eq.4 determines the transformation between the two adiabatic ${}^1Q_1$ states, ${}^1\Psi_1$ and ${}^1\Psi_2$. The following function f(A,B,C) gives the sum of weights of minor spin components over the three states.

$$\begin{aligned} f(A,B,C) = \int [& (a_{11}\lambda_1N_1{}^1\psi_1 + a_{12}N_2{}^1\psi_2 + a_{13}N_3{}^1\psi_3)^2 \\ & + (a_{21}N_1{}^3\psi_1 + a_{22}\lambda_2N_2{}^3\psi_2 + a_{23}\lambda_3N_3{}^3\psi_3)^2 \\ & + (a_{31}N_1{}^3\psi_1 + a_{32}\lambda_2N_2{}^3\psi_2 + a_{33}\lambda_3N_3{}^3\psi_3)^2] d\tau \end{aligned}$$

$$
\begin{aligned}
&= a_{11}{}^2N_1{}^2\lambda_1{}^2 + a_{12}{}^2N_2{}^2 + a_{13}{}^2N_3{}^2 + a_{21}{}^2N_1{}^2 + a_{22}{}^2N_2{}^2\lambda_2{}^2 \\
&+ a_{23}{}^2N_3{}^2\lambda_3{}^2 + a_{31}{}^2N_1{}^2 + a_{32}{}^2N_2{}^2\lambda_2{}^2 + a_{33}{}^2N_3{}^2\lambda_3{}^2 \qquad (9) \\
&+ 2(a_{11}a_{12}N_1N_2\lambda_1 {}^1\psi_1|{}^1\psi_2> + a_{11}a_{13}N_1N_3\lambda_1 {}^1\psi_1|{}^1\psi_3> \\
&+ a_{12}a_{13}N_2N_3 {}^1\psi_2|{}^1\psi_3> + a_{21}a_{22}N_1N_2\lambda_2 {}^3\psi_1|{}^3\psi_2> \\
&+ a_{21}a_{23}N_1N_3k_3 {}^3\psi_1|{}^3\psi_3> + a_{22}a_{23}N_2N_3\lambda_2\lambda_3 {}^3\psi_2|{}^3\psi_3> \\
&+ a_{31}a_{32}N_1N_2\lambda_2 {}^3\psi_1|{}^3\psi_2> + a_{31}a_{33}N_1N_3\lambda_3 {}^3\psi_1|{}^3\psi_3> \\
&+ a_{32}a_{33}N_2N_3\lambda_2\lambda_3 {}^3\psi_2|{}^3\psi_3>)
\end{aligned}
$$

Though we cannot eliminate the minor spin components completely, i.e. f(A,B,C) = 0, we can minimize it as far as possible by choosing A, B and C to satisfy eq.10.

$$\partial f/\partial A = \partial f/\partial B = \partial f/\partial C = 0 \qquad (10)$$

Using U thus determined, we transform with eq.11 three adiabatic energies, $E(^1Q_1 1)$, $E(^1Q_1 2)$ and $E(^3Q_0)$ to six diabatic matrix elements at each geometry.

$$\begin{bmatrix} V_3 & V_{13} & V_{23} \\ V_{13} & V_1 & V_{12} \\ V_{23} & V_{12} & V_2 \end{bmatrix} = U \begin{bmatrix} E(^3Q_0) & 0 & 0 \\ 0 & E(^1Q_1 1) & 0 \\ 0 & 0 & E(^1Q_1 2) \end{bmatrix} U^{-1} \qquad (11)$$

where $V_{ij} = \int \Phi_i{}^* H \Phi_j \, d\tau$ and $V_i = V_{ii}$

We note that the order of the operations in eq.4 is arbitrary. Though a different order of the operations gives a difference in a set of angles A, B, C, which satisfies the eq. 10, it does not change the transformation matrix U in eq.4, and therefore, six diabatic matrix elements on the left hand side of eq. 11 are independent of the order of the operations.

2-2-3. Analytical Fitting of Diabatic Potential Terms

We have fitted the six diabatic matrix elements to analytical functions with respect to seven internal coordinates. The C_{3v} geometries are determined only by R and α, with all the other parameters to be zero. Changes of the other parameters from zero lower the symmetry from C_{3v} to C_s or C_1. First, we describe the three diagonal terms. In the present system, there is an energetic and symmetry hierarchy with respect to the internal coordinates. The diagonal terms change within 0.1 hartree with respect to R, within 0.01 hartree with respect to α, and within 0.001 hartree with respect to the other parameters, θ, ϕ and β_i(i=1,2,3) in the region probed in the dynamics. We have also found that the diabatic terms obey a good additivity rule among the θ, ϕ and β_i's contributions. Furthermore we have to consider the requirement that the adiabatic $^3Q_0$ and $^1Q_1$ energies are unchanged by permutation among the three hydrogens, which relates the internal parameters, ϕ and β_i's. A detailed discussion on this requirement is given in Appendix. This requirement leads us to two restrictions about the fitting forms of

the diabatic potential functions ; there should be a coupling between ϕ and β_i's and there should be some relationships among the fitting forms of six diagonal and off-diagonal terms. Based on the above discussion, we first fitted the diagonal elements at the C_{3v} geometries to analytical functions of R and α. Then, we fitted the differences between the C_{3v} and the non-C_{3v} values ; this procedure ensures that the relatively small energy dependence in the θ, ϕ and β_i's, is properly reproduced in the fitted functions. In the non-C_{3v} fitting, the θ, ϕ and β_i's contributions have been fitted independently in view of the additivity mentioned above. The actual forms of fitting functions are given below for the two diabatic singlets (eqs.12 and 13, corresponding to the A' and the A" state in the C_s symmetry, respectively) and for the diabatic triplet state (eq.14).

$$V_1 = (A_0 + A_1\Delta R)*\exp(-A_5\Delta R) + V_{CH3} + (A_2*\sin^2\theta + A_3*(1+X(\phi,\beta_2,\beta_3,\xi))*\sin\theta)*\exp(-A_5\Delta R) + A_4*S_a*\exp(-A_6\Delta R) \quad (12)$$

$$V_2 = (A_0 + A_1\Delta R)*\exp(-A_5\Delta R) + V_{CH3} + (A_2*\sin^2\theta + A_3*(1-X(\phi,\beta_2,\beta_3,\xi))*\sin\theta)*\exp(-A_5\Delta R) - A_4*S_a*\exp(-A_6\Delta R) \quad (13)$$

$$V_3 = (B_0 + B_1\Delta R)*\exp(-B_3\Delta R) + V_{CH3} + \Delta E_I + B_2*\sin^2\theta*\exp(-B_3\Delta R) \quad (14)$$

The variables used, in addition to θ, are

$\Delta R=R-R_e$, $\Delta\alpha=\alpha-\pi/2$, $\Delta\beta_i=\beta_i-2\pi/3$ (i=1,2,3),

$S_a=1/\sqrt{6}(2\Delta\beta_1-\Delta\beta_2-\Delta\beta_3)$, $S_b=1/\sqrt{2}(\Delta\beta_2-\Delta\beta_3)$,

$X(\phi,\beta_2,\beta_3,\zeta)=[\cos(3\phi+\zeta)+\cos\{3(\phi+\beta_3)+\zeta\}+\cos\{3(\phi-\beta_2)+\zeta\}]/3$,

$\tan\zeta=S_b/S_a$, and

r_e and R_e are the equilibrium C-H and C-I distances.
The coefficients A_0 to A_6, and B_0 to B_3, represented in general by Z_i, are the following functions of $\Delta\alpha$.

$$Z_i = Z_{i0} + Z_{i1}*\sin\Delta\alpha + Z_{i2}*\sin^2\Delta\alpha, \qquad (15)$$

V_{CH3} is the term which reproduces the CH_3 force field in the dissociation limit, and we used Spiko and Bunker's empirical CH_3 force field (43).

$$V_{CH3} = G_2*(r_e*\sin\Delta\alpha)^2 + G_4*(r_e*\sin\Delta\alpha)^4 + G_6*(r_e*\sin\Delta\alpha)^6 + H_2/2*(S_a^2 + S_b^2) \qquad (16)$$

ΔE_I=0.034646 hartree in eq.14 is the energy difference between the ground ($^2P_{3/2}$) and the excited ($^2P_{1/2}$) states of the iodine atom.

The first lines on the right hand side of eqs.12 and 13, which depend only on R and α and are the largest contributions to V_1 and V_2, are the same since they represent the C_{3v} symmetry where V_1 and V_2 are degenerate. The second lines, relating to the direction of bending of the I atom, are different from each other, though they share the common exponential factor A_5 due to the energetic hierarchy and the convenience. The potential curves with respect to $\sin\theta$ all fit well to a parabola. With respect to ϕ, all the diagonal terms have a three fold symmetry, with the energy minimum at ϕ=0° for V_1 and ϕ=180° for V_2 when the CH_3 group has a local C_{3v} symmetry. The second lines represent these angular dependencies. The third lines in eqs.12 and 13, relating to the CH_3 deformation, differ only in sign between eqs.12 and 13. The first term in the third line , which was determined in the C_s symmetry, is linear with respect to $\Delta\beta_i$'s. The coefficients of diagonal terms are listed in Table II.

Table II. Potential Function Parameters : Coefficients of Diagonal Terms [a),b)]

	X_{i0}	X_{i1}	X_{i2}
A_0	0.140181	-0.124719	0.043310
A_1	0.088560	-0.048580	-0.163996
A_2	0.141458	-0.384253	0.339277
A_3	-0.003932	0.002520	-0.000993
A_4	-0.002909	0.005382	-0.006503
A_5	1.99296	-0.127307	-1.41067
A_6	0.810876	2.41001	0.0
B_0	0.099686	-0.153511	0.064085
B_1	-0.068734	0.068596	-0.059619
B_2	0.099668	-0.181578	0.089516
B_3	0.874084	-0.337881	2.610930

CH_3 force field

G_2	0.012319	G_4	0.026889	G_6	-0.000889
H_2	0.096837				

a) In units of a.u.

b) Constants are R_e =4.02889 a.u. and r_e = 2.0484a.u.

Next, we describe the fitting forms of the off-diagonal elements, which are shown in eqs.17, 18 and 19.

$$V_{13} = D_1*X(\phi,\beta_2,\beta_3,\xi)*\sin\theta/((R-D_2)^2+D_3^2) + D_4*S_a/((R-D_5)^2+D_6^2) \quad (17)$$

$$V_{23} = -D_1*Y(\phi,\beta_2,\beta_3,\xi)*\sin\theta/((R-D_2)^2+D_3^2) - D_4*S_b/((R-D_5)^2+D_6^2) \quad (18)$$

$$V_{12} = A_3*Y(\phi,\beta_2,\beta_3,\xi)*\sin\theta*\exp(-A_5\Delta R) + A_4*S_b*\exp(-A_6\Delta R) \quad (19)$$

where

$$Y(\phi,\beta_2,\beta_3,\xi)=[\sin(3\phi+\xi)+\sin\{3(\phi+\beta_3)+\xi\}+\sin\{3(\phi-\beta_2)+\xi\}]/3$$

These off-diagonal elements are all zero within the C_{3v} symmetry. Since the diabatic states $^1\Phi_1$ and $^1\Phi_2$ belong to A' and A" in the C_s symmetry, respectively, V_{23} is 0 in the C_s symmetry, whereas V_{13} is non-zero even in C_s. The singlet-triplet coupling terms, V_{13} and V_{23}, have been found to be reproduced well by Lorentzian functions which have the maximum with respect to R near the conical intersection. The off-diagonal term V_{12} between the two singlet states has been found to fit well to the function relating to the ϕ and β_i's parts of the diagonal term V_1(or V_2), which satisfies the second requirement as pointed out before. The coefficients D_1 to D_6 in eqs. 17 to 18 are also functions of α, as are given in eq.15. The coefficient sets of the off-diagonal terms are listed in Table III.

Table III. Potential Function Parameters : Coefficients of Off-diagonal Terms a)

	X_{i0}	X_{i1}	X_{i2}
D_1	0.004618	-0.011405	0.011226
D_2	4.22343	0.437838	0.0
D_3	0.662089	0.490741	0.0
D_4	-0.000436	0.001009	-0.001683
D_5	4.30019	0.316343	0.0
D_6	0.941249	0.027870	0.0

a) In units of a.u.

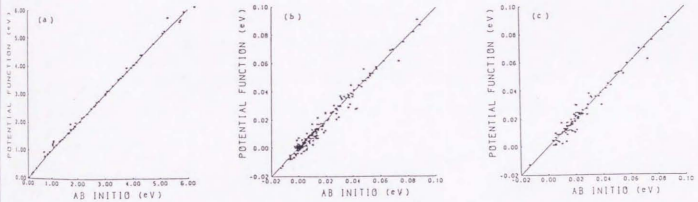

Fig.3 Comparison of the adiabatic energies between ab initio calculations vs. analytical functions fitted.
(a) the energy at the C_{3v} geometry,
(b) the energy difference between the C_{3v} geometry and the non-C_{3v} geometry with respect to θ and ϕ, and
(c) the energy difference between the C_{3v} geometry and the non-C_{3v} geometry with respect to β_i's.

In Fig.3, the adiabatic energies of the ab initio SOCI calculation are compared with those from the fitted analytical potential functions. The standard deviations of the fit were 0.0933, 0.0033, 0.0036 eV for Fig.3(a),(b),(c), respectively. Note the difference in energy scale of (a) from that of (b) and (c). For each hierarchy of variables, the ab initio energies are well reproduced by the analytical functions. We use thus obtained analytical potential energy functions without modification in classical surface hopping trajectory calculation.

2-3. Classical Trajectory Calculations

2-3-1. Initial Conditions

Since parent molecules CH_3I in most relevant experiments are cooled in supersonic expansion, they are considered to be at the vibrational ground state. The rotation of the entire molecule or its coupling with vibration has not been considered. Therefore, the normal mode description can be used for initial conditions of classical trajectory calculations (44). First, nine normal mode coordinates of CH_3I were determined according to eqs. 20 and 21.

Table IV. Calculated Vibrational Frequencies (in cm^{-1}) and Their L Matrix

a_1 symmetry	3105.2 (2933)[a]	1346.3 (1252)	562.4 (533)
S_1	-0.997451	-0.002227	-0.016053
S_2	-0.051969	-0.982293	-0.139558
S_3	0.048904	0.187339	-0.990084
e symmetry	3254.2 (3060)	1541.0 (1436)	891.4 (882)
S_4	-0.997451	-0.002227	-0.016053
S_5	-0.051969	-0.982293	-0.139558
S_6	0.048904	0.187339	-0.990084

Table IV continued

	Definition of Symmetry Coordinates [b]	
a_1	CH_3 s-str.	$S_1 = 1/\sqrt{3}(\Delta r_1 + \Delta r_2 + \Delta r_3)$
	CH_3 s-def.	$S_2 = 1/\sqrt{6}(\Delta\alpha_1 + \Delta\alpha_2 + \Delta\alpha_3 - \Delta\gamma_1 - \Delta\gamma_2 - \Delta\gamma_3)$
	CI str.	$S_3 = \Delta R$
e	CH_3 d-str.	$S_{4a} = 1/\sqrt{6}(2\Delta r_1 - \Delta r_2 - \Delta r_3)$
		$S_{4b} = 1/\sqrt{2}(\Delta r_2 - \Delta r_3)$
	CH_3 d-def.	$S_{5a} = 1/\sqrt{6}(2\Delta\gamma_1 - \Delta\gamma_2 - \Delta\gamma_3)$
		$S_{5b} = 1/\sqrt{2}(\Delta\gamma_2 - \Delta\gamma_3)$
	CH_3 d-rock.	$S_{6a} = 1/\sqrt{6}(2\Delta\alpha_1 - \Delta\alpha_2 - \Delta\alpha_3)$
		$S_{6b} = 1/\sqrt{2}(\Delta\alpha_2 - \Delta\alpha_3)$

a) The numbers in the parentheses are observed frequencies from Ref.44.

b) R is the distance between C and I atoms,
r_i is the distance between C and H^i atoms,
α_i is the angle of H^iCI, and
γ_i is the angle of H^jCH^k:
(i,j,k)=(1,2,3),(2,3,1),(3,1,2).

$$Q_k(t) = Q_k^0 \cos(\lambda_k^{\frac{1}{2}} t + \delta_k) \qquad (k = 1,2,\cdots,9) \qquad (20)$$

$$Q_k^0 = (2\varepsilon_k/\lambda_k)^{\frac{1}{2}} \qquad (21)$$

$$\varepsilon_k = \lambda_k^{\frac{1}{2}}(v_k + 1/2) \qquad (22)$$

$$\delta_k = 2\pi\xi_k \qquad (23)$$

λ_k's were obtained by diagonalizing the force constant matrix of the ground state of CH_3I (Table IV), which was determined by the contracted SOCI calculations described in Section 2-1. The calculated frequencies well reproduced the observed ones (45). ε_k is the energy of mode k with a vibrational quantum number v_k in eq. 22 (in the present trajectory calculation, all v_k's were set to 0 except for the cases explicitly specified in section 4-4). The phase factor of vibration δ_k was calculated according to eq. 23, where ξ_k is a random number uniformly distributed between 0 and 1.

Normal coordinates and conjugate momenta were transformed into cartesian coordinates and conjugate momenta, which were used as the initial conditions of 500 trajectories on the excited states.

2-3-2. Condition of Integration

In our main calculation, we started each trajectory on the $^3Q_0$ adiabatic surface. A discussion on the trajectories starting on the $^1Q_1$ surface will be given in a discussion. This is based on the experimental finding that the A-band is dominated by the transition from the ground to the $^3Q_0$ state. Integration of the Hamilton equation of motion on the adiabatic surfaces was carried out by the Runge-Kutta method. In the present calculation, three C-H bond distances were fixed at r_e. This was done by giving very large force constants with respect to three C-H stretches. The time step used for integration was 0.1 fsec. When the absolute value of the difference between a triplet (V_3) and a singlet (V_1 or V_2) diabatic term was less than 10^{-3} a.u., the time step

was reduced to 0.01fsec in order to determine the timing of non-adiabatic transition accurately.

2-3-3. Treatment of Non-adiabatic Transition

As a trajectory evolves in time, the $^3Q_0$ diabatic surface, correlating to the $CH_3 + I^*$ dissociation limit, must cross the $^1Q_1$ surface, correlating to the $CH_3 + I$ limit. In our trajectory calculation, the non-adiabatic transition between the two surfaces was treated as follows. When the energy difference between one of the diabatic singlets and the triplet, V_1-V_3 or V_2-V_3, changed the sign from positive to negative, which occurred only once for V_1-V_3 and V_2-V_3, respectively, in each trajectory, the transition probability P was calculated based on the Landau-Zener model (46) according to eq. 24 :

$$P = 1 - \exp(-2\pi V_{ij}^2/v_\perp \Delta F_{ij}), \quad (i,j) = (1,2) \text{ or } (1,3) \quad (24)$$

$$\Delta F_{ij} = |F_i - F_j|$$

F_i and $v_\perp$ are the diabatic force and the velocity of this trajectory to the direction perpendicular to the crossing seam. Whether the transition is allowed or not was determined by the Monte Carlo method (47); if the diabatic transition probability P is greater than a random number ξ uniformly distributed between 0 and 1, the transition is allowed and the trajectory is hopped onto the diabatic singlet surface, correlating to $CH_3 + I$; otherwise the trajectory remains on its present diabatic surface,

which correlates $CH_3 + I^*$ in the dissociation limit. In the latter case, the trajectory crosses the other singlet surface within several time steps after the first crossing. At this point, the transition probability was calculated again and it was determined whether the surface hopping takes place here or not. In any case the actual trajectory calculation was carried out on the adiabatic PES's and the correction to the momentum perpendicular to the seam was made in order to conserve the total energy of the trajectory.

2-3-4. Analysis of Trajectories

When the distance between the CH_3 center of mass and the I atom was greater than 20.0 a.u., the trajectory was stopped and the vibrational quantum number v_2 of the CH_3 ν_2 mode and the rotational quantum number were calculated.

The potential energy ε_{pot} contributing to the CH_3 ν_2 umbrella mode depends only on the inversion angle α, and the kinetic energy ε_{kin} of the ν_2 mode is calculated by the CH_3 internal velocity components perpendicular to $r_{CH}i$ (i=1,2,3). The vibrational quantum number v_2 was calculated from the sum of potential and kinetic energy according to eq. 25, where $\tilde{\nu}_2$ is the fundamental frequency of the umbrella mode, and was rounded off to an integer.

$$\varepsilon_{tot} = \varepsilon_{pot} + \varepsilon_{kin} = \tilde{\nu}_2(v_2+1/2) \qquad (25)$$

The CH_3 rotational quantum number N was calculated by taking the rotational angular momentum L_{CH3}^{rot} around the CH_3 center of mass and was rounded off to an integer.

$$L_{CH3}^{rot} = \sum_{i=1}^{4} m_i(r_i - r_{CM}) \times (\dot{r}_i - \dot{r}_{CM}) \qquad (26)$$

$$N = |L_{CH3}^{rot}|$$

The projections, $N^{//}$ and $N^{\perp}$, to the direction parallel and perpendicular to the CH_3 top axis, respectively, are calculated as follows:

$$|L_{CH3}^{//}| = N^{//}, \qquad |L_{CH3}^{\perp}| = N^{\perp}, \qquad (27)$$

$$N^2 = N^{//2} + N^{\perp 2}$$

2-4. PES and Photodissociation Dynamics

2-4-1. Features of the Potential Energy Surfaces

At first we describe the global features of the present analytically fitted PES's. We also compare these with the empirical SB and GS surfaces (17,36).

Fig.4 shows the present analytical $^3Q_0$ and $^1Q_1$ potential energy surfaces for the C_{3v} symmetry. In the C_{3v} symmetry, all the off-diagonal elements V_{ij} are zero, and V_i represent the adiabatic potential surfaces. Fig.4(a) represents the potential energy curves with respect to R with α optimized for each R (cf. Fig.2). The $^1Q_1$ curves (degenerate due to the C_{3v} symmetry) monotonically decrease in energy as R increases. On the other hand, $^3Q_0$ has a shallow well (0.223 eV at R= 3.493 Å and α=91.4°) outside the conical intersection. This is similar to the other ab initio result (0.157 eV at R= 3.5 Å and α=92.6°) by Tadjeddine et al.(22). Brus and Bondybey have pointed out from the analysis of the emission spectrum in the photolysis of CH_3I and CD_3I in Ne at 4.2 °K that the $^3Q_0$ surface is slightly bound (<0.248 eV at around R=3.3 Å) (6).

Next we describe the contour maps in the C_{3v} symmetry. As far as the symmetry of the CH_3I system is restricted to C_{3v}, this is exactly equivalent to a linear XCI system where X is a pseudo-atom placed at the center of mass of three hydrogen atoms with their combined mass. We define a new coordinate system, (R_{tr},r_{int}), replacing the original coordinate system (R, α). R_{tr} is the distance between the I atom and the CH_3 center of mass and r_{int} is the XC distance.

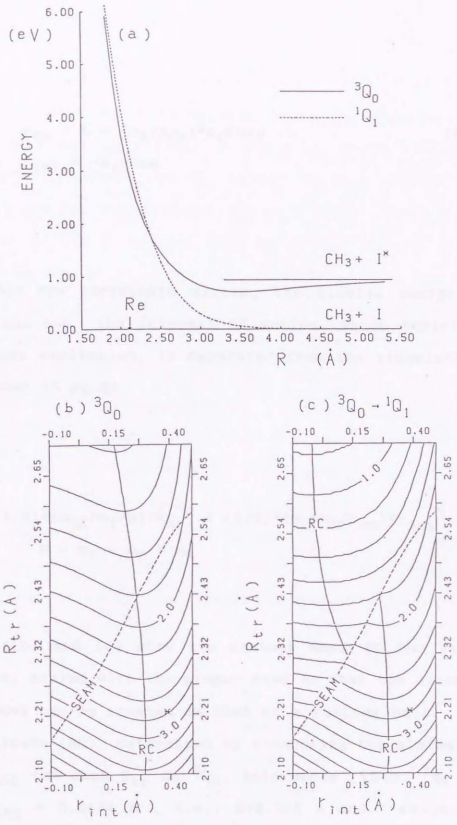

Fig.4 Present potential energy surfaces in the C_{3v} symmetry. (a) The potential energy curves with respect to R, with α optimized for each R. (b) $^3Q_0$ and (c) $^3Q_0$ -> $^1Q_1$ contour maps. Contour spacing is 0.2 eV, relative to the CH_3 + I ($^2P_{3/2}$) limit. SEAM represents the conical intersection, at which $^3Q_0$ and $^1Q_1$ surfaces are connected in (c). RC and * represent the reaction coordinate and the ground state equilibrium geometry, respectively.

$$R_{tr} = R - (m_X/m_{CX})*r_e\cos\alpha \qquad (28)$$
$$r_{int} = -r_e\cos\alpha$$

In this new coordinate system, the kinetic energy operator is diagonal and the internal CX motion, which contributes to the ν_2 mode excitation, is separated from the translational motion, as shown in eq.29.

$$T = (1/2)*(m_{CX}*m_I/M)*\dot{R}_{tr}^2 + (1/2)*(m_C*m_X/m_{CX})*\dot{r}_{int}^2 \qquad (29)$$
$$M = m_I + m_C + m_X$$

Figs.4(b) and (c) show the contour maps in the new coordinate system, scaled with the proper mass so that the dynamics on these surfaces can be treated as that of a rolling ball. The reaction coordinate (RC), determined by connecting the minima with respect to r_{int} for each R_{tr} on $^3Q_0$, intersects with $^1Q_1$ at R_{tr}=2.422 Å, r_{int} = 0.2674 Å , i.e., R=2.365 Å and α=104.3°. When a point is located on the right (left) hand side of the RC, it receives a force which tends to reduce (increase) r_{int}, i.e. α. The change of r_{int} and α on the RC is slow with respect to the change of R_{tr}. Since the Franck-Condon region (α = 111.2°) is

located slightly away from the RC (α = 106.0° at the same R_{tr}), a small force for internal excitation is expected in the early stage of reaction on $^3Q_0$. In fig.4(c), which shows the potential surface $^3Q_0$ before and $^1Q_1$ after the seam of conical intersection, one can see that the RC on $^1Q_1$ has a small r_{int}, i.e. $\alpha \sim 90°$ and is quite far away from RC on $^3Q_0$. When a trajectory hops from the $^3Q_0$ to $^1Q_1$, the force and the force constant with respect to r_{int} change very much. As will be discussed later, these characteristic differences between $^3Q_0$ and $^1Q_1$ are the essential factor governing the difference in ν_2 vibrational excitation in the CH_3 product.

Here we would like to make a brief comparison between the present ab initio surfaces in the C_{3v} symmetry and the SB and GS empirical surfaces (which are defined only within the C_{3v} symmetry), shown in Fig.5. Both SB and GS $^3Q_0$ surfaces monotonically decrease without a well, in contrast to the present surface which has a shallow well. The reaction coordinate on both SB $^3Q_0$ and $^1Q_1$ surfaces pass through near r_{int}=0 for any R_{tr}, indicating that as soon as the system is excited to $^3Q_0$, CH_3 wants to be planar. The preference of the planar CH_3 does not change by switching from $^3Q_0$ to $^1Q_1$. These imply that the umbrella mode excitation is mainly determined at the Franck-Condon region and that there should be little, if any, channel selectivity (17). These features are again in a clear contrast with those of the present surfaces. On the other hand, roughly speaking, the GS surfaces were designed to reproduce the recent experimental findings about the CH_3 ν_2 mode excitation, and are similar to the

present surfaces except for the behavior of the conical intersection to be discussed later (36).

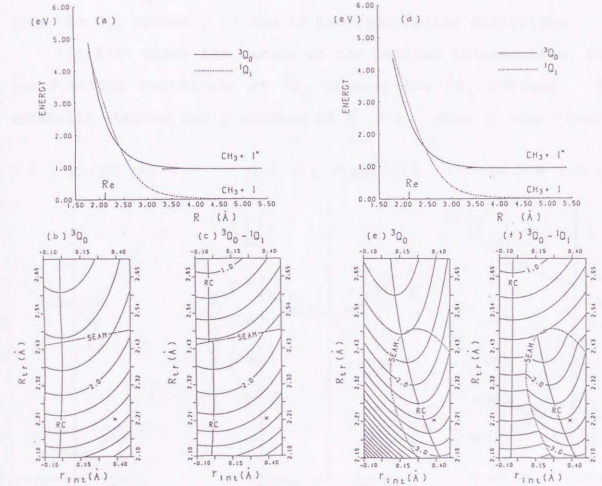

Fig.5 Empirical potential energy surfaces (a)-(c) by Shapiro and Bersohn, and (d)-(f) by Guo and Schatz. The scale and other glossaries are the same as in Fig.4.

Fig.6 shows examples of the present potential energy curves with respect to the bending angle θ for a few fixed values of R, where α is optimized for each state. In the Franck-Condon region (see Fig.6(a)), the $^3Q_0$ surface has a minimum at θ=0, whereas the $^1Q_1$ surface has minima at θ = ±4°. This deviation from the C_{3v} symmetry is due to the Jahn-Teller distortion.

Fig.6(b) shows the curves at the conical intersection, where the reaction coordinate of $^3Q_0$ crosses the $^1Q_1$ surface. Each adiabatic surface has a minimum at $\theta \neq 0$. When α was fixed at

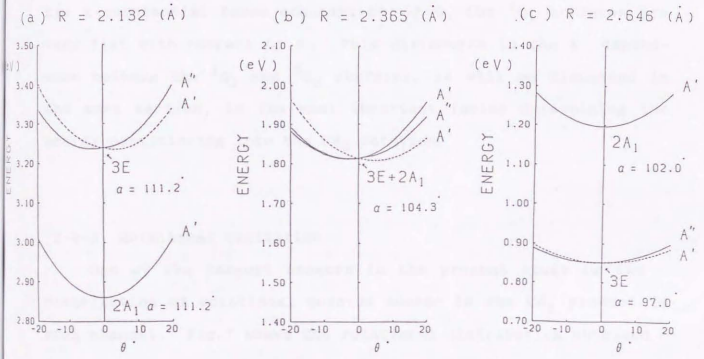

Fig.6 Adiabatic potential energy curves with respect to θ at
(a) the Franck-Condon region, R=2.132 Å
(b) the conical intersection, where the $^3Q_0$ reaction coordinate crosses $^1Q_1$, R=2.365 Å and
(c) outside the conical intersection, R=2.646 Å.
The local C_{3v} symmetry of CH_3 is assumed.
α is optimized at each R for each state for (a) and (c).
The positive and negative values of θ in these figures represent ϕ = 0 and π, respectively.

111.2°, the two surfaces intersects at R=2.445 Å for θ = 0 and the largest bending angle and the bending stabilization energy were θ_{min} = 6.0° and $\Delta E(\theta_{min}) = E(\theta_{min})-E(0°) = -4.3*10^{-3}$ eV for the A' state (48). When α is allowed to change, the RC of the $^3Q_0$ surface intersects the $^1Q_1$ surface at R = 2.365 Å and α=104.3° for θ = 0 and the largest bending stabilization is $\Delta E(\theta_{min} = 5.0°) = -5.3*10^{-3}$ eV; when α is allowed to relax, two surfaces cross at a smaller R. Fig.6(c) shows cuts of PESs outside the conical intersection region. While the $^3Q_0$ surface has a substantial force constant at θ=0, the $^1Q_1$ surfaces are very flat with respect to θ. This difference in the θ dependence between the $^1Q_1$ and $^3Q_0$ surfaces, as will be discussed in the next section, is the most important factor determining the energy partitioning into the CH_3 rotation.

2-4-2. Rotational Excitation

One of the largest concern in the present study is the distribution of rotational quantum number in the CH_3 product in each channel. Fig.7 shows the rotational distribution obtained in the trajectory calculation. We can clearly see the channel selectivity. We have found that the rotational angular momentum is nearly perpendicular to the top axis in most trajectories, i.e. $N \approx N^{\perp}$. Therefore, we use only the total rotational angular momentum N in the following discussion. Qualitatively, the CH_3 product in the I^*-channel is rotationally cool, which agrees with recent experiments (24,28,30) as well as our previous discussion

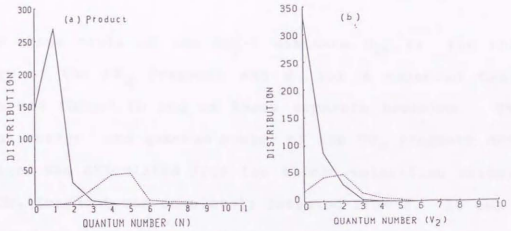

Fig.7 The final (a) rotational (N) and (b) the umbrella vibrational distribution of the CH_3 product. The reactant CH_3I is in the ground vibrational state. The solid line is the distribution in the I^*-channel, and the dotted line is the distribution in the I-channel, scaled up 3 times for clarity.

(37). Quantitatively, the present calculation predicts the peak in the rotational distribution at N=1. It is not clear at this point whether this slightly hot distribution is credible or not, considering the fact that the calculation has been carried out by quassi-classical trajectories with zero-point energies. On the other hand, one finds that the product in the I-channel is rotationally excited up to N=8 with a peak at N=5. This is in good agreement with the experiment by Chandler and co-workers (30), but is in the quantitative sense in disagreement with the PB experiment that CD_3 is rotationally excited up to N=14. If one accepts the comment that the PB experiment carried out at the room temperature may possibly involve rotationally excited parent molecules which would give hotter laboratory rotational distribution of the product due to poor alignment (27,30), the agreement with the experiments is excellent.

We have examined the origin of this selectivity in detail.

Fig.8 shows plots of the CH_3-I distance R_{tr} vs. the rotational energy of the CH_3 fragment and θ for a selected trajectory, which was forced to run on three separate branches. The rotational energy and quantum number of the CH_3 fragment during the reaction was calculated from the atomic velocities assuming that the CH_3 fragment was completely isolated from I. It can be seen in Fig.8(a) that the rotation is highly excited (N=5 in this case) *before* the non-adiabatic transition and furthermore the final rotational energy in each channel is determined by whether this excitation is more or less retained (as in the I-channel) or

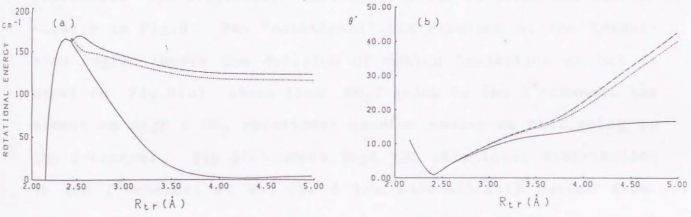

Fig.8 Plots of R_{tr} vs. the rotational energy of the CH_3 fragment, and (b) R_{tr} vs. θ for a randomly selected trajectory.
The solid line represents a trajectory which stayed on the $^3Q_0$ diabatic state and has given I*. The dotted and dashed lines are the same trajectory but have been forced to switch to the $^1Q_1(A')$ and $^1Q_1(A'')$ surface, respectively, and to give I.

is nearly completely damped (as in the I^*-channel). In Fig.8(b), the trajectory on the $^1Q_1$ surface show a smooth increase in θ while the trajectory on $^3Q_0$ does not. These differences are justifiable in relation to the shape of PES with respect to θ. The $^1Q_1$ surfaces are very flat even right after the transition region, as shown at R = 2.646 Å in Fig.6(c). Therefore, the trajectory with the kinetic energy in the "rotational" mode is expected to show a smooth increase in θ, retaining the energy. The $^3Q_0$ surface, on the other hand, now has a substantial positive bending force constant around θ = 0, and the trajectory is forced to remain within a small value of θ, releasing the rotational energy into the translational motion. Though Fig.8 represents one trajectory, this observation is borne out statistically in Fig.9. The "rotational" distribution at the transition region (where the decision of making transition or not is made) in Fig.9(a) shows that CH_3I going to the I^*-channel has almost as high a CH_3 rotational quantum number as that going to the I-channel. Fig.9(c) shows that the rotational distribution in the I^*-channel at R=3.704 Å has substantially cooled down. On the other hand, the rotational excitation in the I-channel remains unchanged (or slightly enhanced) after the transition region. Therefore, we can conclude that the rotational energy is accumulated *before* the transition, and the channel selectivity takes place *after* the transition and is due to the difference in the force constant for bending angle θ outside the conical intersection.

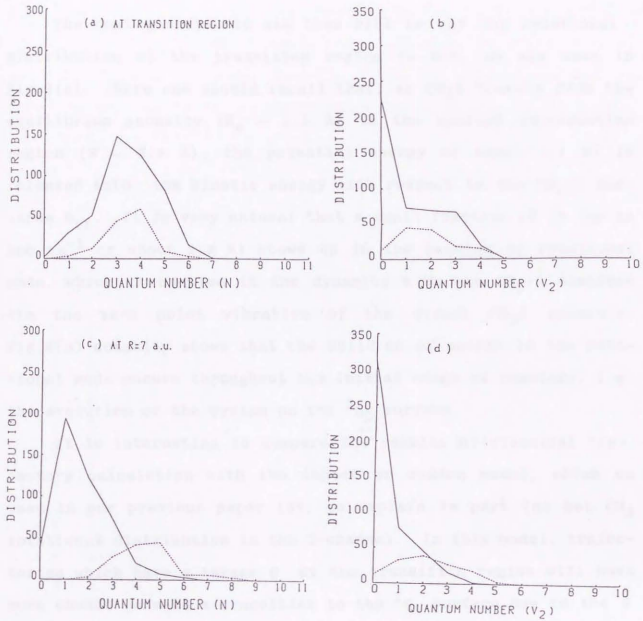

Fig.9 The rotational (N) and umbrella vibrational (v_2) distribution of the CH_3 fragment during the reaction, (a) and (b) at the transition region, and (c) and (d) at the intermediate region, R=3.704 Å. The reactant CH_3I is in the ground vibrational state. Glossaries and scales are same as in Fig.7.

The next question to ask then will be why the rotational distribution at the transition region is hot, as was seen in Fig.9(a). Here one should recall that, as CH_3I travels from the equilibrium geometry (R_e ~ 2.1 Å) to the conical intersection region (R ~ 2.4 Å), the potential energy of about 1.1 eV is released into the kinetic energy with respect to the CH_3-I distance R_{tr}. It is very natural that a small fraction of it (up to 200 cm^{-1} or about 2.2 %) shows up in the bending or rotational mode, which is coupled in the dynamics with the CH_3-I distance via the zero point vibration of the parent CH_3I molecule. Fig.8(a) actually shows that the build-up of energy in the rotational mode occurs throughout the initial stage of reaction, i.e. the evolution of the system on the $^3Q_0$ surface.

It is interesting to compare the results of classical trajectory calculation with the impact or sudden model, which we used in our previous paper (37) to explain in part the hot CH_3 rotational distribution in the I-channel. In this model, trajectories which have a larger θ at the transition region will have more chance to make a transition to the $^1Q_1$ surface due to the θ dependency of V_{13} and V_{23}. Here the torque due to the energy lowering for the bending, $|\Delta E(\theta_{min})|$, will be converted suddenly into the rotational motion. Trajectories with a small θ, on the other hand, will tend to stay on the $^3Q_0$ surface and reach the product with unexcited rotation. Fig.10 shows that there might be a weak relation between the final CH_3 rotational quantum number N and the bending angle θ_t at which the decision of making a transition or not has been made. We have also found

that the final CH_3 rotational quantum number N is unrelated to $\Delta E(\theta_{min})$ at the point of transition. Because of these results as well as the dynamical details discussed above, one has to conclude that there is no justification of a simple impact model.

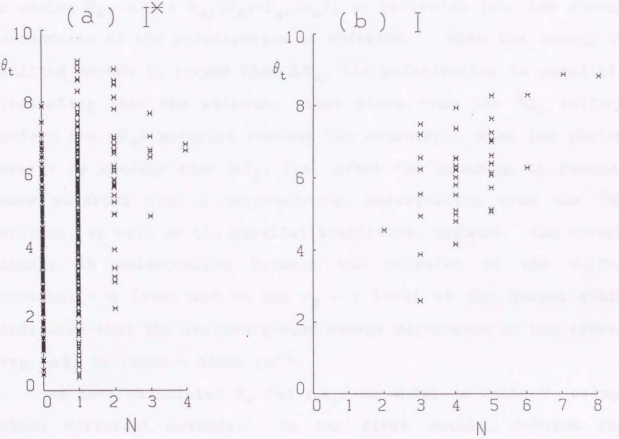

Fig.10 The bending angle θ_t, at which the decision of making a transition or not has been made, vs. the final CH_3 rotational angular momentum N for individual trajectories in (a) the I^*-channel and (b) the I-channel.

2-4-3. Relationship between Dynamics and Crossing Point

The crossing between the two electronic states, $^3Q_0$ and $^1Q_1$, has a close connection to the polarized emission spectroscopy of the dissociating CH_3I molecule by Lao et. al. (35). In their classical, one-dimensional interpretation, the difference in energy between these excited states and the ground state at the crossing R_x, $\Delta E_x = E_{ex}(R_x)-E_{gr}(R_x)$, is reflected into the energy dependence of the polarization of emission. When the energy of emitted photon is larger than ΔE_x, its polarization is parallel, indicating that the emission takes place from the $^3Q_0$ surface *before* the CH_3I molecule reaches the crossing. When the photon energy is smaller than ΔE_x, i.e. *after* the crossing is passed, some emission with a perpendicular polarization from the $^1Q_1$ surface, as well as the parallel transition, appears. The abrupt change in polarization between the emission to the v_3(C-I stretch) = 8 level and to the v_3 = 9 level of the ground state indicates that the excited-ground energy difference at the crossing, ΔE_x is 33000 - 33500 cm^{-1}.

We have calculated R_x and ΔE_x, as shown in Table V, using three different methods. In the first method, denoted the static(R) method, the $^3Q_0$ reaction coordinate (RC) is determined by connecting the potential minima with respect to r_{int} for various values of the C-I distance R within the C_{3v} symmetry, and R_x is defined to be the C-I distance R at which this RC crosses the $^1Q_1$ surface. We obtained ΔE_x to be 31035 cm^{-1} at R=2.393 Å and α=106.6°. This value is similar to the corresponding values, ΔE_x=31370 cm^{-1} and 29598 cm^{-1} of the SB and GS surfaces.

It is also similar to the values quoted in Ref.35, presumably calculated with the method similar to this. These values are lower than the experimental estimate by about 2000 cm^{-1}. Lao et al.(35) have suggested that the calculated C-I distance at the crossing R_x may be too large and that a smaller R_x should give a larger ΔE_x in better agreement with the experiment. This may well be so, because finding the exact location of crossing of two nearly parallel curves is not easy and that ΔE_x should be very sensitive to the location of crossing.

Table V. Location of Crossing and the Excited-Ground Energy Difference

Potentials	Method	R_x (Å)	α_x (°)	$E_{ex}(R_x, \alpha_x)$ (cm^{-1})	$E_{gr}(R_x, \alpha_x)$
Present	Static(R_{tr})	2.365	104.3	32196	
	Static(R)	(2.393)	(106.6)	(31035)	
	Dynamic	2.345	102.5	33051	
Tadjeddine	a)	2.353	NA	31100	
Shapiro	Static(R_{tr})	2.413	91.2	31941	
	Static(R)	(2.396)	(97.9)	(31370)	
	a)	2.403	NA	30716	
Guo and Schatz	Static(R_{tr})	2.435	98.5	30136	
	Static(R)	(2.440)	(101.1)	(29598)	

a) Taken from Table II of Ref.35. Presumably the method used is Static(R).

However, one can argue easily that the above method is not correct. Since the kinetic energy matrix for the (R, r_{int}) coordinate system is not diagonal, the results are coordinate dependent. One has to use the coordinate system which has a diagonal kinetic energy matrix, in order to obtain the coordinate independent reaction coordinate with the above minimization procedure (49). The (R_{tr}, r_{int}) coordinate system, eq.28, satisfies this condition. The crossing, determined with this method, denoted static(R_{tr}), for our surfaces occurs at a smaller R=2.365 Å and a smaller α=104.3° with a larger ΔE_x=32196 cm^{-1}. This correct static value of ΔE_x is still 1000 cm^{-1} too small in comparison with the experimental estimate. However, we can propose that the dynamic effect can account for this discrepancy. Fig.11 shows the plots of the point (R_{tr}, r_{int}) where the decision of making a transition or not has been made for trajectories. One can see immediately that most trajectories cross the conical intersection at points where both R_{tr} and r_{int}, and therefore R and α, are smaller than the above point determined statically (where SEAM and RC cross in Fig.11). Trajectories start at the FC region, which is on the right hand side of the RC. The force in the region is to reduce r_{int} and cause the trajectories on average to reach the seam of crossing at r_{int} which is smaller than r_{int} on RC. (See the next section for the trajectory that starts at the ground state equilibrium geometry). The averaged values in Fig.11, regardless of whether the transition is made (I-channel) or not (I^*-channel), are R_{tr}=2.395 Å, r_{int}=0.234 Å, i.e. R = 2.345 Å, α = 102.5°, where ΔE_x is calcu-

lated to be 33051 cm^{-1}, which is larger than the static ΔE_x by about 1000 cm^{-1}. Thus, the dynamically determined ΔE_x is much better agreement with the experimental estimate.

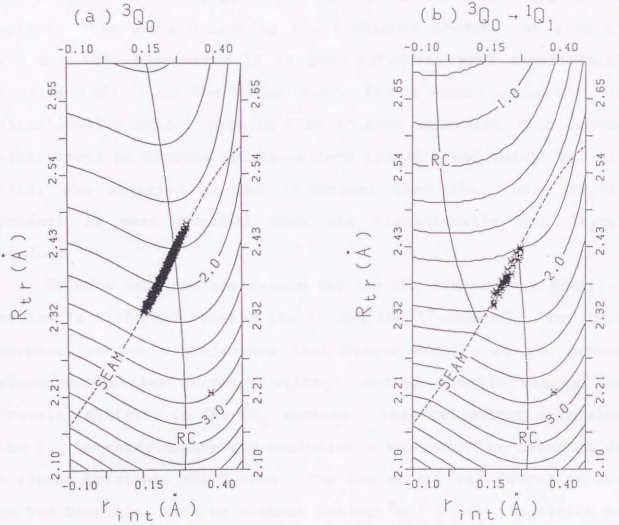

Fig.11 Plots of R_{tr} vs. r_{int} for trajectories at the point where the decision of making the transition or not has been made, (a) for the I^*-channel and (b) for the I-channel, superimposed on the contour maps of Fig.4.

2-4-4. Vibrational Excitation of Umbrella Mode

Now we turn to another important question of the final vibrational distribution in the ν_2 umbrella mode for each channel product. Fig.7(b) gives the results of the trajectory calculation. The distribution in the I-channel product has peak at v=2 and this propensity is in good agreement with experimental results (26). On the other hand, the I^*-channel product is vibrationally cold. This is also in good agreement with recent experiments by Houston and co-workers (24,30), and Suzuki et. al. (31), who observed in the I*-channel that the cold (v_2=0) product is more abundant than the vibrationally hot (v_2=2) product.

We have examined the reason why the CH_3 vibrational distribution is different between the I- and the I^*-channel. For this purpose, we use a trajectory that starts exactly at the ground state equilibrium geometry without initial kinetic energy and travels initially on the $^3Q_0$ surface. This trajectory maintains the C_{3v} symmetry during its evolution ; we treat the dynamics as a linear triatomic XCI system. The trajectory was forced to run in two branches, with or without making $^3Q_0$ -> $^1Q_1$ transition at the conical intersection. Fig.12 shows energetics and Fig.13 actual traces of two branches of the trajectory. As shown in Fig.12(a), most of the potential energy released during the dissociation is converted into the kinetic energy of the CH_3 centre-of-mass as well as that of the I atom (not shown). The difference in the kinetic energy between the two channels reflects the difference in the electronic energy between I and I^*. Fig.12(b) shows the plots of R_{tr} vs. the internal kinetic energy

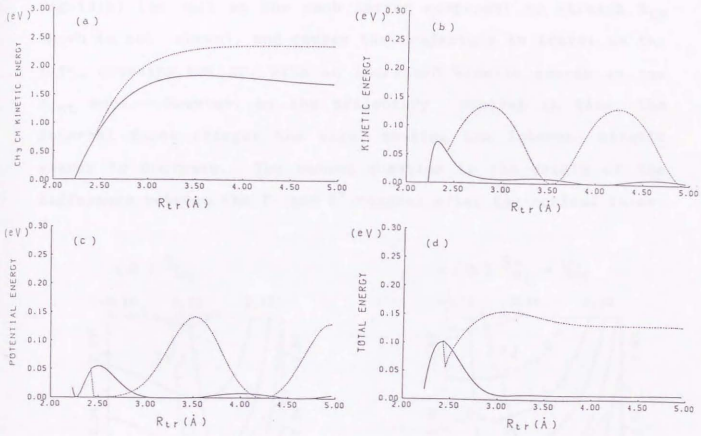

Fig.12 Plots of R_{tr} vs. (a) the kinetic energy of the CH_3 center of mass, (b) the kinetic K, (c) the potential V and (d) the total energy (K+V) in the "umbrella" mode, for the trajectory that starts at the ground state equilibrium geometry without initial kinetic energy. The solid and dotted lines represent the branches giving I^* and I, respectively.

contributing to the ν_2 mode, which is equal to the second term in eq.29. There are two questions to be answered in this figure. The first is why the internal kinetic energy decreases slightly just before the transition. As shown in Fig.13(a) and discussed in section 2-4-1, the starting point of the trajectory is on the right hand side of the RC on the $^3Q_0$ surface, and the force acting on it has a strong component to shorten r_{int}, as shown in

Fig.13(a) (as well as the much larger component to stretch R_{tr} which is not shown), and causes the trajectory to travel to the left, crossing the RC, with an increased kinetic energy in the r_{int} mode. However, as the trajectory evolves in time, the internal force changes the sign, causing the internal kinetic energy to decrease. The second question is the origin of the difference between the I- and I^*-channel after the conical inter-

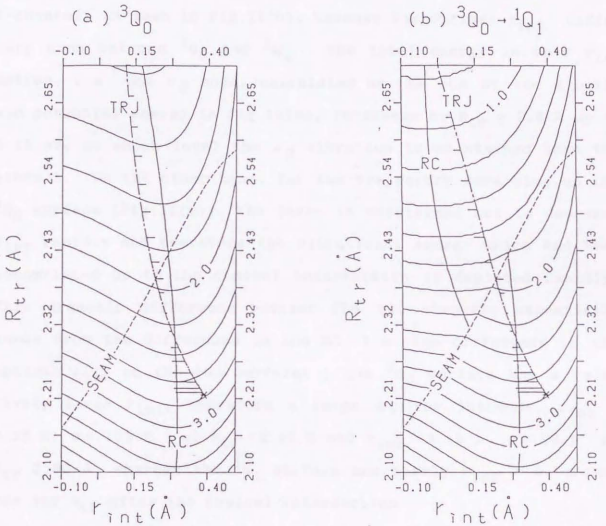

Fig.13 Plots of the zero-energy pseudo-linear trajectory (denoted TRJ), superimposed on the contour map, for (a) I^*-channel product and (b) I-channel product. The internal force , $\partial V/\partial r_{int}$ is also shown, in an arbitrary scale for several values of R_{tr} in the figure.

section. Two branches of the trajectory for I^* and I, shown in Fig.13(a) and (b), respectively, clearly demonstrate what is happening. When the trajectory in Fig.13(b) crosses the seam onto $^1Q_1$, the force with respect to r_{int} changes the sign abruptly, and the kinetic energy in the r_{int} motion increases rapidly (Fig.12(b)). The potential energy in the r_{int} motion, defined as the energy relative to the minimum with respect to r_{int}, of course changes discontinuously at the seam upon going into the I-channel, as seen in Fig.12(c), because the optimal r_{int} differ very much between $^3Q_0$ and $^1Q_1$. The total energy in this r_{int} motion, i.e. the ν_2 mode, calculated as the sum of the kinetic and potential energy in Fig.12(d), increases by R_{tr} = 2.8 Å up to 0.15 eV, at which level the ν_2 vibration is maintained into the product. On the other hand, for the trajectory remaining on the $^3Q_0$ surface (Fig.13(a)), the force is maintained not to decrease r_{int} rapidly and therefore the vibrational energy which had been accumulated up to the conical intersection is depleted rapidly. This dramatic difference between the two channels essentially comes from the difference in the RC, i.e. the difference in the optimal r_{int} on the two surfaces ; the $^3Q_0$ surface has a relatively large r_{int}, therefore a large α, for instance, r_{int} = 0.26 Å, α= 103.9 ° at R_{tr} =2.45 Å and r_{int} =0.13 Å, α= 96.9° at R_{tr} 2.80 Å, whereas the $^1Q_1$ surface has nearly r_{int} = 0, α=90° for any R_{tr} after the conical intersection.

This analysis of the zero-energy quassi-linear trajectory is actually statistically borne out in the full-dimensional trajectory calculation. As was shown in Fig.9(b) at the transition region, both I- and I^*-channel products are still cool. However,

at the intermediate region (R=3.704 Å) (Fig.9(d)), the I-channel product becomes hot and its population is close to that of the final state (Fig.7(b)). On the other hand, the I^*-channel product is cooler in the intermediate region than at the transition region. From the above discussions, we conclude that the difference in the ν_2 mode excitation between the two channels is due to the difference in the shape of PES ; $^1Q_1$ wants to have a planar CH_3, whereas $^3Q_0$ wants to maintain the bent structure until CH_3-I distance becomes very large.

We can briefly point out why the SB potential surfaces give an inverted population in the I^*-channel as well as in the I-channel. As discussed in section 2-4-1, the SB $^3Q_0$ surface, as well as the $^1Q_1$ surface, has the optimal $r_{int} \approx 0$ for any R_{tr}. The excitation of the CH_3 umbrella motion takes place immediately upon excitation to the $^3Q_0$ surface, and the $^3Q_0 \rightarrow {}^1Q_1$ hop makes very little difference in the dynamics. These defects of the SB surfaces disappear in the GS surfaces, which make it possible to have a discussion similar to the present one. As shown in Fig.5 (e) and (f), however, the behavior of the conical intersection of the GS surfaces is very different from that of the present surfaces. The GS surfaces have such a skewed conical intersection seam that some trajectories may actually cross the seam near the FC region.

2-4-5. Effect of Initial Conditions : Mode Selectivity

In order to assess how the initial vibrational states of

CH_3I in the ground electronic state affect the dynamics, we have carried out additional trajectory calculations with an initial excitation by one quantum number in each of the vibrational mode ν_2, ν_3, ν_5 and ν_6 of CH_3I. The product distributions of the ν_2 vibrational and the rotational quantum numbers thus obtained are shown in Fig.14. These figures should be directly compared with Fig.7, which is for the initial ground vibrational state of CH_3I. The excitation in the ν_3 C-I stretching mode has no effect on the product internal energy distribution. This is understandable because this C-I mode becomes the dissociation mode in the excited state. The excitation in the ν_2 CH_3 umbrella mode gives a higher excitation in the ν_2 mode in the CH_3 product for both I- and I^*-channels, but makes very little difference in the rotational distribution. Of course, the ν_2 mode of CH_3I is directly correlated to the ν_2 mode of CH_3. The excitation in the ν_6 rocking mode, which is correlated to the CH_3 rotation, gives a substantially higher rotational excitation in both I- and I^*-channels. This mode also gives a higher I/I^* branching ratio. The ν_6 mode destroys the C_{3v} symmetry of the system due to varying θ and promotes a coupling (which is zero in the C_{3v} symmetry) and therefore increases a transfer between diabatic surfaces. The ν_5 mode also destroys the C_{3v} symmetry due to changing β_i's. However, the branching ratio (as well as the distributions) is little influenced by the ν_5 mode excitation. This is understandable because the β_i's part in the coupling elements, V_{13} and V_{23}, is a quarter or less of the θ part. All these results indicate that the internal energy given to a particular mode of the reactant remains there substantially

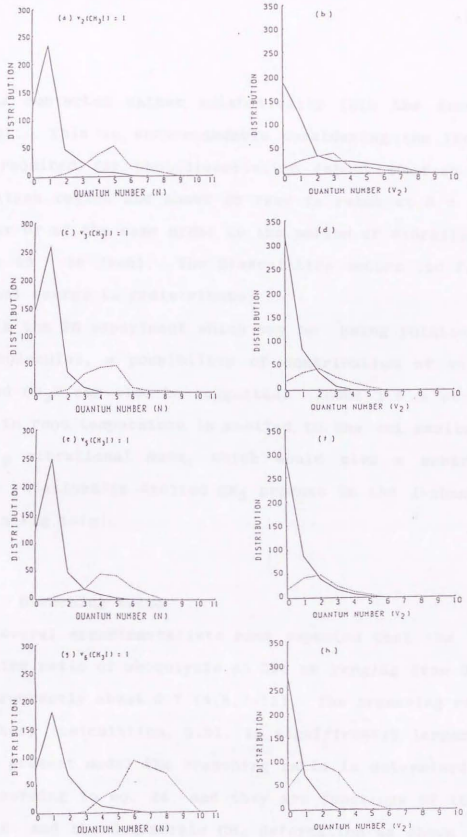

Fig.14 The final rotational,(N) and umbrella vibrational (v_2) distribution of CH_3 product.
The initial vibrational state of the parent molecule CH_3I is excited by one quantum of :
(a),(b) ν_2: sym.-CH_3-def., (c),(d) ν_3: C-I str.,
(e),(f) ν_5: d-CH_3-def., (g) and (h) ν_6: d-CH_3-rock.
Glossaries and scales are same as in Fig.7.

and is converted rather adiabatically into the energy of the product. This is understandable considering the fact that the time required for photodissociation (about 10 fsec up to the transition region and about 20 fsec to reach at R = 3.0 Å) is shorter or of the same order to the period of vibrational motions (about 20 - 60 fsec). The dissociation occurs too fast for the internal energy to redistribute.

In the PB experiment which may be using rotationally warm CH_3I molecules, a possibility of contribution of vibrationally excited CH_3I can also be suggested. About 1.5 % of CH_3I molecules in room temperature is excited to the v=1 excited state of the ν_6 vibrational mode, which would give a contribution to highly rotationally excited CH_3 product in the I-channel, as is seen in Fig.14(g).

2-4-6. Branching Ratio

Several experimentalists have reported that the $I^*/(I+I^*)$ branching ratio of photolysis at 266 nm ranging from 0.6 to 0.9, most frequently about 0.7 (4,5,7-12). The branching ratio in our trajectory calculation, 0.91, is significantly larger than 0.7. In the present model the branching ratio is determined by V_{13} or V_{23} according to eq. 24, and they are functions of the bending angle θ and the degenerate CH_3 deformation as shown in eqs.17-18. Eqs.17-18 are valid, as far as only six degrees of freedom are used in the potential functions and consequently in the dynamics. If three C-H stretching degrees of freedom, frozen in the present study, are taken explicitly into account, however,

the degenerate stretching modes, $S_{4a} = 1/\sqrt{6}(2\Delta r_1 - \Delta r_2 - \Delta r_3)$ and $S_{4b} = 1/\sqrt{2}(\Delta r_2 - \Delta r_3)$ are expected to contribute to V_{13} and V_{23} as well. Our preliminary ab initio SOCI calculations with varying C-H distances (50) indicate that actually there are new additive contributions from S_{4a} and S_{4b}, of the same order of magnitude as the terms in eqs.17-18. Thus, if we carry out a trajectory calculation using potential functions including C-H stretches, the branching ratio is expected to decrease, to approach experimental values. A recent experimental finding shows that the symmetric C-H stretch ν_1 of the CH_3 product takes place preferentially in the I-channel (30). This could be just a matter of difference in the exothermicity, but could also imply the importance of C-H stretch in the dynamics.

In the present model, trajectories are restricted to start on the $^3Q_0$, based on the experimental fact that 94 % of the absorption is $^3Q_0 \leftarrow {}^1A_1$ at about 260 nm (4). The experiment also indicates that a few percent of the A-band absorption is $^1Q_1 \leftarrow {}^1A_1$. We have also carried out a trajectory calculation starting on the $^1Q_1$ state. In this case, the branching ratio to the I^*- and I- channel is calculated to be 0.03 : 0.97. Therefore, the contribution of a few percent of $^1Q_1 \leftarrow {}^1A_1$ absorption is expected to decrease the calculated branching ration $I^*/(I+I^*)$ by a few percent.

2-5.Conclusion

We have calculated the potential energy surfaces of CH_3I photodissociation with the contracted spin-orbit CI method. The contracted SOCI gives the results almost undistinguishable to the uncontracted SOCI method, while reducing the computer time substantially.

Our analytical potential functions, derived from ab initio results in six degrees of freedom, and surface hopping trajectories on them can reproduce important recent experimental results, including (i) the hot CH_3 rotational distribution with peak at N=5 in the I-channel and the cold distribution in the I^*-channel, (ii) the hot CH_3 ν_2 vibrational distribution with peak at v_2=2 in the I-channel and the cold distribution in the I^*-channel, and (iii) the excited-ground energy difference at the seam of conical intersection where trajectories make a transition, if the dynamics effect is taken into account.

The CH_3 rotational excitation is mainly determined by the shape of potential energy surfaces with respect to the bending angle θ outside the conical intersection. The rotation is hot when trajectories arrive at the conical intersection. If a transition is made onto the $^1Q_1$ surface to give an I-channel product, the $^1Q_1$ surface which is flat with respect to θ retains the rotational excitation. If the trajectory stays on $^3Q_0$ to give an I^*-channel product, the $^3Q_0$ surface which has a large bending force constant damps the rotational excitation. The CH_3 ν_2 vibrational excitation, on the other hand, is mainly determined by the shape of potential surfaces with respect to the CH_3 umbrella angle α outside the conical intersection. The reaction

coordinate on $^1Q_1$ has $\alpha \sim 90^\circ$ outside the conical intersection, whereas that on $^3Q_0$ retains relatively large $\alpha \sim 110^\circ$, until the CH_3-I distance is very large. The ν_2 vibration is relatively cool when trajectories arrive at the conical intersection. If a transition is made from $^3Q_0$ to $^1Q_1$ to give an I-channel product, the trajectory receives an abrupt, strong force to reduce α, because of the difference in the optimal α between two surfaces, and the ν_2 vibration becomes excited. If the trajectory stays on $^3Q_0$, energy cannot easily flow into the vibrational mode.

Trajectories cross the conical intersection on average with a smaller CH_3-I distance and a smaller CH_3 umbrella angle than what the reaction coordinate indicates. This dynamical effect can account for the discrepancy in the ground-excited energy difference between the polarized emission experiment and the calculation on the reaction coordinate.

Appendix

Considering the numerical behavior of the diabatic terms and the requirement that the adiabatic $^3Q_0$ and $^1Q_1$ energies are invariant under permutation among the three hydrogen atoms, the fitting functions have to have the forms shown in (A.1) to (A.6),

$$V_1 = V_{10} + P_1X + P_2S_a \tag{A.1}$$

$$V_2 = V_{10} - (P_1X + P_2S_a) \tag{A.2}$$

$$V_3 = V_{30} \tag{A.3}$$

$$V_{12} = P_1Y + P_2S_b \tag{A.4}$$

$$V_{13} = Q_1X + Q_2S_a \tag{A.5}$$

$$V_{23} = -(Q_1Y + Q_2S_b) \tag{A.6}$$

where V_{10}, V_{30}, P_1, P_2, Q_1 and Q_2 are functions with respect to R, α, θ, which are invariant under permutation and S_a, S_b, X and Y are defined by (A.7) to (A.10).

$$S_a=1/\sqrt{6}(2\Delta\beta_1-\Delta\beta_2-\Delta\beta_3) \tag{A.7}$$

$$S_b=1/\sqrt{2}(\Delta\beta_2-\Delta\beta_3) \tag{A.8}$$

$$X(\phi,\beta_2,\beta_3,\xi)=[\cos(3\phi+\xi)+\cos\{3(\phi+\beta_3)+\xi\}+\cos\{3(\phi-\beta_2)+\xi\}]/3 \tag{A.9}$$

$$Y(\phi,\beta_2,\beta_3,\xi)=[\sin(3\phi+\xi)+\sin\{3(\phi+\beta_3)+\xi\}+\sin\{3(\phi-\beta_2)+\xi\}]/3 \tag{A.10}$$

$$\tan\xi=S_b/S_a \tag{A.11}$$

A set of dihedral angles, $A=\{\phi,\phi+\beta_3,\phi-\beta_2\}$, are defined by those of the I atom against the three hydrogen atom H^1, H^2 and H^3, respectively (cf. Fig.2). If one permutes two hydrogens,

one would obtain another set of angles, A' $=\{\phi', \phi'+\beta_3', \phi'-\beta_2'\}$. However, two sets, A and A' are identical.

Next we comment on the phase factor ξ in X (and Y). The secular equation composed of (A.1) to (A.6) gives a cubic equation in (A.12),

$$x^3 - (2V_{10}+V_{30})x^2 + [-(V_{10}^2+2V_{10}V_{30}) + (P_1^2+Q_1^2)(X^2+Y^2) + (P_1^2+Q_1^2)(S_a^2+S_b^2) + (P_1P_2+Q_1Q_2)(XS_a+YS_b)]x - (V_1V_2V_3+2V_{12}V_{23}V_{13}-V_1^2V_{23}-V_2^2V_{13}+V_3^2V_{12}) = 0 \qquad (A.12)$$

In order to satisfy the energy invariance under permutation, the coefficients of the cubic equation have to satisfy the invariance under permutation. The coefficients of the second order, and the first to third coefficients of the first order are invariant. If one choose the phase factor ξ determined by (A.11), the fourth coefficient of the first order in (A.12) equals to $X(\phi, \beta_2, \beta_3, 0)$, which is invariant due to the fact that the dihedral angle set A is invariant. It can be also proved that the constant term is invariant under permutation.

References.

1. J.V.V.Kasper and G.C.Pimentel, Appl.Phys.Lett. 5 231 (1964).

2. M.J.Dzvonik and S.C.Yang, Rev.Sci.Instrum. 45 750 (1974).

3. M.J.Dzvonik, S.C.Yang and R.Bersohn, J.Chem.Phys. 61 4408 (1974).

4. A.Gedanken and M.d.Rowe, Chem.Phys.Lett. 34 39 (1975).

5. S.J.Riely and K.R.Wilson, Faraday Disc.Chem.Soc. 53 132 (1972).

6. L.E.Brus and V.E.Bondybey, J.Chem.Phys. 65 71 (1976).

7. M.D.Barry and P.A.Gorry, Mol.Phys. 52 461 (1984).

8. R.K.Sparks, K.Shobatake, L.R,Carlson and Y.T.Lee, J.Chem.Phys. 75 3838 (1981).

9. S.L.Baughcum and S.R.Leone, J.Chem.Phys. 72 6531 (1980).

10. G.N.A.van Veen, T.Baller, A.E.de Vries and N.J.A. van Veen Chem.Phys. 87 405 (1984).

11. H.W.Hermann and S.R.Leone, J.Chem.Phys. 76 4766 (1982).

12. W.P.Hess, S.J.Kohler,H.K.Haugen and S.R.Leone, J.Chem.Phys. 84 2143 (1986).

13. J.K.Knee, L.R.Khundkar and A.H.Zewail, J.Chem.Phys. 83 1996 (1985).

14. T.F.Hunter and K.S.Kristjansson, Chem.Phys.Lett. 58 291 (1978).

15. M.Shapiro and R.Bersohn, Ann. Rev.Phys.Chem. 33 409 (1982).

16. M.Shapiro and R.Bersohn, J.Chem.Phys. 72 3810 (1980).

17. M.Shapiro, J.Phys.Chem. 90 3644 (1986).

18. S.Y.Lee and E.J.Heller, J.Chem.Phys. 76 3035 (1982).

19. S.Kanfer and M.Shapiro, J.Phys.Chem. 88 3964 (1984).

20. R.L.Sundberg, D.Imre, M.O.Hale, J.L.Kinsey and R.D.Coalson, J.Phys.Chem. 90 5001 (1986).

21. S.K.Gray and M.S.Child, Mol.Phys. 51 189 (1984).

22. M.Tadjeddine, J.P.Flament and C.Teichteil, Chem.Phys. 118 45 (1987).

23. R.O.Loo, G.E.Hall,H.P.Haerri and P.L.Houston,
J.Phys.Chem. 92 5 (1988).

24. R.O.Loo, H.P.Haerri, G.E. Hall and P.L.Houston,
J.Chem. Phys. 90 4222 (1989).

25. J.F.Black and I.Powis, Chem.Phys.Lett. 148 479 (1988).

26. J.F.Black and I.Powis, Chem.Phys. 125 375 (1988).

27. J.F.Black and I.Powis, J.Chem.Phys. 89 3986 (1988).

28. I.Powis and J.F.Black, J.Phys.Chem. 93 2461 (1989).

29. D.W.Chandler and P.L.Houston, J.Chem.Phys. 87 1445 (1987).

30. D.W.Chandler, J.W.Thoman Jr., M.H.M Jassen and D.H.Parker,
Chem.Phys.Lett. 156 151 (1989).

31. a) H.Kanamori and E.Hirota, private communication.
b) T.Suzuki, H.Kanamori and E.Hirota, private communication.

32. G.E.Hall, T.J.Sears and J.M.Frye,
J.Chem.Phys. 90 6234 (1989).

33. D.Imre, J.L.Kinsey, A.Asinha and J.Krenos,
J.Phys.Chem. 88 3956 (1984).

34. M.O.Hale, G.E.Galcica, S.G.Glogover and J.L.Kinsey,
J.Phys.Chem. 90 4997 (1986).

35. K.Q.Lao, M.D.Person, P.Xayariboun and L.J.Butler,
J.Chem.Phys. 92 823 (1990).

36. H.Guo and G.C.Schatz, J.Chem.Phys. 93 393 (1990).

37. S. Yabushita and K.Morokuma, Chem.Phys.Lett. 153 517 (1988).

38. (a) S.Huzinaga, J.Chem.Phys. 42 1293 (1965).
(b) T.H.Dunning Jr., J.Chem.Phys. 53 2823 (1970).

39. W.R.Wadt and P.J.Hay, J.Chem.Phys. 82 284 (1985).

40. (a) R.Shepard, I.Shavitt, R.M.Pitzer, D.C.Comeau,
M.Pepper, H.Lischka, P.G.Szalay, R.Ahlrichs, F.B.Brown
and J-G. Zhao, Int.J.Quant.Chem. S22 149 (1988).
(b) IMS Computer Center Library, implemented by S.Yabushita.

41. J.S.Cohen, W.R.Wadt and P.J.Hay,
J.Chem.Phys., 71 2995 (1979).

42. K.H.Hellwege, ed., Landolt-Bornstein new series Vol 7,
Structure data of free polyatomic molecules,
(Springer Berlin, 1976) p42.

43. V.Spiko and P.R.Bunker, J.Mol.Spectrosc. 95 381 (1982).

44. M.Baer, ed. 'Theory of Chemical Reaction Dynamics',p.1, CRC Press 1985.

45. T.Shimanouchi, ed., 'Tables of Molecular Vibrational Frequencies', Consolidated Vol. 1, NSRDS-NBS 39.

46. E.E.Nikitin, ed., 'Theory of Elementary Atomic and Molecular Processes in Gases', Claredon Press, Oxford (1974) Chap 3.

47. R.K.Preston and J.C.Tully, J.Chem.Phys. 54 4297 (1971).

48. This is slightly different from our previous result that α =111.2° (fixed), R=2.445 Å , θ_{min} = 6.4° and $\Delta E(\theta_{min})$ = $-5.3*10^{-3}$eV.

49. (a) K.Fukui, S.Kato and H.Fujimoto, J.Am.Chem.Soc. 97 1 (1975).
(b) S.Kato and K.Morokuma, J.Chem.Phys. 73 3900 (1980).

50. Y.Amatatsu, S.Yabushita and K.Morokuma, to be published.

Part III

General Conclusion

In this research, the author has intended to clarify the behavior of electronically excited molecules based on ab initio potentials.

In Part I, the author examined the mechanism of CT state formation of DMABN in an aqueous solution, of which a realistic molecular model has been actually nonexistent. The solvation properties based on ab initio MO calculations and Monte Carlo simulations are in qualitative agreement with the available experimental data. The potential energy of S_2 state, which relates CT state, increases monotonically and the 90° twisted geometry is at the top of potential energy surface with respect to the torsional angle in the gas phase. On the other hand, in an aqueous solution, the potential of mean force of S_2 state become very flat in a wide range of the torsional angle, which is the origin of broad emission band in a polar solvent. The dynamics of CT state formation has two factors. It was pointed out from the reaction free energy surfaces that initially the intramolecular (that is, torsional) fluctuations play an important role in the dynamics. However, once the transition from S_1 to S_2 free energy surface is occurred, the solvent diffusion plays an important role alternatively.

In Part II, the author examined the A-band photodissociation dynamics of methyl iodide, which could not be treated as a linear triatomic system. The contracted SOCI calculations are useful method to obtain the multi-dimensional potential surfaces instead of terribly large scale variational SOCI calculations because the energies relative to the ground state well reproduce variational ones and the CPU time can be saved substantially. The present

potential functions, derived from ab initio result in six degrees of freedom, and surface hopping trajectories on them can reproduce important recent experimental results, including (i) the hot CH_3 rotational distribution with peak at N=5 in the I-channel and the cold distribution in the I^*-channel, (ii) the hot CH_3 ν_2 vibrational distribution with peak at v_2=2 in the I-channel and the cold distribution in the I^*-channel, and (iii) the excited-ground energy difference at the seam of conical intersection where trajectories make a transition, if the dynamics effect is taken into account. It was found that these findings are in close relation to the shape of $^3Q_0$ and $^1Q_1$ potential energy surfaces.

In this research, the author started with making a potential energy surface by means of ab initio MO calculation and went on to making theoretical investigations based on Monte Carlo simulations or classical trajectory calculations in order to clarify two attractive problems of the behavior of electronically excited polyatomic molecules. To obtain the ab initio potential functions is the first step and very important to make theoretical investigations of the structure and dynamics of electronically excited molecules.

List of Publications

1. 'Pyrolysis of Amines: Infrared Spectrum of 1-Aminopropene'
   Y.Hamada, Y.Amatatsu and M.Tsuboi,
   J.Mol.Spectrosc. 110 369-378 (1985).

2. 'Pyrolysis of Amines: Infrared Spectrum of N-methylvinylamine'
   Y.Amatatsu, Y.Hamada, M.Tsuboi and M.Sugie,
   J.Mol.Spectrosc. 111 29-41 (1985).

3. 'FT-IR Detection of Unstable Molecules:
   Infrared Spectrum of 1-Azetine'
   Y.Amatatsu, Y.Hamada and M.Tsuboi,
   J.Mol.Spectrosc. 123 267-275 (1987).

4. 'FT-IR Detection of Unstable Molecules:
   Infrared Spectrum of 2-Azabutadiene'
   Y.Amatatsu, Y.Hamada and M.Tsuboi,
   J.Mol.Spectrosc. 123 276-285 (1987).

5. 'Pyrolysis of Amines: Infrared Spectrum of N-methylketenimine'
   Y.Amatatsu, Y.Hamada and M.Tsuboi,
   J.Mol.Spectrosc. 123 476-485 (1987).

6. 'Infrared Spectrum of N-Chloromethylenimine'
   Y.Amatatsu, Y.Hamada and M.Tsuboi,
   J.Mol.Spectrosc. 129 364-370 (1988).

7. 'A theoretical study on the mecanism of charge transfer state
   formation of 4-(N,N-dimethylamino)benzonitrile in an aqueous
   solution'
   S.Kato and Y.Amatatsu,
   J.Chem.Phys. 92 7241-7257 (1990).

8. 'Ab Initio Potential Energy Surfaces and Trajectory Studies of
   A-band photodissociation Dynamics :
   CH_3I^* -> CH_3 + I and CH_3 + I^*'
   Y.Amatatsu, K.Morokuma and S.Yabushita,
   J.Chem.Phys. 94 4858-4876 (1991).

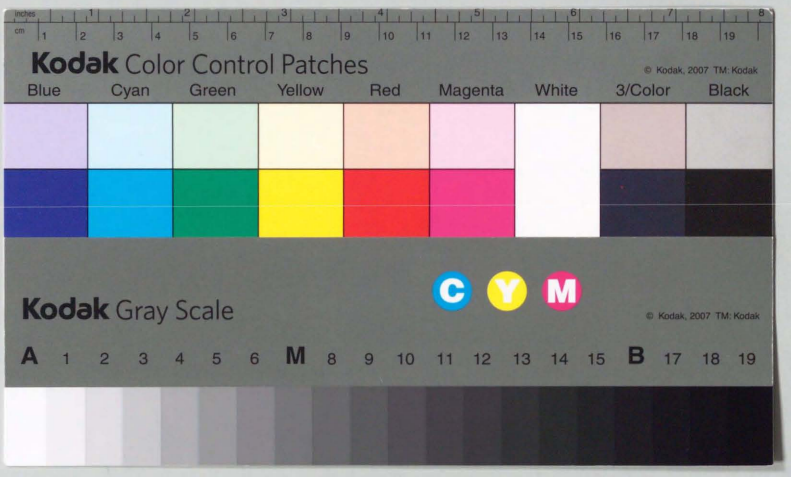
inches
cm
Kodak Color Control Patches
© Kodak, 2007 TM: Kodak
Blue
Cyan
Green
Yellow
Red
Magenta
White
3/Color
Black
Kodak Gray Scale
C
Y
M
© Kodak, 2007 TM: Kodak
A 1 2 3 4 5 6 M 8 9 10 11 12 13 14 15 B 17 18 19